Science
AAAS

Supplementary Materials for

The Winchcombe Meteorite, a Unique and Pristine Witness from the Outer Solar System

Ashley J. King, Luke Daly, James Rowe, Katherine H. Joy, Richard C. Greenwood, Hadrien A. R. Devillepoix, Martin D. Suttle, Queenie H. S. Chan, Sara S. Russell, Helena C. Bates, James F. J. Bryson, Patricia L. Clay, Denis Vida, Martin R. Lee, Áine O'Brien, Lydia Hallis, Natasha R. Stephen, Romain Tartèse, Eleanor K. Sansom, Martin C. Towner, Martin Cupak, Patrick M. Shober, Phil A. Bland, Ross Findlay, Ian A. Franchi, Alexander B. Verchovsky, Feargus A. J. Abernethy, Monica M. Grady, Cameron J. Floyd, Matthias Van Ginneken, John Bridges, Leon Hicks, Rhian H. Jones, Jennifer T. Mitchell, Matthew J. Genge, Laura Jenkins, Pierre-Etienne Martin, Mark A. Sephton, Johnathan S. Watson, Tobias Salge, Katherine A. Shirley, Rowan J. Curtis, Tristram J. Warren, Neil E. Bowles, Finlay M. Stuart, Luigia Di Nicola, Domokos Györe, Adrian J. Boyce, Kathryn M. M. Shaw, Tim Elliott, Robert C. J. Steele, Pavel Povinec, Matthias Laubenstein, David Sanderson, Alan Cresswell, Anthony J. T. Jull, Ivan Sýkora, Sanjana Sridhar, Richard J. Harrison, Francesca M. Willcocks, Catherine S. Harrison, Daniel Hallatt, Penny J. Wozniakiewicz, Mark J. Burchell, Luke S. Alesbrook, Aishling Dignam, Natasha V. Almeida, Caroline L. Smith, Brett Clark, Emma R. Humphreys-Williams, Paul F. Schofield, Luke T. Cornwell, Vassilia Spathis, Geraint H. Morgan, Mark J. Perkins, Richard Kacerek, Peter Campbell-Burns, Francois Colas, Brigitte Zanda, Pierre Vernazza, Sylvain Bouley, Simon Jeanne, Mike Hankey, Gareth S. Collins, John S. Young, Clive Shaw, Jana Horak, Dave Jones, Nick James, Steve Bosley, Alan Shuttleworth, Paul Dickinson, Ian McMullan, Derek Robson, Andrew R. D. Smedley, Ben Stanley, Richard Bassom, Mark McIntyre, Alan A. Suttle, Richard Fleet, Luc Bastiaens, Mira Ihasz, Sarah McMullan, Sarah J. Boazman, Zach I. Dickeson, Peter M. Grindrod, Annemarie E. Pickersgill, Colin J. Weir, Fiona M. Suttle, Sarah Farrelly, Ieun Spencer, Sheeraz Naqvi, Ben Mayne, Dan Skilton, Dan Kirk, Ann Mounsey, Sally E. Mounsey, Sarah Mounsey, Pamela Godfrey, Lachlan Bond, Victoria Bond, Cathryn Wilcock, Hannah Wilcock, Rob Wilcock

Correspondence to: Ashley King (a.king@nhm.ac.uk) / Luke Daly (luke.daly@glasgow.ac.uk)

This PDF file includes:

Materials and Methods
Figs. S1 to S25
Tables S1 to S23

Materials and Methods

1. Fireball Observations

1.1 *UK Fireball Alliance (UKFAll)*

The UK Fireball Alliance (UKFAll) is a collaboration of the six fireball and meteor camera networks in the UK including (1) the UK Meteor Network (UKMON), which uses a mix of CMOS digital cameras and CCD-based digital video cameras; (2) the UK Fireball Network (UKFN), based on the DSLR system developed by the Desert Fireball Network (DFN) in Australia (*32*); (3) the System for the Capture of Asteroid and Meteorite Paths (SCAMP), a deployment of all-sky cameras from the French Fireball Recovery and InterPlanetary Observation Network (FRIPON) (*33*); (4) the Network for Meteor Triangulation and Orbit Determination (NEMETODE), which uses CCD-based digital video cameras; (5) the Canadian-based Global Meteor Network (GMN), which uses CMOS digital video cameras (*34*); (6) the German-based AllSky7 network, with each site consisting of seven CMOS digital video cameras (*35*).

The Winchcombe fireball occurred at 21:54:16 (UTC) on the 28th February 2021 and lasted a little over eight seconds. The skies over the UK were clear at the time and eyewitness accounts and footage of the fireball captured on doorbell and dashboard cameras quickly appeared on social media channels or were uploaded to the International Meteor Organization (IMO) and UKMON websites. Several observers reported hearing a sonic boom. Fig. S1 shows example images of the Winchcombe fireball, which was detected by 16 of the stations operated by the UKFAll networks (Table S1). This makes the Winchcombe meteorite the most widely instrumentally observed carbonaceous chondrite fall to date.

1.2 *Trajectory*

The seven best optical records were used to measure the astrometric picks, with the remaining data having minor quality issues (e.g., unfavorable geometry, CCD blooming due to saturation, compression artefacts). Astrometric measurements were done in the SkyFit2 software

using its radial distortion models (*34*), and the trajectory was computed using a Monte Carlo solver (*36*). Fig. S2 shows the fireball trajectory on a map in relation to the observing locations. Most cameras observed the fireball from within 100 km, the closest one being in Hullavington, which was able to accurately observe the details of final fragmentation due to its proximity and high optical sensitivity.

Fig. S3 shows the trajectory fit residuals. All stations had mean measurement errors below 100 m while the fireball was moving in a straight line, typically around 50 m, on par with previous instrumentally observed meteorite falls (*37–39*). However, after the final fragmentation at a height of 35 km, the remaining fragments started deviating from a straight line. This is not a measurement error; the astrometric accuracy for the Hullavington GMN camera was 0.8 arc minutes (~15 m at the range of ~60 km to the fireball) based on 40 calibration stars selected across the field of view. This was the only camera sensitive enough to observe the end close enough to measure this deviation, thus, it was not possible to constrain the final fragment trajectory in three dimensions. A similar phenomenon has been reported for other fireballs (*40, 41*), but the cause of the deviation is currently unknown. All measurements below 35 km were excluded when computing the radiant and the pre-atmospheric orbit. The calculated fireball radiant and the pre-atmospheric orbit are given in Table S2, and the physical and atmospheric trajectory information is given in Table S3.

1.3 *Dynamics and Fragmentation Modelling*

The unsaturated light curve up to magnitude -8^{M} was determined using SCAMP/FRIPON data to an accuracy of $\pm 0.1^{M}$. The brightest part of the light curve was measured on an unsaturated reflection in the optics of the Wilcot UKMON camera and adjusted to match the absolute calibration. The light curve and the dynamics were fitted using a meteoroid ablation and fragmentation model (*42*) and an improved luminous efficiency model (*43*). Fig. S4 shows the best fit, which was achieved using physical parameters appropriate for a carbonaceous body (*44*), and

similar to those derived for the Maribo CM chondrite fall; meteoroid bulk density of ρ_M = 2000 kg m^{-3} and grain density of ρ_M = 3500 kg m^{-3} (*9*), intrinsic ablation coefficient σ = 0.005 kg MJ^{-1}, and the product of the drag and shape coefficient ΓA = 0.8.

The derived pre-atmospheric mass of 13 ± 3 kg is the smallest ever to be recorded for a carbonaceous chondrite by two orders-of-magnitude due to the low entry speed (13.5 km s^{-1}) relative to the associated fireballs of the other falls. Assisted by the shallow entry angle (~40°), the meteoroid slowly decelerated without reaching large dynamic pressures and disrupting the fragile body. The peak dynamic pressure of only 0.6 MPa is the lowest ever recorded for an instrumentally observed fall (*43*).

The observed part of the light curve above the height of 65 km is too faint compared to the model, even assuming no fragmentation. A smaller non-physical intrinsic ablation coefficient of σ = 0.002 kg MJ^{-1} better explains the observed light production; however, this is a known effect usually attributed to meteoroid pre-heating, which was not modelled in this work (*41*).

Three minor fragmentations occurred at pressures of 0.02 – 0.06 MPa, followed by a near-catastrophic 98% loss of mass into fragments at ~0.1 MPa. The subsequent dynamics could only be explained by doubling the intrinsic ablation coefficient to σ = 0.01 kg MJ^{-1}. The remaining body did not show significant fragmentation until reaching 0.6 MPa at 35 km, upon which ~100 g of dust was released. This final fragmentation was evidenced by a bright peak, following which four individual fragments became visible in the Hullavington GMN video. The dynamic mass measurements indicated that they each had masses of ~100 g, consistent with the recovery of ~600 g of meteorite stones on the ground.

1.4 *Orbital Analysis*

To gain insight on the recent dynamical past of the Winchcombe meteoroid before it crossed the Earth's path, backwards integrations of the orbit were applied (*45*). 1090 orbital clones

of the meteoroid were created based on the uncertainties (Table S2) and then integrated backwards using the Rebound IAS15 adaptive time step integrator (*46*) with the Sun + 8 planets + the Moon as active bodies. The state vector of the test particles was recorded every 1000 years, both in barycentric coordinates and as osculating ecliptic orbital elements. Backwards integrations were stopped at 3 million years in the past, way past the time for which meaningful dynamical insights of the meteoroid's history can be gained. Because the meteoroid was affected by Earth, Mars, and Jupiter in the past, the dynamical system is very rapidly chaotic. In post-analysis, the time at which each meteoroid clone entered near-Earth space (perihelion distance < 1.3 AU) was recorded. This gave a median near-Earth entry of ~80,000 years in the past, with 50% of the particles entering between 35,000 and 240,000 years. The median perihelion distance of the particles was also tracked; although the meteoroid probably spent time closer to the Sun than its impact perihelion distance suggests (~0.9868 AU), it most likely remained at > 0.7 AU throughout its history.

2. Recovered Samples

The first samples of the Winchcombe meteorite fall were found on the 1st March 2021 by the Wilcock family, who woke to discover a pile of dark powder on their driveway and fragments scattered across the front lawn in the town of Winchcombe, Gloucestershire, UK. After seeing reports of the fireball in the media, Rob Wilcock picked up fragments while wearing rubber gloves and used a stainless-steel knife to collect the powder from the impact site. This material was then placed into visibly clean polypropylene pots and sealed polyethylene zip lock bags ~12 hours after the fall. Later the same day, a 17.2 g fragment was recovered using aluminum foil from a neighbor's driveway. The find was reported to UKMON on the 1st March 2021, and on the 3rd March Richard Greenwood from the Open University visited the Wilcock family and confirmed the meteorite fall. Further material was collected from the driveway and lawn over the next four days using powder-free nitrile gloves, aluminum foil, glass vials and polyethylene sample bags.

The freshest material was transferred to the Natural History Museum (NHM), London on the 4th March 2021 and then weighed and curated on the 5th March 2021. The largest fragments (~ > 2.5 g) were wrapped in high purity aluminum foil and stored in acid free trays with Revolutionary Preservation K (RP-K) oxygen scavengers within Escal enclosures. Smaller fragments and powder were sealed in glass vials stored within polyethylene sample bags.

In the week following the fall, samples of the Winchcombe meteorite were also found on properties in the village of Woodmancote, which lies ~4 km to the west of Winchcombe. The largest individual piece of the Winchcombe meteorite is a 152.0 g fusion-crusted stone, which was recovered on the 6th March 2021 by Mira Ihasz, a member of a team from the University of Glasgow, from farmland between Winchcombe and Woodmancote. The stone, handled and initially stored using nitrile gloves and geological sample bags, was embedded in the damp soil, and split into two pieces (48.9 g and 103.1 g) during extraction, revealing a dark interior with few visible white flecks.

In total, 531.5 g of the Winchcombe meteorite was recovered less than seven days after the fall. During that week, the weather in the local area was stable and mainly cloudy; the maximum daytime temperature was 9 °C and there was no rainfall, although the humidity was high and there was heavy fog and dew on the ground. Over the next four weeks a further 70.4 g of material from the strewn field was recorded, giving the Winchcombe meteorite a total known mass of 601.9 g. Table S4 summarizes the recovered meteorites and Table S5 gives details about the samples analyzed in this study.

3. Reflectance Spectroscopy

3.1 *Visible-λ Goniometer Measurements*

The broadband (0.35 – 1.25 μm) albedo of the Winchcombe meteorite was derived from Bidirectional Reflectance Distribution Function (BRDF) measurements taken using the Visible

Oxford Space Environment Goniometer (VOSEG), a laboratory set-up that can illuminate and measure the reflectance of a sample over a range of viewing angles (*47*, *48*).

The BRDF was measured for a powdered sample of the Winchcombe meteorite (BM.2022,M1-22, 2.0 g) across 0 – 70° reflectance angles, in steps of 5°; at 15°, 30°, 45° and 60° incidence angles; and at 0°, 90° and 180° azimuthal angles. The data were then fitted using the Hapke BRDF model to enable constraints to be placed on the bulk scattering properties of the meteorite sample (*49*). Importantly, the surface profile of the sample was characterized using an Alicona 3D® instrument (Fig. S5). Therefore, two of the free parameters within the model – the filling factor, φ; and the RMS slope angle, θ – could be set, as $\varphi = 0.65 \pm 0.02$ and $\theta = 16.11°$ (at 500 µm size-scale). This enabled w, b and h_S to be set as the three open parameters within the Hapke BRDF model Least-Squares Levenberg-Marquardt fitting function. The best fit Hapke parameters were determined to be $w = 0.152 \pm 0.030$, $b = 0.633 \pm 0.064$ and $h_S = 0.016 \pm 0.008$. From the BRDF dataset, the broadband albedo value was calculated to be $A = 4.09 \pm 0.18$ %, which can be converted to hemispheric albedo by multiplying by π (*49*).

3.2 *Spectrometer Measurements*

Visible to near-infrared (VNIR) and mid-infrared (MIR) reflectance spectra of Winchcombe meteorite samples BM.2022,M1-91 and BM.2022,M2-41 were collected at the Planetary Spectroscopy Facility at the University of Oxford. Spectra were measured using a Bruker VERTEX 70v Fourier Transform Infrared spectrometer using a diffuse reflectance accessory under vacuum (~2 hPa) at 4 cm^{-1} resolution, with an average of 150 scans all calibrated to a diffuse gold target. The shortest wavelength range (0.8 – 2.0 µm) was acquired using an InGaAs detector coupled with a VIS/Quartz beam splitter, while a RT-DLaTGS detector and wide range beam splitter were used for the near- and mid-IR (2 – 30 µm). Due to features in the wide range beam splitter, data at ~16 µm were excluded from the analysis.

Fig. S6 (a) shows that the Winchcombe meteorite samples have red spectral slopes (increasing reflectance with increasing wavelength) that could be related to particle size (*50*). As both samples were prepared in the same way, slight differences in the spectral slope can be attributed to the composition and/or abundance of phyllosilicates (~88 and 93 vol%, Table S13; (*51*)). Fig. S6 (b) shows a strong feature near 2.7 μm attributed to Mg-rich phyllosilicates and OH^- /H_2O, while the shoulder near 3 μm for sample 1b-38 could be related to a higher content of iron or water. These, and other subtle features in this spectral region, are likely related to parent body aqueous alteration and adsorbed terrestrial moisture.

The MIR region contains features due to the fundamental vibrations directly caused by the structure and chemistry of the bulk mineralogy. Fig. S6 (c) shows a Christiansen feature (CF) near 9 μm consistent with low silicate polymerization. A small shift in the position of the CF to longer wavelengths for BM.2022,M1-91 correlates to the slightly higher olivine abundance in this sample (Table S13).

4. Neon Isotopic Composition

The Ne isotopic composition of the Winchcombe meteorite was determined in two ~30 mg aliquots of homogenized powder (BM.2022,M2-36 and BM.2022,M4-7). Each sample was weighed into Pt foil, loaded in an ultra-high vacuum system, and baked overnight prior to analysis. Neon was released in four steps of increasing temperature using a 970 nm diode laser until a final melt step and re-extraction to demonstrate complete degassing. Neon isotopes were measured using the electron multiplier procedure of a converted ThermoFisher ARGUS VI noble gas mass spectrometer. Neon isotope data were corrected for blanks (<1%) and mass discrimination, and the reported uncertainties are 1σ. Full details of gas extraction, purification, and analysis procedures, as well as blank levels and the corrections for isobaric interferences, are described in (*52*).

Neon data are given in Table S6. As is common for carbonaceous chondrites, the bulk of the Ne originates from trapped components rather than produced from galactic cosmic rays during recent exposure in space. High $^{20}Ne/^{22}Ne$ are present in the low temperature steps of both samples, which records the release of solar wind (SW) derived Ne, indicating either the presence of regolith material or the preservation of primordial material that was irradiated prior to accretion. The low $^{20}Ne/^{22}Ne$ of the higher temperature steps indicates that both samples contain appreciable contribution of pre-solar Ne (Ne-Q; (*53*)) and Ne-HL (*54*).

The isotopic composition of the total Ne released from each stone are plotted as circles on Fig. S7. They demonstrate that pre-solar Ne dominates in BM.2022,M4-7 and solar wind dominates in BM.2022,M2-36. The concentration of cosmogenic ^{21}Ne ($^{21}Ne_{cos}$) was determined from the measured Ne content and isotope composition and the trapped endmembers defined by (*15*). The range of $^{21}Ne_{cos}$ production rates (P_{21}) used for the calculation of cosmic-ray exposure (CRE) ages ($1.24 – 3.08 \times 10^{-8}$ cc/g/Ma) were determined using the models for carbonaceous chondrites developed by (*55*) and mean bulk chemical composition of CM chondrites from (*56*). We assume a pre-atmospheric meteoroid radius of 10 cm to 65 cm. Using the range of P_{21} CRE ages are 0.09 – 0.21 Ma for BM.2022,M2-36 and 0.06 – 0.15 Ma for BM.2022,M4-7. This is within the main CRE cluster of CM chondrites (*15*).

5. Cosmogenic Nuclides

5.1 *Analytical Procedures*

Samples of the Winchcombe meteorite (BM.2022,M2-6, OE-2021-23 (1), OE-2021-23 (7)) were analyzed non-destructively by low-background gamma-ray spectrometry. An additional sample (BM.2022,M2-40) was used for destructive analysis of ^{14}C (a soft beta-emitter) via high-sensitivity accelerator mass spectrometry (AMS). All samples were of irregular shape as they

originated during a complex fragmentation process in the atmosphere during the meteorite fall, and they clearly showed effects of ablation due to their interaction with the atmosphere.

Gamma-ray spectrometry measurements were carried out at the Faculty of Mathematics, Physics and Informatics of the Comenius University (CU, Bratislava, Slovakia), and at the Laboratori Nazionali del Gran Sasso of the Italian Institute for Nuclear Physics (INFN-LNGS, Assergi, Italy). The low-background laboratory of the Comenius University used high purity germanium (HPGe) detectors of 70% (PGT, USA) and 50% (Canberra, Belgium) relative efficiency (for 1332.5 keV gamma-rays of ^{60}Co) placed in low background shields situated in the basement of the three-storey building. The larger shield, which is used for the 70% efficiency detector, has outer dimensions of 2 × 1.5 × 1.5 m^3 and is composed of the following layers (from the outside to the inside): 10 cm of lead, 10 cm of electrolytic cooper, 10 cm of polyethylene with boric acid, 0.1 cm of electrolytic cooper, 0.1 cm of cadmium and 1 cm of perspex. On the top, a layer of 12 cm of iron is added. The inner dimensions of the shield are 80 × 90 × 172 cm^3, where an extra shield made of electrolytic copper (12 × 20 × 30 cm^3) has been inserted to further decrease the background. The radon contribution to the detector background was decreased by flushing nitrogen gas through the inner copper shielding. A detailed description of the measuring procedures, energy and efficiency calibrations and applied corrections can be found in (*57*–*59*). The INFN-LNGS laboratory STELLA (Subterranean Low-Level Assay) operates fourteen HPGe detectors, located deep underground with 1400 m rock overburden (i.e., 3800 meters of water equivalent), with additional ultra-low background shields (25 cm of lead and an inner liner of 5 cm oxygen free high conductivity copper). Radon suppression was attained by flushing the closed shielding with ultra-pure nitrogen (*60*). Both laboratories use for efficiency determination of the HPGe detectors dedicated programs based on the GEANT software package developed at CERN (*61*).

The AMS laboratory of the University of Arizona at Tucson carried out the ^{14}C analyses. Cosmogenic ^{14}C was extracted in an RF induction furnace in a flow of oxygen, and passing the gases evolved over a CuO furnace to ensure conversion to CO_2. This gas was collected and measured volumetrically. The CO_2 was then converted to graphite and analyzed on a 3 MV National Electrostatics Corporation AMS machine. The full procedure for ^{14}C measurements is given in (*62*).

The database on radionuclide decay characteristics (*63*) was used for activity calculations. The uncertainties of results were mainly due to counting statistics, which were typically below 10 %. The measuring time of gamma-ray spectrometry analysis was from 30 to 48 days, depending on the mass of the analyzed samples. Regular analysis of IAEA and NIST reference materials and participation in intercomparison exercises guarantees to maintain a good quality of results.

5.2 *Results*

Several gamma-lines were identified in the gamma-ray spectra of the analyzed meteorite fragments (122.06 keV (^{57}Co), 477.60 keV (^{7}Be), 810.77 keV (^{58}Co), 834.84 keV (^{54}Mn), 846.76 keV (^{56}Co), 889.28 and 1120.54 keV (^{46}Sc), 1173.24 and 1332.50 keV (^{60}Co), 1274.5 keV (^{22}Na), and 1808.65 keV (^{26}Al). The corresponding half-lives of these cosmogenic radionuclides are ranging from 53.22 days (^{7}Be) to 0.717 Ma (^{26}Al). AMS identified another long-lived radionuclide, ^{14}C (half-life of 5730 a). Table S7 gives results of the analyses of cosmogenic radionuclides in the Winchcombe meteorite samples. Generally, a reasonable agreement has been obtained between the gamma-spectrometry laboratories, showing results within statistical uncertainties.

Cosmogenic radionuclides found in meteorites are products of interactions of cosmic-ray particles of galactic and solar origin with the meteoroid bodies. Galactic cosmic rays because of higher energies produce in meteoroids secondary and higher generations of neutrons and protons, which then in interaction with target nuclei produce cosmogenic radionuclides, which can be used

to study the origin and characteristics of meteorites (e.g., their dimensions, CRE ages, orbits in space), as well as temporal and spatial variations of cosmic rays.

The dominant cosmogenic radionuclides present in the Winchcombe meteorite are ^{7}Be, ^{54}Mn and ^{22}Na. Other measured radionuclides (^{46}Sc, ^{26}Al, ^{56}Co) were produced in much smaller quantities. The important observation is the presence of short-lived radionuclides (^{7}Be, ^{56}Co, and ^{46}Sc), which clearly demonstrates that the analyzed fragments originated from the recent Winchcombe meteorite fall.

When comparing the measured radionuclide activities in the Winchcombe meteorite with other carbonaceous chondrites, the observed activities were much smaller. For example, in the Maribo CM chondrite, the levels of ^{7}Be, ^{26}Al and ^{60}Co were several times higher, reflecting different production scenarios. A small dispersion in activities of the samples presented in Table S7 indicates that the positions of the samples in the meteorite body were close to each other.

The ^{22}Na and ^{26}Al radionuclides were produced mainly by secondary neutron and proton reactions with energies > 10 MeV on target nuclei of Si, Al and Mg. For other radionuclides, except for ^{60}Co and ^{14}C, the main target was Fe. The measured activities depend on the flux of cosmic-ray particles, nuclear reaction cross sections, the concentration of the main target element in the meteorite, and the position of the fragment in the meteorite body. As ^{22}Na and ^{26}Al were produced in similar nuclear reactions, their activity depth profiles should be similar, and their activity ratio, ^{22}Na/^{26}Al should not depend on shielding effects in the meteorite. The observed ^{22}Na/^{26}Al activity ratio in the Winchcombe meteorite was 5.50, much higher than in the case of Maribo (1.79), and higher than the value of 1.5 averaged over a solar cycle by (*64*) for chondrites. The high ^{22}Na/^{26}Al activity ratio has been caused by unsaturated production of ^{26}Al.

A specific case is ^{60}Co, which is produced predominantly by the thermal-neutron capture reaction ^{59}Co (n, γ) ^{60}Co. ^{60}Co is one of the most suitable radionuclides for the determination of

the position of samples within the meteorite body and for calculating its pre-atmospheric radius (*65*). Unfortunately, only a detection limit for ^{60}Co was estimated (< 8 dpm kg^{-1}), which would indicate that the analyzed fragments were located on the meteorite surface, and its size was too small for the development of a nucleonic cascade.

The absence of ^{60}Co in the analyzed Winchcombe meteorite indicates either a small concentration of the target isotope (^{59}Co) in the meteorite and/or its small radius. The cobalt concentration in two Winchcombe samples was measured to be 526 and 521 ppm (Table S7), which is lower by about 10% than the mean concentration in CM chondrites (*66*). After appropriate corrections for chemical composition, and following the approach of (*67*, *68*), the pre-atmospheric radius of the Winchcombe meteorite is calculated as < 20 cm.

The measured ^{14}C activity in a small sample was 13.3 ± 0.4 dpm kg^{-1} (Table S7), and after corrections for chemical composition (*68*), the radius is 5 ± 3 cm. The measured ^{14}C activity in the Winchcombe is lower at least by about a factor of two when compared with other chondrites, which could be due to the high-water content in the meteorite, which changes the distribution of thermal neutrons by elastic scattering on hydrogen. Therefore, the ^{14}C-derived radius could be lower by about a factor of two.

^{26}Al can also be used to estimate the pre-atmospheric radius of the Winchcombe meteorite, although its activity is very low due to its short exposure age. A comparison of the saturated ^{26}Al activity in the meteorite with Monte Carlo simulations of ^{26}Al production rates in (*55*), after appropriate corrections for its chemical composition, suggest that the pre-atmospheric radius of the Winchcombe meteorite was 15 ± 5 cm. Using the measured bulk Winchcombe meteorite density of 2100 kg m^{-3}, the initial mass of the meteoroid is estimated to be 30 ± 10 kg, in a reasonable agreement with the fireball observations.

The CRE ages of the Winchcombe meteorite was calculated using the method of (*69*) using only ^{26}Al data (*70*) and equation:

$$A = P\,(1 - e^{-\lambda T}),$$

where A is the cosmogenic radionuclide activity, P is its production rate in the meteorite by cosmic-ray particles, λ is the decay constant, and T is the time of the meteorite irradiation equal to its CRE age. Fig. S8 shows saturated ^{26}Al production rates, estimated for different radii of the Winchcombe meteorite (following the Monte Carlo model of (*55*)), adjusted for its chemical composition. Using the corresponding production rates of 32 and 39 dpm kg^{-1}, the CRE ages are 0.29 Ma and 0.24 Ma, with an average value of 0.27 ± 0.08 Ma. This value is in good agreement with ^{21}Ne based value presented in this work (0.3 Ma) (Section 4).

6. Bulk Element Abundances

Major and trace element abundances of the powdered Winchcombe meteorite samples BM.2022,M1-91 and BM.2022,M2-41 were determined by inductively coupled plasma optical emission spectroscopy (ICP-OES) and inductively coupled plasma mass spectrometry (ICP-MS) in the Imaging and Analysis Centre (IAC) at the NHM. For major element analysis, ~40 mg of each powdered sample was pre-treated with 0.5 mL of concentrated NHO_3 and fused with 120 mg of $LiBO_2$ in a Pt/Au crucible to produce a flux. This was then dissolved in 0.64M HNO_3 before element abundances were measured in triplicate using a Thermo iCap 6500 Duo ICP-OES instrument, which was calibrated using a range of certified reference materials (CRMs) prepared in the same way. The standards BE-N (basalt, Groupe International de Travail) and JG-1 (granodiorite, Geological Survey of Japan) were analyzed as unknowns as a measure of accuracy.

To determine trace element abundances, a further ~40 mg of each powder was digested in HF + $HClO_4$ + HNO_3 and analyzed in triplicate using an Agilent 8900 ICP-QQQ-MS instrument. The instrument was optimized to reduce interferences by tuning CeO+/Ce+ and Ba++/Ba+ to <1 %. The accuracy of analyses was monitored by measuring CRMs BCR-2 (basalt, United States Geological Survey) and SY-2 (syenite, Canadian Certified Reference Material Project). The final meteorite abundances are given in Tables S8 and S9 and are consistent with the range for CM chondrites (e.g., *66*).

7. Oxygen Isotopes

Oxygen isotopic analysis of the Winchcombe meteorite was undertaken at the Open University, UK using an infrared laser-assisted fluorination system (*71*, *72*). For the analysis, ~150 mg fragments extracted from samples BM.2022,M1-85 and BM.2022,M1-86 were powdered and homogenized.

All of the oxygen isotope analyses of the Winchcombe meteorite were run in modified "single shot" mode (*73*). This involved loading a single aliquot (~2 mg) of the homogenized powder into one of the wells of a nickel sample block. The sample was overlain by a ~1 mm thick, 3 mm diameter internal BaF_2 window to retain the sample during laser reaction. In a second well, a 2 mg aliquot of the internal obsidian standard was loaded without a BaF_2 window. The nickel sample block was then placed into the two-part laser chamber, which was made vacuum tight using a compression seal with a copper gasket and quick-release KFX clamp (*71*, *72*). A 3 mm thick BaF_2 window at the top of the chamber allows simultaneous viewing and laser heating of the samples.

Prior to analysis the sample chamber was heated overnight under vacuum to a temperature of ~95°C to remove any adsorbed moisture. Following overnight heating, the chamber was allowed to cool to room temperature and then the flexi sections that had been brought up to atmosphere

during the sample loading procedures were purged using three aliquots of BrF_5 to remove any moisture. The sample chamber itself was kept closed during this procedure to avoid pre-reactions. Following these "flexi" blanks, the sample chamber was opened and a further single 5 min BrF_5 blank was undertaken to reduce and eliminate any residual moisture adsorbed on to the sample chamber walls. The oxygen isotope composition of this blank was analyzed using the MAT 253 microvolume facility. Following this blank analysis, the sample itself was run.

Sample heating in the presence of BrF_5 was carried out using a Photon Machines Inc. 50 W infrared CO_2 laser (10.6 μm) mounted on an X-Y-Z gantry. Reaction progress was monitored by means of an integrated video system. After fluorination, the released O_2 was purified by passing it through two cryogenic nitrogen traps and over a bed of heated KBr to remove any excess fluorine. The isotopic composition of the purified oxygen gas was analyzed using a Thermo Fisher MAT 253 dual inlet mass spectrometer with a mass resolving power of ~200. A post reaction blank was run following analysis of the Winchcombe meteorite and finally, the internal obsidian standard was fluorinated, and its oxygen isotope composition determined.

Overall system precision, as defined by replicate analyses of the internal obsidian standard, is: ± 0.053 ‰ for $\delta^{17}O$; ± 0.095 ‰ for $\delta^{18}O$; ± 0.018 ‰ for $\Delta^{17}O$ (2σ) (*74*). Oxygen isotopic analyses are reported in standard δ notation, where $\delta^{18}O$ has been calculated as: $\delta^{18}O = [(^{18}O/^{16}O)_{Sample} / (^{18}O/^{16}O)_{VSMOW} - 1] \times 1000$ (‰), and similarly for $\delta^{17}O$ using the $^{17}O/^{16}O$ ratio. VSMOW is the international standard Vienna Standard Mean Ocean Water. $\Delta^{17}O$, which represents the deviation from the terrestrial fractionation line, has been calculated as: $\Delta^{17}O = \delta^{17}O - 0.52 \times \delta^{18}O$.

Table S10 summarizes the results of the oxygen isotope analysis of the Winchcombe meteorite. Sample BM.2022,M1-85 yielded a composition of $\delta^{17}O = 2.75$ ‰, $\delta^{18}O = 9.48$ ‰, and $\Delta^{17}O = 2.18$ ‰, while sample BM.2022,M1-86 gave values of $\delta^{17}O = 0.94$ ‰, $\delta^{18}O = 7.29$ ‰, and

$\Delta^{17}O$ = 2.85 ‰. These compositions are consistent with classification of the Winchcombe meteorite as a CM chondrite.

8. Titanium Isotopes

A fragment of the Winchcombe meteorite (BM.2022,M3-16) was powdered using an agate mortar and pestle and digested in a 1:4 mixture of 29 M HF to 15 M nitric acid at 140°C in a 60 mL Savillex PFA beaker for >3 days, and then dried at 110°C. The residue was redissolved in 15 mL of aqua regia in a 20 mL PFA beaker before refluxing in a Parr bomb for 7 days at 200°C to ensure complete dissolution of acid-resistant phases.

To isolate Ti, the sample underwent three stages of liquid chromatographic separation. The first consisted of an anionic resin column (BIORAD® AG-1-X8, 100 – 200 mesh Cl-form) to remove Fe using 6 M HCl. The second consisted of a cationic resin column (BIORAD® AG-50W-X12) from which Ti was eluted, plus other "high field strength" elements (e.g., Zr, Hf, Nb, Ta) and Al, using 0.5 M HF, while the majority of matrix elements remained on the column. The final column consisted of an anionic resin, as in the first stage, eluting only Ti with a mixture acetic acid, hydrogen peroxide, and nitric acid. This results in the separation of Ca, V, and Cr from Ti such that the final Ca/Ti, V/Ti, and Cr/Ti ratios were all <1/1000. The complete procedural blanks, including dissolution, produced <3 ng of Ti, which is negligible for the mass of the Winchcombe meteorite analyzed.

Titanium isotope ratios were measured by the Bristol Isotope Group at the University of Bristol on a Thermo-Scientific Neptune MC-ICP-MS (s/n 10002) with a Jet-sample and X-skimmer cone combination. Samples dissolved in 0.3 M HNO_3 enter the plasma through an Aridus desolvating nebulizer using an Ar sweep gas with additional N_2 for increased sensitivity. Sample solution uptake rates vary between 40 – 50 µL min^{-1}. The Winchcombe meteorite sample was analyzed in "medium resolution" ($M/\Delta M$ >6000, where ΔM is the peak width between 5 – 95 %

intensity). The five Ti isotopes were measured alongside the intensities of $^{90}Zr^{2+}$, $^{51}V^{+}$, $^{52}Cr^{+}$, and $^{44}Ca^{+}$, which were monitored to track possible elemental interferences on ^{46}Ti, ^{48}Ti, and ^{50}Ti. Beam collection occurred in a "dynamic" mode, consisting of two magnetic settings with integration times of 8.4 s and a magnet setting time of 3 s. The main step collected $^{90}Zr^{2+}$, $^{46}Ti^{+}$, $^{47}Ti^{+}$, $^{48}Ti^{+}$, $^{49}Ti^{+}$ (axial mass), $^{50}Ti^{+}$, $^{51}V^{+}$, and $^{52}Cr^{+}$. The second step, measured every 10 main integration cycles, collected $^{44}Ca^{+}$ and $^{47}Ti^{+}$ (axial mass). Both steps require the measurement mass to be offset from the centre of mass onto a "peak shoulder" to avoid molecular interferences e.g., $^{36}Ar^{14}N^{+}$, $^{40}Ar^{12}C^{+}$, and $^{12}C^{16}O_2^{+}$. The beam intensities of all isotopes were measured using amplifiers with 10^{11} Ω feedback resistors, excluding $^{90}Zr^{2+}$ which used an amplifier with a 10^{13} Ω resistor, and $^{48}Ti^{+}$ which used an amplifier with a 10^{10} Ω resistor.

The sample and standards were run at concentrations of 200 ng mL^{-1} (which yield ~2 × 10^{-10} A on $^{48}Ti^{+}$) and measured over 10 repeats of single blocks of 40 integrations. Instrumental blanks, usually <1 % of the Ti signal, were measured before and after each block and subtracted from intermediate samples and standards. Mass-dependent fractionation was corrected by internal normalization using the exponential law and assuming a constant $^{49}Ti/^{47}Ti$ ratio of 0.749766 (*75*). Interferences of Ca, V, and Cr were also corrected (*76–78*). Each sample analysis was bracketed by a measurement of a standard solution of the same concentration; in this case the NIST-3162a standard reference material (SRM). Relative deviations of internally normalized Ti isotope ratios of the samples from a linear fit to internally normalized Ti isotope ratios of the bracketed NIST-3162a SRM were used to calculate $\Delta'^{X/47}Ti_{49/47}$ (reported in ppm). The reported values and errors are the mean and 2SE of 10 repeat measurements in a single session. The mean and 2SE reported values for $\Delta'^{46/47}Ti_{49/47}$, $\Delta'^{48/47}Ti_{49/47}$ and $\Delta'^{50/47}Ti_{49/47}$ from the same session for a BCR-2 basalt reference material were 1 ± 5 ppm, 2 ± 4 ppm, and 2 ±10 ppm, respectively.

Table S11 gives the Ti isotopic composition of the Winchcombe meteorite. The values are in good agreement with previous analyses of CM chondrites reported in the literature (e.g., *79*).

9. Chromium Isotopes

A sample of the Winchcombe meteorite (BM.2022,M3-33) was crushed to a fine powder using an agate pestle and mortar. Approximately 20 mg was weighed into a 5 mL Savillex Teflon high pressure vessel and dissolved in a 2:1 mixture of 29 M HF and 15.4 HNO_3 at 160 °C for three days. The meteorite sample was dissolved alongside geostandard USGS DTS2. After dissolution, the samples were evaporated to close to a gel, redissolved in 6 M HCl to avoid formation of insoluble fluorides, and then dried. They were redissolved in repeated steps of 6 M HCl and 7 M HNO_3 until fully in solution.

Chromium was purified using a 2-stage ion exchange procedure (*80, 81*). The first stage column was 4 mL of AG50W x8 in 1 M HCl; the samples were heated at 100 ºC for more than 18 hours in concentrated HCl then diluted to 1 M HCl immediately prior to loading on to precleaned and preconditioned resin and Cr was eluted with washes of 1 M HCl. Samples were dried and treated with concentrated HNO_3 to remove organics.

Next, the samples were dissolved in 0.5 M HNO_3:0.05 % H_2O_2 and allowed to equilibrate for five days. Solutions were then loaded onto 400 µL of precleaned and preconditioned AG50W x8. Matrix elements were eluted with washes of 1 M HNO_3 followed by elution of Cr with 6 M HCl. The samples were further dried and treated with concentrated HNO_3 to remove organics and prepare for analysis. Prior to analysis sample solutions were checked for adequate matrix separation and yield by analysis using an Agilent 8900 triple quad. The yield of the whole procedure was within error of 100 % and the total procedural blank was <40 ng of Cr and negligible compared to the ~20 µg of Cr in the smallest samples.

Samples were measured using a Thermo Finnigan Neptune Plus MC-ICPMS in the STAiG lab at the University of St. Andrews. The samples were aspirated using a 70 µLmin^{-1} nebulizer tip into a ESI Apex Omega desolvating nebulizer. Solutions were diluted to approximately 2 ppm, matched within 5 % to the bracketing standard, with the full analytical session consuming 8-10 µg of Cr per sample. A standard sample cone was used with an x-type high-sensitivity skimmer cone. Measurements were made in high-resolution mode with m/Δm > 8000 yielding a sensitivity of 25 V/ppm of ^{52}Cr. Beams of ^{49}Ti, ^{50}Cr, ^{51}V, ^{52}Cr, ^{53}Cr, ^{54}Cr and ^{56}Fe were simultaneously collected using cups L4, L2, L1, C, H1, H2, H4. Each was connected to amplifiers with 10^{11} Ω feedback resistors, except the cup collecting ^{52}Cr with a 10^{10} Ω feedback resistor and L1 collecting ^{51}V with a 10^{12} Ω feedback resistor. Samples and standards were 100 cycles of 8.439 s and blanks were 50 cycles of 4.197 s.

Peak center routines were performed before each sample and standard measurement to monitor and correct for magnet drift. The measurement position was offset to the low mass side of the peak to resolve molecular interferences, and the position of the peak edge and interferences were verified by peak flat measurements prior to each analytical session. All sample measurements were bracketed by on peak zero blank measurements and bracketing standard NIST SRM 979. Interference contributions from ^{50}Ti and ^{50}V on ^{50}Cr and ^{54}Fe were calculated from ^{49}Ti, ^{51}V and ^{56}Fe, respectively. These were within the ranges for which these corrections can be accurately applied (*82*).

The degree of mass-dependent fractionation of the interfering isotope ratios was estimated from the ^{50}Cr/^{52}Cr ratio and the interference ratios were adjusted accordingly before the interference signals were subtracted from the Cr isotope signals. Samples and standards were corrected for mass-dependent fractionation using the ^{50}Cr/^{52}Cr = 0.051859 (*78*) ratio and the exponential law. Samples were corrected for non-exponential drift and cup factors by calculating

the parts per ten thousand differences from the bracketing standard, yielding ε^{53}Cr and ε^{54}Cr. Due to an issue in the detector electronics, occasional outliers were present on only the largest beam (^{52}Cr), which were often very large and resulted in >5 σ outliers in the processed ratios. These did not influence the accuracy of the resulting data as they affected samples and standard alike but did artificially reduce the precision. The outliers were removed with a 3.25 σ outlier rejection on the normalized ^{53}Cr/^{52}Cr ratio. This level of rejection would have no effect on the data if no outliers were present.

The reproducibility of the resulting data was estimated using a pooled dataset (n = 26) yielding 2 SD external precision of 6.4 ppm for ε^{53}Cr and 16.9 ppm for ε^{54}Cr on a single measurement, and 3.2 ppm for ε^{53}Cr and 8.4 ppm for ε^{54}Cr 2se on a typical sample of n = 4. The accuracy of the analyses was verified with geostandard DTS2, which was within analytical uncertainty of previously reported ratios (*82*). Table S12 gives the Cr isotopic composition of the Winchcombe meteorite. The values are in good agreement with previous analyses of CM chondrites reported in the literature (e.g., *79*).

10. X-ray Diffraction

The mineralogy of the Winchcombe meteorite was initially characterized on the 9th March 2021 using a PANalytical X'Pert Pro scanning X-ray diffractometer at the NHM. Approximately ~5 mg of the powder BM.2022,M1-88 was mixed with several drops of acetone and deposited as a thin smear on a zero-background substrate. An XRD pattern of the sample was then collected using Co Kα radiation from 3 – 120° with a step size of 0.02° and time per step of 6.5 seconds, giving a total measurement time of ~12.5 hours. Mineral phases were identified using the International Centre for Diffraction Data (ICDD) database (PDF-2).

Fig. S9 shows the scanning XRD pattern of the Winchcombe meteorite, which is typical of CM chondrites. Intense peaks at ~14° and ~29° and a broader feature at ~23° are attributed to

abundant Fe- and Mg-bearing serpentines, while other minor phases identified from the pattern include olivine, magnetite, pyrrhotite, calcite and tochilinite.

The modal mineralogy of ~50 mg aliquots of three powdered (grainsize <50 μm) samples (BM.2022,M1-91 and BM.2022,M2-41, also analyzed by IR spectroscopy (Section 3) and ICP-MS (Section 6); BM.2022,M2-36, also analyzed for neon (Section 4)) was determined in May and June 2021 using an Enraf-Nonius PDS120 XRD equipped with an INEL curved 120° position-sensitive-detector (PSD) at the NHM. The PSD is in a static geometry relative to the primary X-ray beam and sample, meaning the only moving part of the instrument is the sample stage, which is rotated throughout an analysis. Each powder was packed into an aluminum sample well using the sharp edge of a spatula to minimize preferred crystal alignments and then analyzed using Cu Kα radiation. PSD-XRD patterns of the Winchcombe meteorite samples were collected for 16 hours and patterns of mineral standards were acquired under the same analytical conditions for 30 minutes.

Mineral abundances were calculated from the PSD-XRD patterns using a profile-stripping method (*83, 84*), whereby the pattern of a mineral standard was initially scaled to the same measurement time as the meteorite samples (e.g., ×32). The mineral standard pattern was then reduced by a factor to fit its intensity in the diffraction pattern of a meteorite before being subtracted to leave a residual pattern. This process was repeated for all phases present in the meteorites, resulting in final residuals with zero counts and the fit factors summing to one. The fit factors were corrected for relative differences in X-ray absorption to give final volume fractions in the meteorites. The detection limit was ~0.5 – 1.0 vol.% and the uncertainties were ~0.5 – 5 vol.% depending on the phase (see (*85*) for details).

The bulk mineralogy of the Winchcombe meteorite is summarized in Table S13. The most abundant phases were Fe- and Mg-bearing serpentines, with little difference found between the

three analyzed samples (87 – 93 vol.%). Similarly, each sample contained a much lower abundance (3.1 – 8.1 vol.%) of anhydrous silicates (olivine and enstatite). From these abundances, the phyllosilicate fractions (PSF = total phyllosilicate abundance / [total anhydrous silicate + total phyllosilicate abundance]) were calculated as 0.92 – 0.97, giving petrologic types of 1.2 – 1.1 on the alteration scale of (*86*). The bulk mineralogy of the Winchcombe meteorite is therefore consistent with highly altered CM chondrites (*87, 88*).

11. Petrographic Observations

11.1 *Analytical Procedures*

Two polished sections (P30423 and P30424) of the Winchcombe meteorite were prepared (without water) at the NHM and characterized using scanning electron microscopy (SEM) and energy-dispersive spectrometry (EDS) in March - July 2021. Secondary (SE) and backscattered electron (BSE) images, EDS point spectra, and large area, high-resolution EDS elemental maps were acquired under high vacuum using a ZEISS EVO 15LS SEM equipped with an Oxford Instruments AZtec EDS system and 80 mm^2 X-Max silicon-drift detector (SDD) based in the IAC of the NHM. Whole-section EDS maps were collected with a spatial resolution of ~1.9 µm/pixel at an accelerating voltage of 20 kV and beam current of 3 nA, resulting in output count rates of >50 kcps and deadtimes of ~30 – 60 %.

All EDS spot analyses were performed at a fixed working distance of 10.0 mm. An accelerating voltage of 20 kV and beam current of 1.5 nA resulted in an output count rate of ~40 – 60 kcps for silicate minerals. Prior to analysis, the EDS system was calibrated using a polished cobalt metal reference sample. Standards-based quantification was performed using the XPP matrix correction routine (*89*). For silicate minerals, quantification was performed using the "oxygen by stoichiometry" routine, while for carbonate minerals the "carbon by difference", and for sulphides and metals the "all elements", routines were used. The accuracy and precision for

major rock-forming silicate cations were cross-checked against analyses on the Smithsonian Kakanui augite reference sample, for which the composition is known from wet chemistry. Element detection limits were on the order of 0.1 – 0.3 wt.%.

A further 14 polished sections of the Winchcombe meteorite were prepared and characterized using SEM (Table S14). Polished sections P30540 and P30552 were investigated at the University of Glasgow using a Zeiss Sigma field-emission (FE-) SEM equipped with an Oxford Instruments X-Max EDS SDD and the AZtec/INCA software package. BSE images were acquired at an accelerating voltage of 20 kV and beam current of ~1 nA, and quantitative chemical spot analyses of individual mineral grains at 20 kV and ~2 nA. P30541 was studied at the University of Manchester using an FEI Quanta 650 FE-SEM operated under high vacuum. BSE images, EDS spectra, and elemental EDS X-ray maps were obtained with an accelerating voltage of 20 – 25 kV and beam currents of 3 – 6 nA. P30542 was studied at the University of Kent using a Hitachi S3400. Quantitative chemical analyses were acquired using an Oxford Instruments X-Max EDS SDD operated through the INCA software package. BSE images were obtained with an accelerating voltage of 20 kV and beam current of ~20 nA, and a combination of area and spot analyses were used to characterize individual minerals and fine-grained matrix. P30543 was studied using a FEI Quanta 650 FE-SEM at the University of Leicester Advanced Microscopy Facility. BSE images and EDS chemical compositions were acquired with an accelerating voltage between 5 and 20 kV and using Oxford Instruments AZtec software. P30545 was investigated by the Plymouth Electron Microscopy Centre at the University of Plymouth using a JOEL 7001F FE-SEM coupled with Oxford Instruments X-Max 50 mm^2 EDS detector. BSE images were acquired using an accelerating voltage of 20 kV and beam current of 5 nA, and both spot analyses and larger-area X-ray elemental maps were collected using Oxford Instruments AZtec software. Finally, the fusion crust in P30551, P30554, and P30555 was characterized using a Hitachi

TM4000Plus at Imperial College, London, with BSE images and X-ray element maps at acquired at 20 kV.

11.2 *Results*

A total area of 154.2 mm^2 across the 14 polished sections of the Winchcombe meteorite was characterized by SEM-EDS. In general, the sections were found to be typical of CM chondrites, consisting of chondrules, calcium-aluminum-rich inclusions (CAIs) and phyllosilicate clumps and/or tochilinite-cronstedtite intergrowths (TCIs), set within a matrix of finer-grained phyllosilicates, carbonates, Fe-sulfides, and magnetite. Many of the coarse refractory objects retain well preserved fine-grained rims (FGR).

Petrographic observations indicate that the Winchcombe meteorite is a breccia containing multiple lithologies (Fig. S10). The main lithology in the Winchcombe meteorite accounts for >50 % of the area analyzed in this study. In this lithology, chondrules are near-complete pseudomorphs, with most of their interiors replaced by Fe- and Mg-bearing phyllosilicates (Fig. S11 (a)). Anhydrous Mg-rich (Mg# >97) primary silicate minerals remain in ~20 % of the chondrules or occur as isolated grains (<2 area%, up to ~200 μm in length) in the matrix (Table S15). These show evidence for etching, dissolution, and corrosion, although some still retain enclosed Fe-Ni metal grains.

A small number of chondrules (<3 %) in the main lithology are calcitized (Fig. S11 (b)). These chondrule pseudomorphs, the main occurrence of carbonate in this lithology, are similar to the type 2 grains reported by (*90*). The compositions of the carbonates are relatively pure $CaCO_3$ with minor Mg (<3.0 wt.%) and Fe (0.3 – 3.3 wt.%) and trace Mn (Table S15). Intact CAIs are rare, with most showing replacement by carbonates and retaining only residual primary silicate minerals (Fig. S11 (c) and (d)).

The matrix comprises >80 area% of the main lithology and is dominated by a series of coarse, usually rounded to sub-rounded, phyllosilicate clumps with fibrous, porous, or meshwork textures that range in size from ~20 – 70 μm (Fig. S12). The cores of some clumps are Fe-rich (Mg# 36 – 61) and appear relatively homogenous in BSE images, while others have bimodal structures with Mg-enriched cores (Mg# 73 – 79) and Fe- and S-rich (avg. S = 4.4 at.%) rims (Table S15). The rims are fibrous with needle-like radiating acicular grains that extend into the core of the clump. In many examples, three or more phyllosilicate clumps occur in close proximity to form a single larger rounded object (Fig. S12 (b)). The phyllosilicate clumps are enclosed by finer-grained matrix materials that are darker in BSE images (Mg# 65 – 76). The matrix contains Ni-rich (24 – 34 wt.%) pentlandite with euhedral rounded or lath-shaped grains up to ~100 μm in size (Table S15), but magnetite was not observed.

The main lithology in the Winchcombe meteorite experienced a high degree of parent body aqueous alteration, which is reflected in the extensive replacement of chondrule silicates and metal, including the absence of any glassy mesostasis, the presence of type 2 calcite grains, the low FeO/SiO_2 and S/SiO_2 ratios of phyllosilicate clumps, and high Mg-content of the fine-grained matrix. Its mineralogical, chemical, and textural properties are consistent with a petrologic subtype of CM2.1.

Other lithologies in the Winchcombe meteorite were found to contain phyllosilicate clumps, TCIs, and multiple generations of calcite (Fig. S13). Several also have Mn-bearing dolomite, Fe-sulfides (usually pentlandite but pyrrhotite was also identified), magnetite framboids and platelets, and unusual, rounded grains of pure tochilinite penetrated by radial crack networks. Most lithologies typically consist of an abundant matrix of Mg-rich phyllosilicates, few or no surviving metal grains, and chondrules where >50 % of the primary anhydrous silicates have been replaced by phyllosilicates and/or carbonates. These features are all consistent with petrologic

subtypes of CM2.0 – 2.4. However, the dominant lithology in section P30541 is less altered, with largely unaltered chondrule silicates, abundant Fe-Ni metal in chondrules and matrix, sulfides consisting of pyrrhotite with pentlandite rims, and a high abundance of T0 calcites (Fig. S10c). Its mineralogy is consistent with petrologic subtype of CM2.6.

12. Transmission Electron Microscopy

12.1 *Analytical Procedures*

Thin lamellae were cut and extracted from polished sections of the Winchcombe meteorite using an FEI Helios Plasma Focused Ion Beam (FIB) instrument at the University of Glasgow and an FEI Quanta 200 3D FIB-SEM at the University of Leicester Advanced Microscopy Centre. In both cases, the protocol followed was similar to that outlined by (*91*). Briefly, the region of interest was initially coated with an ~1 µm thick bar of Pt deposited by a gas injection system to protect the sample. Lamellae were then milled to a thickness of ~1 mm, before being extracted using an *in-situ* micromanipulator and welded to a copper grid using platinum. After further milling to a thickness of ~100 nm, the lamellae were studied using transmission electron microscopy (TEM).

Lamellae from the matrix and FGRs within the polished sections P30540 and P30552 were initially characterized using an FEI T20 TEM at the University of Glasgow. An accelerating voltage of 200 kV was used to obtain diffraction-contrast images, high-resolution images, and selected area electron diffraction (SAED) patterns from the lamellae. High angle annular dark-field images and quantitative chemical analysis were also acquired at 200 kV using a JOEL ARM200F field-emission scanning TEM (STEM). For the analytical work, the X-ray spectra were acquired and processed using a Bruker Quantax EDS system with a 60 mm^2 SDD operating the Esprit V2.2 software. In addition, high resolution TEM imaging, calibrated STEM-EDS, and lattice spacing measurements of serpentine-like phases in lamellae extracted from polished section P30543 were performed mostly using a JEOL 2100 TEM at the University of Leicester Advanced

Microscopy Facility, as well as additional measurements using the JOEL 2100+ TEM at the University of Nottingham. Analyses used the Gatan Micrograph and Oxford Instruments AZtec software packages.

12.2 *Results*

TEM observations show that phyllosilicates are the main constituents of the matrix and FGRs. Both S-bearing and S-poor phyllosilicates are present; the latter with d_{001} spacings of ~0.70 – 0.74 nm, and the former with d_{001} spacings of ~0.62 – 0.70 nm. Lattice spacings with repeating units of two layers, consistent with 1:1 layered T-O phyllosilicates, are characteristic of serpentine-group minerals, as are the measured Mg-Fe silicate chemical compositions.

Crystals display a wide range of morphologies that are typical of CM carbonaceous chondrites (*92–95*), including tubular chrysotile (Fig. S14 (a) and (b)) and platy cronstedtite whose SAED patterns indicate characteristic stacking disorder (Fig. S14 (c) and (d)). Fibers of tochilinite are also abundant in some of the Winchcombe meteorite lithologies. The ~1.8 nm d-spacing of these crystals, together with high-resolution images, show that they are comprised of coherently interstratified intergrowths of tochilinite (d_{001} = 10.8 nm) with serpentine (d_{001} = ~7.3 nm) (*94*). The FGRs contain phyllosilicate crystals of widely different sizes, within which are organic nano-globules that have been partially replaced by the phyllosilicates (Fig. 6 (b)).

13. Bulk Magnetic Properties

13.1 *Analytical Procedures*

A MicroMag 2900 Series alternating gradient magnetometer (AGM) at the University of Cambridge was used to measure hysteresis loops, DC demagnetization (DCD) curves, and first order reversal curve (FORC) diagrams of chips taken from the Winchcombe meteorite samples BM.2022,M1-95 (3.3 mg) and BM.2022,M3-32 (11.4 mg). The FORC diagrams of the Winchcombe meteorite samples were compared quantitively to those of CI and CM chondrites using principal component analysis (PCA; (*96*)). In addition, an MFK1-FA MultiFunction

KappaBridge was used to measure the mass specific magnetic susceptibility of 80.2 mg and 75.3 mg chips of BM.2022,M1-95 and BM.2022,M3-32, respectively.

Hysteresis loop measurements were conducted using an applied saturation field of 1 T, an averaging time of 200 ms, and a field increment of 10 mT. Paramagnetic adjustment was conducted to remove the effect of paramagnetic minerals in the samples. DCD curves were measured using an applied saturation field of 1 T, an initial field of 0 T, a maximum reverse applied field of -500 mT, and an averaging time of 1 s. A non-linear field sequence was used with 150 points measured.

FORC diagram measurements were conducted using a 1 T saturating field, a 2.09 mT field-step size, and an averaging time of 275 ms. Three hundred FORCs were measured for each sample. The FORC diagrams were processed using the VARIFORC approach (*97*) within the FORCinel software package (*98*). During smoothing, a value of 0.2 was used for the horizontal and vertical lambda values (λ). Vertical ridge, central ridge, horizontal smoothing, and vertical smoothing parameters of 8, 5, 12 and 12, and 6, 6, 10 and 10, were used for chips BM.2022,M1-95 and BM.2022,M3-32, respectively. PCA was conducted on the processed FORC diagrams using the FORCem software package along with CM1 and CI1 chondrites (*96, 99*).

Mass specific magnetitic susceptibility measurements were conducted using an AC field amplitude of 200 Am^{-1} and a frequency of 976 Hz. Five measurements of each chip were taken, and the average recorded.

13.2 *Results*

Figs. S15 (a) and (b) show the hysteresis loops for chips BM.2022,M1-95 and BM.2022,M3-32. Saturation magnetization (M_S), remanence magnetization (M_{RS}), coercivity (H_C), coercivity of remanence (H_{CR}), mass specific magnetic susceptibility (χ), and the S300 ratios of the measured Winchcombe meteorite are given in Table S16. The mass normalized M_S and M_{RS} values, and the H_C, H_{CR}, and mass specific magnetic susceptibility (χ) (provided here as log(χ))

values of the Winchcombe meteorite fall into the lower range of values reported for CM chondrites (*96, 100, 101*). The S300 ratios of chips BM.2022,M1-95 and BM.2022,M3-32 fall into the higher range exhibited by the CM chondrites, indicating higher abundances of magnetite relative to magnetic pyrrhotite (*101*).

Figs. S15 (c) and (d) show FORC diagrams of chips BM.2022,M1-95 and BM.2022,M3-32. Both FORC diagrams show similar characteristics, including a prominent central ridge that extends to ~0.1 – 0.15 T, characteristic of <0.1 μm single domain (SD) magnetic grains (*102*) and similar to previous analysis of CM chondrites (*96*). Chip BM.2022,M1-95 displays a more extensive, symmetrical vertical spreading cantered near the origin, which indicates the presence of interacting vortex (Int-V) and/or larger, multi domain (MD) grains (*103*). A similar signal is observed in carbonaceous chondrites that contain magnetite framboids (clustered and magnetically interacting, 0.1 – 5 μm grains of magnetite), such as the CI chondrites, and the $C2_{ung}$ chondrites Tagish Lake and WIS 91600 (*96, 104, 105*).

Fig. S15 (e) shows PCA of the Winchcombe meteorite FORC diagrams alongside CI and CM chondrites with petrologic grades of 1.0 – 1.3 on the alteration scale of (*86*). The previously measured CI and CM chondrite FORC diagrams define endmembers in a region of PCA space within which most of the highly aqueously altered samples plot. The CM chondrites define a linear trend between two endmembers (smaller, <0.1 μm, SD magnetic grains, and slightly larger, 0.1 – 5 μm, V state magnetic grains), with the CI chondrites defining a third endmember (corresponding to closely packed, interacting magnetic assemblages, i.e., framboids and plaquettes). Both analyzed Winchcombe meteorite chips plot within the identified region enclosed by the end members, although notably closer to the Int-V/MD endmember defined by the CI chondrites rather than most other CM1.0 – 1.3 chondrites. This suggests the presence of more framboid and plaquette magnetite in the Winchcombe meteorite compared to other CM chondrites.

14. Computed Tomography

14.1 *Analytical Procedures*

The internal and external features of 20 fragments of the Winchcombe meteorite (<0.01 – 0.36 g) were imaged using micro X-ray computed tomography (XCT) in July and August 2021 in the IAC of the NHM. For analysis, fragments were mounted in gel capsules with supporting foam and loaded into modified pipettes (~7 mm in diameter; 1 to 2 fragments per pipette), which were then fixed onto the stage of a cabinet-based industrial Zeiss Xradia Versa 520 CT system. X-rays were generated from a tungsten source using a voltage of 70 – 130 kV and a current of 76 – 87 µA. Appropriate X-ray source filtration was used to help reduce beam hardening effects.

For each fragment a total of 1601 – 3201 projections were collected while it was rotated by 360°. The center shift during stage rotation was corrected in post-processing using the Zeiss Reconstructor software. Each projection was magnified by a 4X or 0.4X objective lens and then recorded using a 2000 × 2000 CCD plane (16-bit pixel depth) with an exposure of 3 – 20 seconds. Spatial resolutions (in voxels) were 1.17 – 4.59 µm, depending upon the size of the analyzed fragment, and beam hardening was corrected for the XCT images with a constant value of 0.05.

To conduct petrofabric measurements, the data were loaded into the Avizo software, and a non-local means filter was applied to reduce noise in the images. Non-local means filter parameters were: search window –9, local neighbor –4, and similarity value –0.4. Chondrules were identified within the XCT data by a difference in X-ray attenuation when compared to the matrix (i.e., darker appearance) and the presence of FGRs. Following identification, a representative section of each chondrule was manually segmented in each of the three orthogonal planes (XY, XZ and YZ) using the Avizo manual segmentation draw tool. A fit ellipsoid was fitted to the outer margins of these segmented sections and measured using the Blob3D software. The resulting directional cosine data for the orientation of the long and short shape axis of the ellipsoid was then converted into trend

and plunge before being plotted on an equal area stereonet using the Stereonet 11 software. A stereonet illustrating chondrule orientation was produced for each visible lithology to determine whether any petrofabrics (e.g., random, planar, lineation) were present.

To calculate the macro porosity of the Winchcombe meteorite fragments BM.2022,M2-34 (0.24 g) and BM.2022,M3-31 (<0.01 g), the XCT data were loaded into Avizo, and a total of five internal sub-volumes were extracted from the dominant lithologies present. The sub-volumes were then segmented using a general thresholding technique to approximately extract the macro-scale pores and fractures. Following segmentation, a small spot removal function was applied to remove regions of less than five connected voxels in an attempt to reduce noise. Once macro-porosity was segmented, a material statistics function was applied to ascertain the number of voxels segmented as pore space.

14.2 *Results*

XCT imaging of the chips highlighted the diversity of lithologies in the Winchcombe meteorite. In total, 15 of the fragments were analyzed for evidence of petrofabrics; eight contained lithologies possessing weak-moderate, chondrule defined petrofabrics. All of the observed petrofabrics were characterized by long shape axis orientations plotting along a great circle girdle and short shape axis orientations clustering, a pattern indicative of foliation. Within three fragments (BM.2022,M1-84, 0.36 g; BM.2022,M2-34; BM.2022,M4-34, <0.01 g), multiple lithologies were distinguished by a difference in X-ray attenuation. In sample BM.2022,M2-34 three distinct lithologies were identified, two of which exhibited petrofabrics orientated in different directions (Fig. S16). In addition to chondrule defined petrofabrics, one fragment (BM.2022,M1-84) was characterized by a fracture defined fabric (Fig. S16). An average fracture trend of 156.1° relative to the top of the XCT slices was observed.

Macro-scale porosity extracted from four sub-volumes within BM.2022,M2-34 ranged from 0.56 – 4.21 %. Three sub-volumes were observed to contain cross-cutting fractures, producing porosity values >1.5 %. Sub-volume four was not observed to have cross-cutting fractures and consequently recorded a reduced porosity of 0.56 %. Within the sub-volume extracted from BM.2022,M3-31, a small cross-cutting fracture was observed, which was reflected in a porosity value of 0.99 %.

15. Thermogravimetric Analysis

Approximately 45 mg of the Winchcombe meteorite powder BM.2022,M1-88 was characterized on the 5th March 2021 using a TA Instruments Simultaneous Thermal Analysis (SDT) Q600 at the NHM. The powder was loaded into an alumina crucible and placed onto the TGA balance within a furnace that was then sealed. The mass of the sample was recorded as it was heated from ~15°C to 1000°C at 10°C min^{-1} under a N_2 flow of 100 ml min^{-1}. The sensitivity of the TGA balance is 0.1 µg and the overall error on the measured mass loss fractions is ~0.1 % (*106*).

Previous studies of hydrated carbonaceous chondrites have divided TGA curves into distinct temperature regions: (a) mass loss <100°C is attributed to the removal of adsorbed terrestrial water, (b) from 100 − 200°C mainly to the breakdown of sulphates, (c) between 200 − 400°C and 400 − 770°C due to the release of -OH/H_2O in Fe-(oxy)hydroxides and phyllosilicates, respectively, and (d) between 770 − 900°C from CO_2 produced during the breakdown of carbonates (*106, 107*). Additional mass loss in these temperature ranges could also result from the decomposition of Fe-sulfides and refractory organic matter, although the contribution is expected to be small.

Table S17 summarizes the mass loss in each temperature region for the Winchcombe meteorite. The total mass loss during heating from 15 – 1000°C was ~15 wt.%. The Winchcombe

meteorite showed a mass loss at <100°C from terrestrial adsorbed water of 2.4 wt.%, similar to other CM chondrite falls and finds (Fig. S17). In contrast, the Winchcombe meteorite mass loss between 100 – 200°C was only 0.6 wt.% and lower than all other analyzed CM chondrites, except for a few highly altered hot desert finds. For CM chondrites, the main cause of mass loss in this temperature region is the breakdown of terrestrially formed sulphates, which is usually observed as a peak in the derivative curve at ~120°C. However, this peak was not seen for the Winchcombe meteorite, indicating low terrestrial contamination and modification.

Assuming all mass loss from 200 – 770°C was due to the dehydration and dehydroxylation of Fe-(oxy)hydroxides and phyllosilicates, the water abundance of the Winchcombe meteorite was calculated as 11.2 wt.%. This agrees with values of Winchcombe samples analyzed using stepped pyrolysis (Section 16) and is consistent with other highly altered CM chondrites (*51*).

16. Hydrogen Pyrolysis

The abundance and isotopic composition of hydrogen in the Winchcombe meteorite was analyzed by stepwise pyrolysis at the Scottish Universities Environmental Research Centre (SUERC). Two chips (BM.2022,M2-39, which split into two chips during transport) sealed in glass vials on the 16th March 2021, were transferred to a desiccator on the 18th March 2021. The smaller chip (BM.2022,M2-39-a, 45.1 mg) was put under vacuum on the 19th March 2021 before analysis on the 23rd and 24th March 2021. The other chip was put under vacuum on the 24th March and subsequently split into two subsamples: BM.2022,M2-39-b (32.7 mg) and BM.2022,M2-39-c (30.9 mg). Sample BM.2022,M2-39-b was analyzed on the 26th March 2021 and BM.2022,M2-39-c on the 30th March 2021.

Chips rather than powders were analyzed in order to minimize the potential for terrestrial contamination (*25*). Each chip was placed in a previously outgassed (to 1100°C) Pt crucible within an all-glass vacuum line, pumped down overnight, and then incrementally heated via a

temperature-controlled resistance furnace (25 – 700°C) and temperature-controlled induction furnace (>700°C) over seven steps: 100, 200, 300, 400, 500, 700, and 1100°C (± 5°C). The samples were held at each temperature for at least 30 minutes. Released gases were first stored in a cold trap at −196°C using a liquid N_2 bath, which was then replaced by a mixture of dry ice and acetone at −78°C, trapping water but releasing other gases. The yield of gas that was not trapped at −78°C was measured using an Edwards PR10-C Pirani vacuum pressure gauge. The dry ice and acetone bath was then removed from the cold trap, which was gently heated to release the water. This water was released to H_2 by exposure to Cr powder at 850°C (*108*). The yield of hydrogen in each step was measured using the Pirani vacuum pressure gauge, and the H_2 was collected with a mercury Toepler pump into a small borosilicate vessel with Teflon-sealed high-vacuum valves. The vessels were immediately taken to a VGI Optima mass spectrometer for hydrogen isotope analysis. In-run repeat analyses of water standards (international standards GISP and V-SMOW, and internal standard LT-STD) gave a reproducibility of better than ± 2 ‰ for δD. Table S18 summarizes the data and Fig. S18 shows the abundance and isotopic composition of hydrogen released during the stepped pyrolysis.

The bulk water content of the Winchcombe meteorite chips was calculated by excluding the releases at <200°C due to possible terrestrial modification. This resulted in water abundances of 9.3 wt.% for BM.2022,M2-39-a, 10.7 wt.% for BM.2022,M2-39-b and 11.4 wt.% for BM.2022,M2-39-c, giving an average for the Winchcombe meteorite of 10.5 ± 1.1 wt.%, in good agreement with the estimate from the TGA (Table S17). Excluding the low temperature steps yielded bulk δD values of −145.8 ‰ for BM.2022,M2-39-a, −138.6 ‰ for BM.2022,M2-39-b, and −140.2 ‰ for BM.2022,M2-39-c, resulting in an average for the Winchcombe meteorite of −142 ± 4 ‰.

17. Carbon and Nitrogen Pyrolysis

17.1 Analytical Procedure

Small chips of Winchcombe meteorite samples BM.2022,M1-85 (5.0502 mg) and BM.2022,M1-86 (5.0981 mg) were analyzed at the Open University using the Finesse system, which can simultaneously measure the abundance and isotopic compositions of He, Ne, Ar, Xe, N, and C (*109–111*). Gases are released by heating the sample in a double-vacuum furnace in which a quartz glass inner tube is separated from the outer corundum tube by an evacuated space.

For analysis of the Winchcombe meteorite, each chip was loaded into a Pt foil (25 mm thick) capsule and dropped into the extraction furnace through a gate vale, and then heated at ~100 °C for 0.5 h under pumping to decrease atmospheric contamination. The samples were analyzed using a high-resolution temperature program of 25°C steps from 100°C to 600°C, the temperature range over which most of the carbonaceous matter combusted. Temperature steps of 50°C or 100°C were employed at higher temperatures as the amount of combustion products decreased. Released gases were separated into fractions ((CO2 + Xe), (He + Ne), (N2 + Ar)) using a combination of cold fingers, molecular sieves, and getters (*109–111*). All the volumes of the vacuum system are calibrated, so the proportion of the total amount of a gas included in one or another fraction is precisely known. The amount of CO_2 was determined by pressure measurement using a Baratron^{TM} capacitance monometer to a precision of better than ±1 %.

The system has magnetic sector mass spectrometers, each equipped with three collectors set for masses (m/z) of 28, 29, and 30 (for N_2) and 44, 45, and 46 (for CO_2). A single measurement lasted ~1 minute, during which ~300 data points were collected for each isotope, providing a precision of 0.3 – 0.5 ‰. Calculation of $\delta^{13}C$ and $\delta^{15}N$ was achieved through analysis under identical conditions of appropriate standards measured alternately with the samples (*109–111*).

The laboratory standards were calibrated using NBS standard calcite (for CO_2) and air (for noble gases and N_2).

The system blank was determined prior to analysis of the Winchcombe meteorite by stepped combustion of an empty Pt foil capsule over the same temperature range as the sample. The contribution from the system blank at temperatures below 600°C was negligible for C and N and not more than 10 % for the noble gases. Above 600°C, correction for system blank becomes more significant as the amount of gas released from the sample decreases. However, the gas-rich nature of the Winchcombe meteorite ensured that even at the highest temperatures, the contribution from the blank was less than about 20 % of the released nitrogen and noble gases and 5 % of the CO_2.

17.2 Carbon and Nitrogen

Carbon and nitrogen data from stepped combustion of samples BM.2022,M1-85 and BM.2022,M1-86 are summarized in Figs. S19 and S20 and Tables S19 and S20. The carbon abundance and isotopic composition are typical of CM chondrites (*23*, *112*). The two samples exhibited very similar behavior on combustion, although there are subtle differences that illustrate the heterogenous nature of the Winchcombe meteorite.

The bulk of the carbon occurs as organic matter, combusting below 500°C. Variation in isotopic composition within this temperature range indicates that at least three different organic components are present, with $\delta^{13}C$ between −20 ‰ and +15 ‰. The material released on combustion between room temperature and 100 °C has a $\delta^{13}C$ around 0 ‰ and may correspond with the species identified by selected ion flow tube-mass spectrometry (SIFT-MS) (Section 18). The isotopically lighter material combusting between 350 – 500 °C is likely to be the abundant macromolecular material known to occur in CM chondrites (*113*), almost certainly mixed with CO_2 from nanodiamonds (*114*). A second maximum in carbon yield carbon occurs at 600 °C with

$\delta^{13}C$ between +40 ‰ and +60‰; comparison with other CMs suggests that this is carbonate, probably calcite (*115*). At least one of the components has $\delta^{13}C$ of at least +150 ‰, probably from a mixture of presolar graphite and SiC (e.g., *116*).

Like carbon, the abundance and isotopic composition of nitrogen in the Winchcombe meteorite are typical of CM chondrites (*23, 112*), with both samples exhibiting similar behavior on combustion. The combustion profiles are dominated by release of nitrogen from organic matter: there is a maximum at 250 – 300 °C, which accounts for ~10 % of the total nitrogen, with $\delta^{15}N$ around +50 ‰. This component is unresolved in carbon data, but the nitrogen isotopic composition is characteristic of meteoritic organic acids (*117*). The bulk of the nitrogen, though, like the carbon is from combustion of macromolecular material, depleted in both ^{15}N and ^{13}C relative to the less refractory organics (*118*). The sharp and pronounced drop in $\delta^{15}N$ at 400°C is a sign that nanodiamonds are co-combusting with the organic material. Above 600 °C, we see separate presolar components enriched and depleted in ^{15}N – also evidence of presolar graphite and SiC (*116*).

17.3 Noble Gases

Table S21 gives the total concentration (in cm^3 STP g^{-1}) of ^4He, ^{20}Ne, ^{36}Ar, and ^{132}Xe in the Winchcombe meteorite samples BM.2022,M1-85 and BM.2022,M1-86. The concentrations are generally an order of magnitude higher than observed in typical CM meteorites (e.g., (*15*)), where planetary (or Q-type) noble gases dominate. The Ne isotopic composition of the individual temperature steps mostly plot on the mass fractionation line (MFL) indicating the presence of fractionated solar wind (SW) (Fig. S21), implying that the meteorite is from the regolith of its parent body where it was irradiated by SW particles. However, since the MFL is indistinguishable from the SW-Q mixing line, a contribution from Q cannot be ruled out. Its presence is clearly visible in sample BM.2022,M1-85, which has a lower Ne content than BM.2022,M1-86. In the

latter case, some data points plot above SW composition indicating higher contribution of the (fractionated) SW component.

Fig. S21 shows that some data points fall of the SW-Q mixing line, lying within the SW-Q-COSM triangle, suggesting the presence of cosmogenic Ne. This is more pronounced for BM.2022,M1-85, which has a lower overall concentration of Ne. The calculated concentration of cosmogenic ^{21}Ne in 1a-85 is $(1.6 \pm 0.8) \times 10^{-9}$ cm^3 STP g^{-1}, which corresponds to a ^{21}Ne CRE age of 0.55 (± 0.3) Ma (assuming a $^{21}Ne_{cosm}$ production rate of 0.288×10^{-8} cm^3 g^{-1} yr^{-1} established for CM meteorites by (*119*)). This age is slightly longer than those measured in samples BM.2022,M2-36 and BM.2022,M4-7 (Sections 4 and 5) but still close to the main cluster of exposure ages for CM meteorites (*15*).

18. Selected Ion Flow Tube-Mass Spectrometry

The profile of C_1 to C_6 alcohols, aldehydes, ketones, and carboxylic acids present in Winchcombe meteorite samples BM.2022,M1-85 (17.8 mg) and BM.2022,M1-86 (15.7 mg) were determined within ten months of collection. The chips were placed into 20 ml cleaned glass vials, with the headspace flushed with dry nitrogen. Volatile species were then analyzed using selected ion flow tube-mass spectrometry (SIFT) at Anatune Ltd, Cambridge, UK following their release into the vial headspace, after heating to 150 °C for 15 minutes. An empty vial was processed in the same way to act as a blank.

Fig. S22 shows that no significant differences were found between the samples and there was a general decrease in abundance with increasing carbon number. Aldehydes and ketones were found to be the most abundant species present, followed by alcohols and then carboxylic acids. This profile is consistent with previous reports of ultraviolet (UV) emissions from the CM chondrite Murchison and analysis of volatiles by proton-transfer reaction mass spectrometry (PTR-MS) (*120*), but significantly different from the results of (*121*), who concluded that by solvent

extraction, carboxylic acids are the most abundant free compounds in Murchison and dominate the free organic inventory. The low level of carboxylic acids determined by both the thermal and UV method is likely due to the carboxylic acids being present in their salt form, thus thermally stable and non-volatile.

19. Low Voltage SEM-EDS

On the 11th March 2021 17 fragments (~0.5 – 8 mm in size, from Site 1) of the Winchcombe meteorite were mounted using cleaned stainless-steel tweezers onto carbon-based electrically conductive, double-sided adhesive discs, also known as Leit tabs, stuck to the flat surface of two aluminum SEM pin stubs. The uncoated and unpolished fragments were then quickly transferred to an FEI Quanta 650 FE-SEM at the IAC of the NHM.

The FE-SEM is equipped with a Bruker Quantax EDS system with a high-sensitivity, annular, four-channel Bruker FlatQUAD SDD inserted between the pole piece and sample within the main chamber of the SEM. The annular geometry allows sufficient data collection on uncoated, beam sensitive and non-conductive samples with substantial surface topography using ultra low beam currents under high vacuum (*122*). An accelerating voltage of 6 kV and 9 kV and a beam current of 30 – 190 pA was used, resulting in an input count rate up to 55 kcps. Several of the fragments were initially mapped at 3 and 4 µm pixel resolution using automated stage control to identify features of interest, which were then further analyzed at a pixel resolution down to 16 nm. Follow-up SEM imaging of the features of interest was carried out in the variable pressure mode of the SEM using a low-vacuum cone.

Many fragments were found to be coated in micrometer to sub-micrometer sized particles with the same composition as the bulk meteorite fragments, suggesting that they are highly electrostatic in nature. The fragments were composed mainly of silicate minerals, with carbonate, phosphate, and sulfide minerals also present throughout. Despite mapping the fragments over

several days, there was no evidence for phases such as halite or other salts, elemental sulfur or oldhamite. However, carbon- and nitrogen-rich areas were observed heterogeneously distributed within the fragments. High resolution imaging revealed the regions (typically ~10's μm in size) to be carbonaceous, likely organic materials, often with "globule-like" morphologies (Fig. S23). Based on their textural settings (i.e., clearly within the meteorite matrix), and also the rapid recovery and minimal handling of the fragments prior to analysis, the carbonaceous materials are interpreted as being indigenous to the Winchcombe meteorite. Furthermore, in some instances, they are intimately associated with minerals, such as carbonates, that are expected to have formed from extraterrestrial fluids on the asteroid parent body.

20. Liquid Chromatography-Mass Spectrometry

20.1 *Samples*

The Winchcombe stones BM.2022,M2-23 and BM.2022,M9-4 were crushed using an agate pestle and mortar to a grainsize of <0.1 mm, with six ~50 mg aliquots then taken from each powder. For both samples, three of the aliquots were initially analyzed using untargeted liquid chromatography-mass spectrometry (LC-MS), and three were subsequently analyzed using targeted LC-MS (*123*). Six ~50 mg environmental soil controls from Site 1 and Site 6 (Table S4) were also analyzed to identify terrestrial organic molecules in both locations. Fig. S24 summarizes the samples and analytical workflow.

20.2 *Solvent Extractions*

All samples and environmental controls were crushed using an agate mortar and pestle at SUERC. The mortar and pestle were cleaned with 2% DECON solution, followed by ultrapure water, then acetone, and was dried in a positive pressure fume hood environment in between uses.

Solvent extractions were all performed in a positive pressure fume hood. Glassware and metal tools were wrapped in foil and placed in a furnace overnight at 450°C. All glassware, ceramics, and tools were then washed in 2% DECON clean solution and rinsed with ultrapure

water and acetone in between uses for different samples. After crushing, three ~50 mg replicates from each powder were weighed out and placed in new sterile PTFE screw-top vials.

Three procedural blanks (new empty vials opened at that stage) were added at each step of the extraction to pick-up any contaminants in the laboratory, starting at the crushing step, with blanks introduced for each new solvent, as well as the pooling and filtering step.

Solvent extractions were performed by adding 1 ml of each solvent to each powdered sample using a Gilson pipette (with a new sterile tip each time) and mixing using a vortex for 10 minutes at room temperature. Hexane was the first solvent added and mixed, then dichloromethane, and finally methanol. These solvents were used to target a broad range of apolar to moderately polar molecules. Each solvent was added, mixed, removed, and then placed in a new vial, using fresh pipette tips before the next solvent was added. 330 µl of each solvent extract was then pooled and mixed in a fresh vial to make up a 990 µl extract, which was then removed using a hypodermic needle and syringe (with needles rinsed with a 1:1:1 sterile solvent mixture between uses, and a fresh needle used every five samples), and finally filtered using a 0.45 µm filter, leaving behind ~80 µl, which was placed in a fresh vial, ready for LC-MS analysis.

These pooled and filtered extracts were frozen in PTFE screw top vials at ~ −10°C until LC-MS analysis. Three procedural blanks (fresh vials with solvent added only from that step onwards) were added at each new extraction step to identify the introduction of any laboratory contaminants.

20.3 *LC-MS*

Hydrophilic interaction liquid chromatography (pHILIC) was carried out on a Dionex UltraMate 3000 RSLC system using a ZIC-pHILIC column (150 mm × 4.6 mm, 5 mm column, Merck Sequant) at the Polyomics Facility, University of Glasgow. The column was maintained at

25°C and samples were eluted with a linear gradient (20 mM ammonium carbonate in water, A and acetonitrile, B) over 26 minutes at a flow rate of 0.3 ml min^{-1} (Table 22).

The injection volume was 10 µl and samples were maintained at 5°C prior to injection. A Thermo Orbitrap QExactive was operated in polarity switching mode and the MS settings were as follows: resolution, 70,000; AGC, 1×10^6; *m/z* range, 70 – 1050; sheath gas, 40; auxiliary gas, 5; sweep gas, 1; probe temperature, 150°C; capillary temperature, 320°C.

For positive mode ionization the source voltage was +3.8 kV; S-Lens RF level, 30.00; S-Lens voltage, 25.00 V; skimmer voltage, 15.00 V; inject flatopole offset, 8.00 V; bent flatopole DC, 6.00 V. For negative mode ionization the source voltage was −3.8 kV. The calibration mass range was extended to cover small metabolites by inclusion of low-mass calibrants with the standard Thermo calmix masses (below *m/z* 138), butylamine ($C_4H_{11}N$) for positive ion electrospray ionization (PIESI) mode (*m/z* 74.096426) and COF3 for negative ion electrospray ionization (NIESI) mode (*m/z* 84.9906726). To enhance calibration stability, lock-mass correction was also applied to each analytical run: Positive mode lock masses: Number of lock masses: 1 lock mass #1 (*m/z*): 144.9822; Negative mode lock masses: Number of lock masses: 1 lock mass #1 (*m/z*): 100.9856

Instrument .raw files were converted to positive and negative ionization mode mzXML files. These files were processed with IDEOM (*124*), which uses the XCMS (*125*) and mzMatch (*126*) software in the R environment. Briefly, this involves using the CentWare algorithm within XCMS to pick-out signals based on their retention time and mass-to-charge ratio. These signals are then grouped based on sample replicates and filtered using relative standard deviation, minimum intensity, and a noise filter to produce a set of signals that are likely to be due to real metabolites.

Finally, a gap-filling step was employed to ensure that signals that may have been missed or lost from a particular group/groups while retained for another group were re-instated, to avoid erroneous identification of signals unique to a particular sample. Fragmentation data were analyzed in PiMP (*127*) with the FrAnK in-house fragmentation data analysis software. Comparisons between the overall metabolite distributions of the samples were made using Metaboanlyst (*128*).

20.4 *Results*

PCA of untargeted LC-MS data indicated that the solvent extracts from both meteorite chips contained many organic molecules in common with each other, but not present in the environmental samples (Fig. S25). This suggests that despite the detection of a number of likely contaminants (molecules found in the soil sample extracts, as well as the meteorite extracts), a significant amount of indigenous extraterrestrial organic matter remained in the meteorite chips.

Fig. S25 shows that the six Winchcombe meteorite extracts cluster closely together, whilst the environmental samples cluster away from both the meteorite extracts and each other. The first principal component shown on Fig. S25 is responsible for 75.1 % of the variance in the distribution of the organic molecules in the extracts, leading to the separation of the Winchcombe meteorite extracts from the environmental samples. This close clustering of the Winchcombe extracts, and the relatively high variance which PC1 accounts for, further suggests that there was minimal contamination, and much of the indigenous organic material remained in the meteorite.

A large number (>200) of organic molecules were detected at high intensities in the Winchcombe meteorite extracts from both Site 1 and Site 6 but were below the detection limits in the environmental samples. Approximately 10% of these were identified as organic sulfonate compounds, with several alkyl sulfonate of various chain lengths (ethanesulfonate, propanesulfonate, pentanesulfonate, and hexanesulfonate). Organic sulfonates have previously been detected in the Murchison CM2 chondrite (*129*).

21. Gas Chromatography-Mass Spectrometry

21.1 *Samples, Chemicals and Materials*

Gas chromatography-mass spectrometry (GC-MS) was used to characterize the amino acid content of a Winchcombe meteorite stone (BM.2022,M2-14) and nearby soil sample (the "fall site soil"). A powdered sample of serpentinized peridotite from Kennack Sands, UK, was also analyzed as a procedural blank. The procedural blank was heated to 500°C in air for 24 hours prior to the amino acid extraction procedures. Stock solutions (10^{-3} M to 10^{-1} M) of individual amino acids were made by dissolution of standard crystals in ultrapure water. An amino acid standards mixture was made by combining individual standard solutions. The amino acid standards mixture, procedural blank, and fall site soil were subjected to the same experimental procedures as the meteorite sample.

All tools, glassware, and ceramics were sterilized by baking at 500°C in air for 24 hours. Millipore ultrapure water (18.2 MΩ cm, ≤3 ppb total organic carbon) was used for all laboratory work performed in this study. The amino acid 3-amino-3-methyl butanoic acid and 3-amino-2,2-dimethylpropanoic acid were provided by the Astrobiology Analytical Laboratory at Goddard Space Flight Center, NASA. All other amino acid standard crystals/powder were purchased from Acros Organics, Sigma-Aldrich, and Fluka. Hydrochloric acid (HCl) (37 %), ammonium hydroxide (NH_4OH) (28 – 30 wt.%), isopropanol (IPA) (99.5 %), and trifluoroacetic anhydride (TFAA) (>99.0 %) were purchased from Sigma-Alrich. Acetyl chloride (99+ %) and pyrene (98 %) were from Acros Organics. Prepacked columns, analytical grade 50W-X8, hydrogen form (100 – 200 mesh) were acquired from BIORAD®. Sodium hydroxide (NaOH) pellets and dichloromethane (DCM) (99.8+ %) were purchased from Fisher Scientific.

21.2 *Sample Extraction and Desalting Procedures*

The Winchcombe meteorite sample was powdered, split into five equal portions, and transferred to individual test tubes (20 × 150 mm) for hot-water extraction. Ultrapure water (1 ml)

was added to each sample. The test tubes were then flame-sealed and heated to 100°C for 24 hours in a heating block. After cooling to room temperature, the test tubes were rinsed with ultrapure water, cracked open, and centrifuged for 5 minutes. 80 % of the water supernatant was transferred to small test tubes (12 × 75 mm) individually, dried under vacuum, flame-sealed in a larger test tube (20 × 150 mm) containing 1 ml of 6 N HCl, and then subjected to acid vapour hydrolysis for 3 hours at 150°C to determine the total (free + bound) amino acid content. 15 % of the water supernatant (the non-hydrolyzed fraction) was transferred to small test tubes and kept in a fridge until prior to the desalting procedure. After the hydrolysis procedure, the test tubes were rinsed with ultrapure water, and then cracked open. The small test tubes were removed and dried under vacuum.

Cation exchange was performed on prepacked columns. The columns were prepared according to the following procedures. After removing the caps and snapping off the seals on the Luer tips, the columns were filled to the top with water (~10 ml) plus one bed volume (~2 ml). Once the volume of water was just above the resin bed, three bed volume (~6 ml) of 2M NaOH was added to desorb any contaminating amino acids. The columns were then washed by filling to the top with water twice (20 ml) until the eluting solution had a neutral pH to remove residual NaOH. Three bed volume (~6 ml) of 1.5 M HCl was added to re-acidify the columns. The columns were again washed with two volumes of water (20 ml) to remove excess HCl until neutral pH.

Both hydrolyzed and non-hydrolyzed samples were then brought up in 3 × 1 ml of ultrapure water and desalted on the cation exchange resin. Different fractions of the same sample were re-combined by desalting in the same column. Purified amino acids were eluted by adding 2 × 3.5 ml fractions of 2M NH_4OH, and the eluates were collected in small test tubes, which were then evaporated to dryness by vacuum centrifugation.

21.3 *TFAA-IPA Derivatization and GC-MS Analysis*

Prior to GC-MS analysis, amino acids were derivatized by esterification with IPA and acylation with TFAA. The samples were re-suspended in 2 × 50 µl of ultrapure water in inserts within GC vials. 100 µl of acetyl chloride:IPA mixture (30:70 v/v) was added to each of the samples. The vials were tightly capped, and the samples were heated in a heating block set at 110°C for 1 hour. The samples were then cooled in an ice bath and dried under a gentle stream of dry N_2. After the samples were brought to room temperature, 100 µl of DCM and 50 µl of TFAA were added to the dried sample. The vials were capped tightly again and heated to 100°C for 10 minutes. The samples were then cooled to room temperature and the excess reagent was removed under a slow stream of N_2. Prior to injection the derivatized samples were dissolved in 30 µl of DCM and 5 µl of pyrene in DCM (200 µg/ml) as an internal standard. The derivatized samples were then immediately analyzed by GC-MS.

Amino acids in the hot water extracts were analyzed by an Agilent Technologies 7890A series GC coupled to an Agilent Technologies 5975C mass selective detector (MSD). The separations of the D, L-amino acid enantiomers were achieved using a CP-Chirasil-L Val GC Column (25 m × 0.25 mm ID × 0.12 µm; Agilent Technologies). For separation of the D, L-isovaline enantiomers a 6890N series GC coupled to a 5973 MSD (both Agilent Technologies) and a CP-Chirasil-Dex CB GC Column (25 m × 0.25 mm ID × 0.25 µm; Agilent Technologies) were used.

Helium was used as the carrier gas and the column flow rate was set at 1.1 ml min^{-1} and injection (1 µl) was in split mode (10:1) at 220°C. The source and quadrupole temperatures were maintained at 230°C and 150°C, respectively, and the MSD transfer line was heated to 180°C. Standard autotunes with perfluorotributylamine (PFTBA) and air/water checks were made daily. The oven program was set at an initial temperature of 90°C and held for 2 minutes, then increased

by 5°C min^{-1} to 200°C and held for 6 minutes. GC-MS methods were the same for both instruments used. Total ion current chromatograms were acquired and analyzed with the Agilent Technologies MSD ChemStation (6890-5973) or MassHunter (7890-5975) software packages. Amino acids present in the Winchcombe meteorite samples were identified by comparison of the retention time and mass fragmentation pattern with a known amino acid standard reference mixture, and quantification was made by chromatographic data collected in the selected ion monitoring (SIM) mode. Identification was added by retention time locking of the GC method and creation of a custom library from standards which include retention time and retention indices for the amino acids.

21.4 *Results*

The pristine nature of the Winchcombe meteorite is reflected by its amino acid content (Table S23). In the hot water extracts of the Winchcombe meteorite, trifluoroacetyl (TFA)-derivatives of two up to six carbons ($C_2 – C_6$) amino acids were identified and quantified. The total (free + bound peptide-like) amino acid abundance in the 6M HCl hydrolyzed hot water extract of the Winchcombe meteorite was 1132 ± 49 ppb (Table S23), which is lower than most primitive CM chondrites such as Murchison (14,600 ppb) (*130*). The presence of terrestrially rare amino acids (e.g. α-aminoisobutyric acid (α-AIB), α-, β-, and γ-amino-n-butyric acids (ABA), isovaline), and the elevated abundance of some of these compounds, such as α-AIB (467 ± 17 ppb) and isovaline (391 ± 17 ppb) – the two most abundant amino acids in the Winchcombe meteorite – strongly indicate that these amino acids are extraterrestrial in origin. Terrestrial biology uses only the L-enantiomers of chiral amino acids except in rare scenarios. Therefore, the indigenous nature of the detected amino acids in the Winchcombe meteorite is unequivocally established by the racemic mixtures of the D- and L-enantiomers of both non-protein amino acids (e.g. $D/L_{isovaline}$ = 1.06 ± 0.15) and common protein amino acids (e.g. $D/L_{alanine}$ = 1.13 ± 0.16).

Protein amino acids that are derived from terrestrial contamination, such as serine and threonine, were found predominantly as the L-enantiomers (up to enantiopure) in the soil collected from Site 1 (Table S4), which are absent in the Winchcombe meteorite. Biologically derived amino acids often increase in abundance after acid hydrolysis as they are released from their bound form, as was observed in the Site 1 soil. This contrasts with what was observed for the Winchcombe meteorite, providing further compelling evidence against any significant contribution of the amino acids from a biological origin.

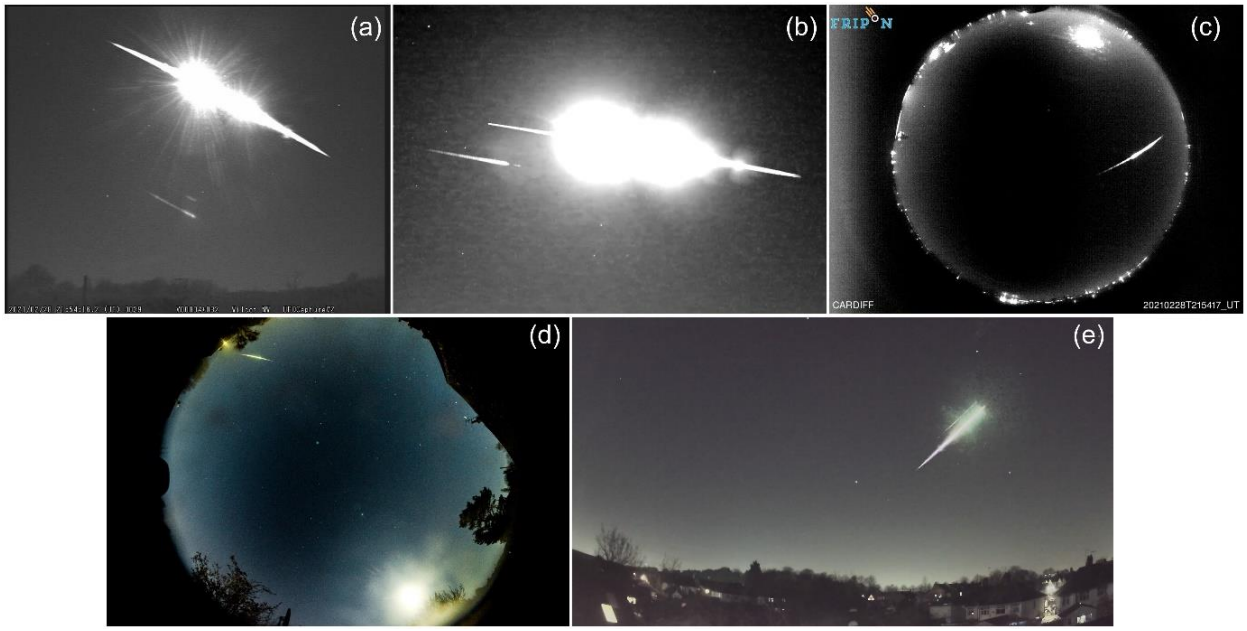

Figure S1. The Winchcombe fireball, as observed by the UKFAll camera networks. (a) UKMON camera in Wilcot; (b) GMN camera in Hullavington; (c) SCAMP/FRIPON camera in Cardiff; (d) UKFN camera in Welwyn; (e) AllSky7 camera in Nuneaton. A reflection in the optics that is parallel to the fireball is also visible in insets (a), (b) and (e).

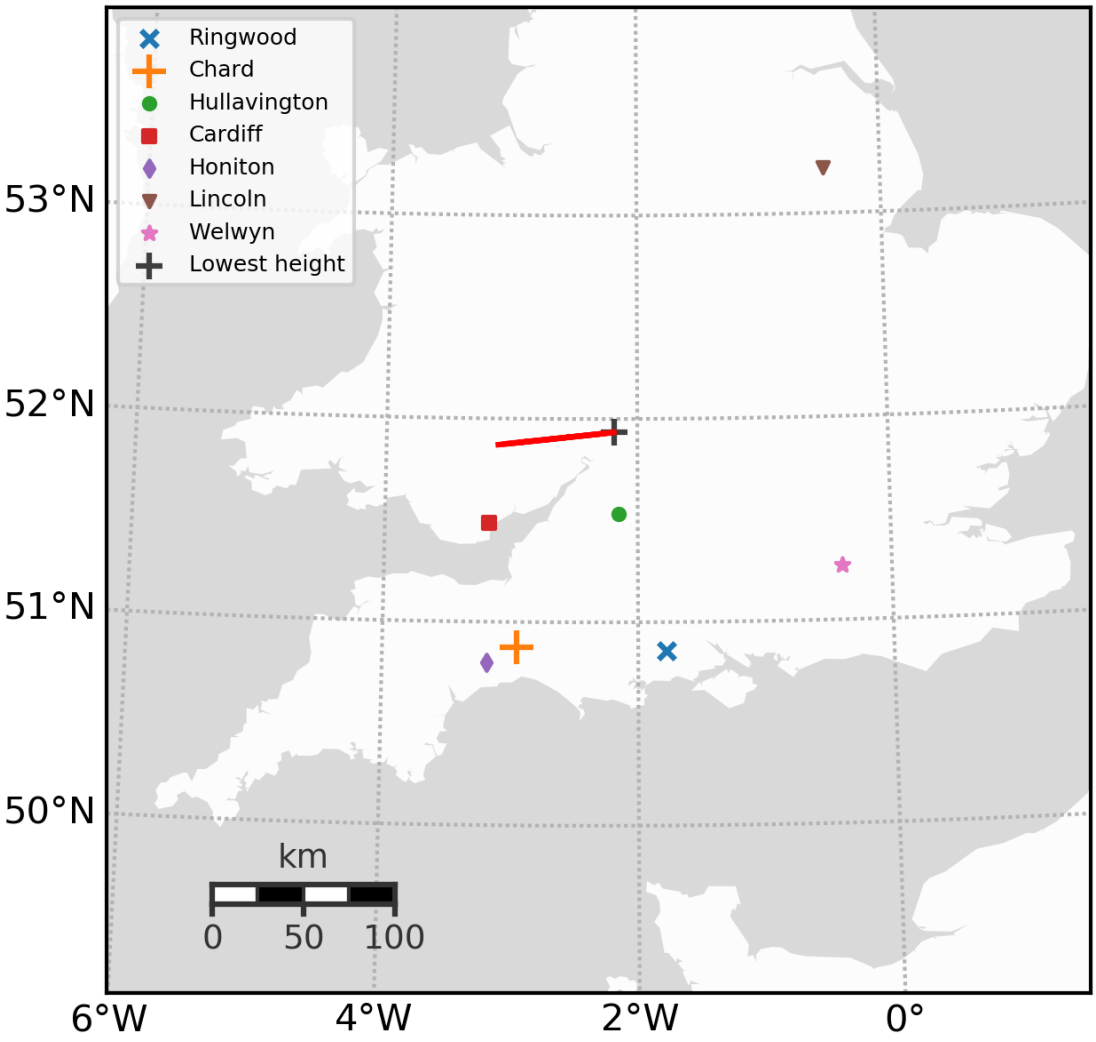

Figure S2. The Winchcombe fireball trajectory (red line) and locations of cameras used for astrometric measurements.

5

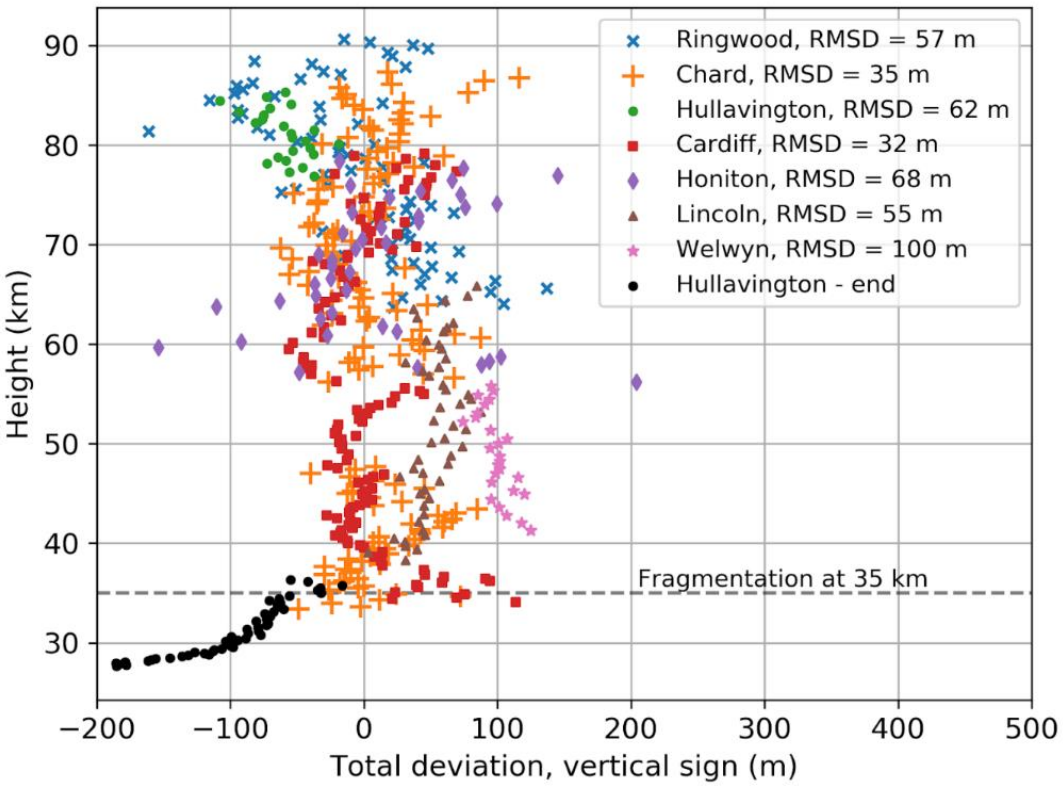

Figure S3. Trajectory fit residuals versus height. RMSD stands for root-mean-square deviation. The measurements from Hullavington were only done at the beginning and the end, as the fireball was too bright in the middle of the flight for accurate astrometric picks.

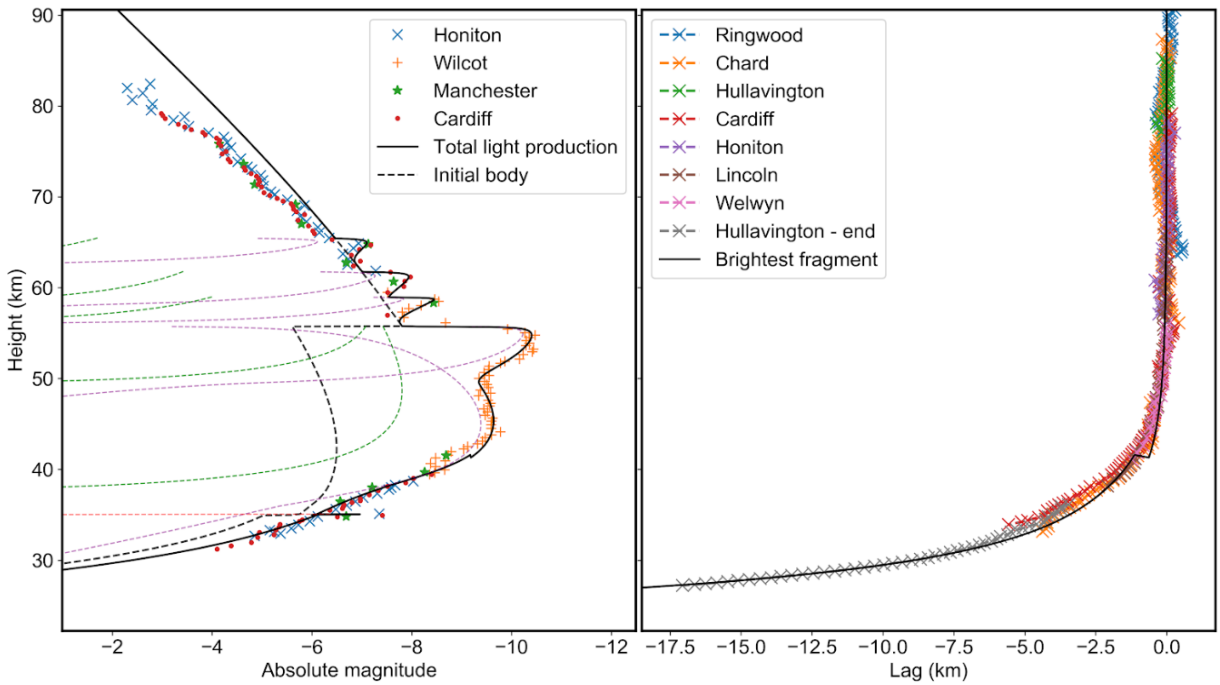

Figure S4. Fit of the ablation model (black line) to the observed light curve (left) and the deceleration (right) for the Winchcombe fireball. Contributions to the total light production of individual fragments is given in dashed lines; black for the magnitude of the main body, green for eroding fragments, purple for grains released by erosion, and orange for dust released directly from the main body.

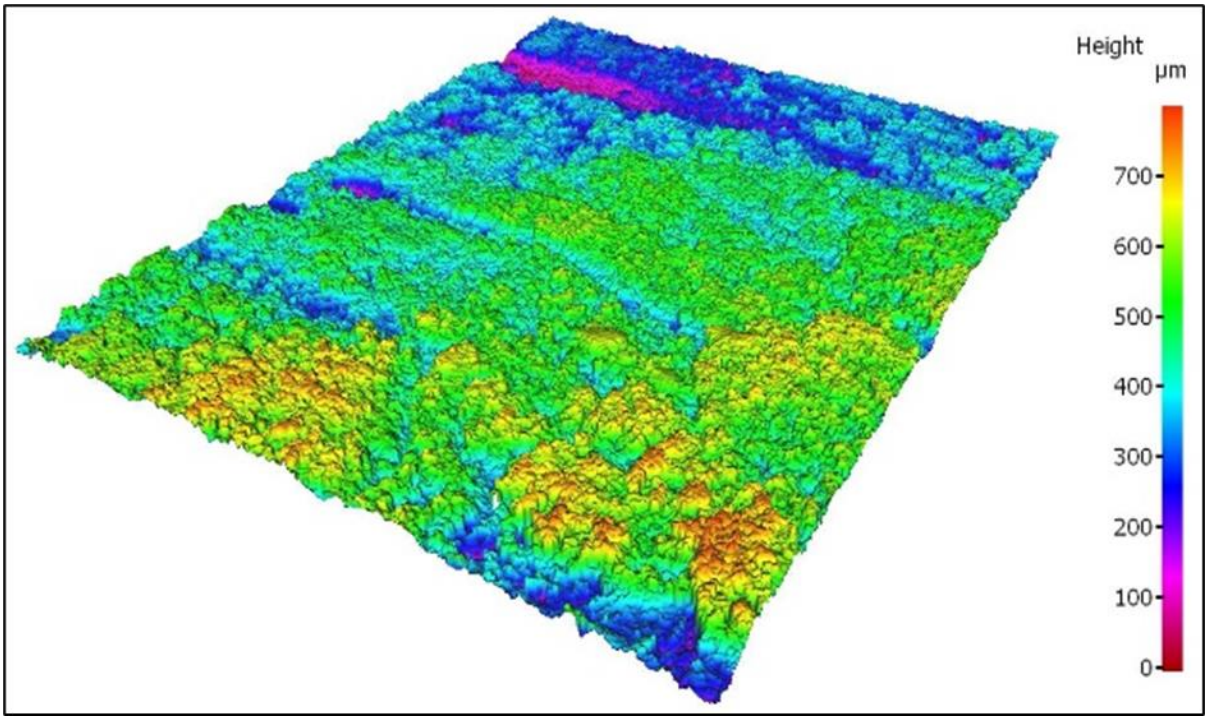

Figure S5. A 1 cm^2 surface profile of the Winchcombe meteorite sample used in the reflectance study, measured using an Alicona 3D® instrument. Lateral resolution = 10 µm; vertical resolution = 1 µm.

5

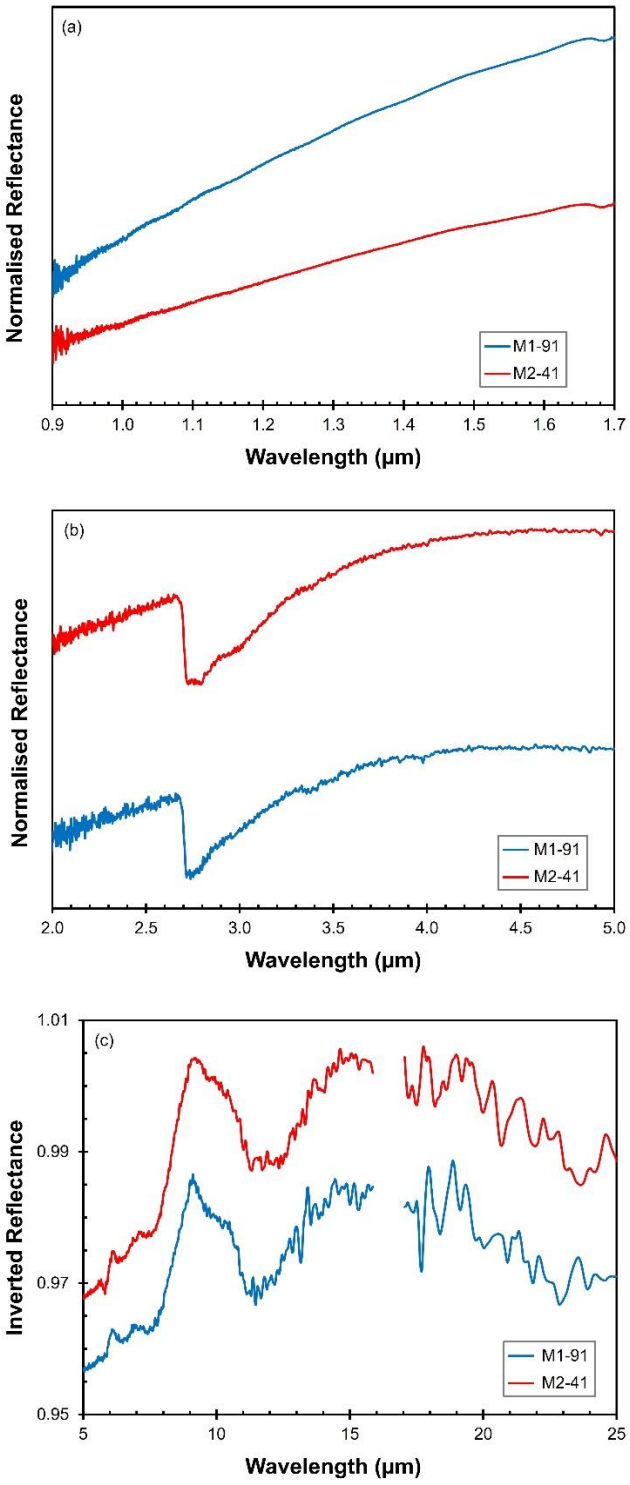

Figure S6. VNIR ((a) and (b)) and MIR (c) reflectance spectra for powdered Winchcombe meteorite samples BM.2022,M1-91 and BM.2022,M2-41. The slope in (a) is consistent with a fine particulate sample with a high phyllosilicate abundance. Features in (b) are related the water content and phyllosilicate composition, and features in (c) suggest small variations in the olivine content and degree of aqueous alteration recorded by the samples.

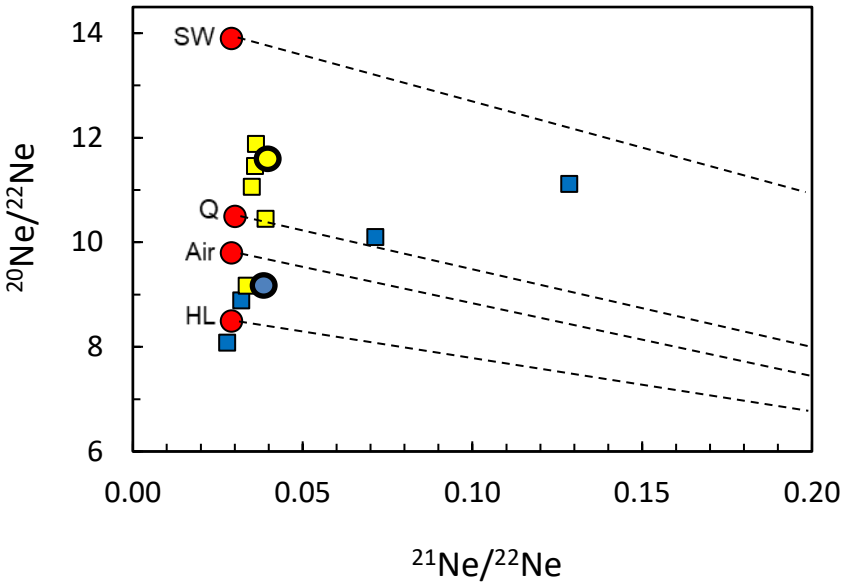

Figure S7. Neon isotope composition of gases released by step heating two samples of the Winchcombe meteorite (BM.2022,M2-36 and BM.2022,M4-7). The isotopic composition of the total gas from each sample is shown as circles. Black dashed lines represent mixing between the main trapped components (red circles: solar wind (SW; (*131*)), Air (*132*), Q (*53*), and HL (*54*)) with cosmogenic Ne derived from Galactic Cosmic Rays (*133*).

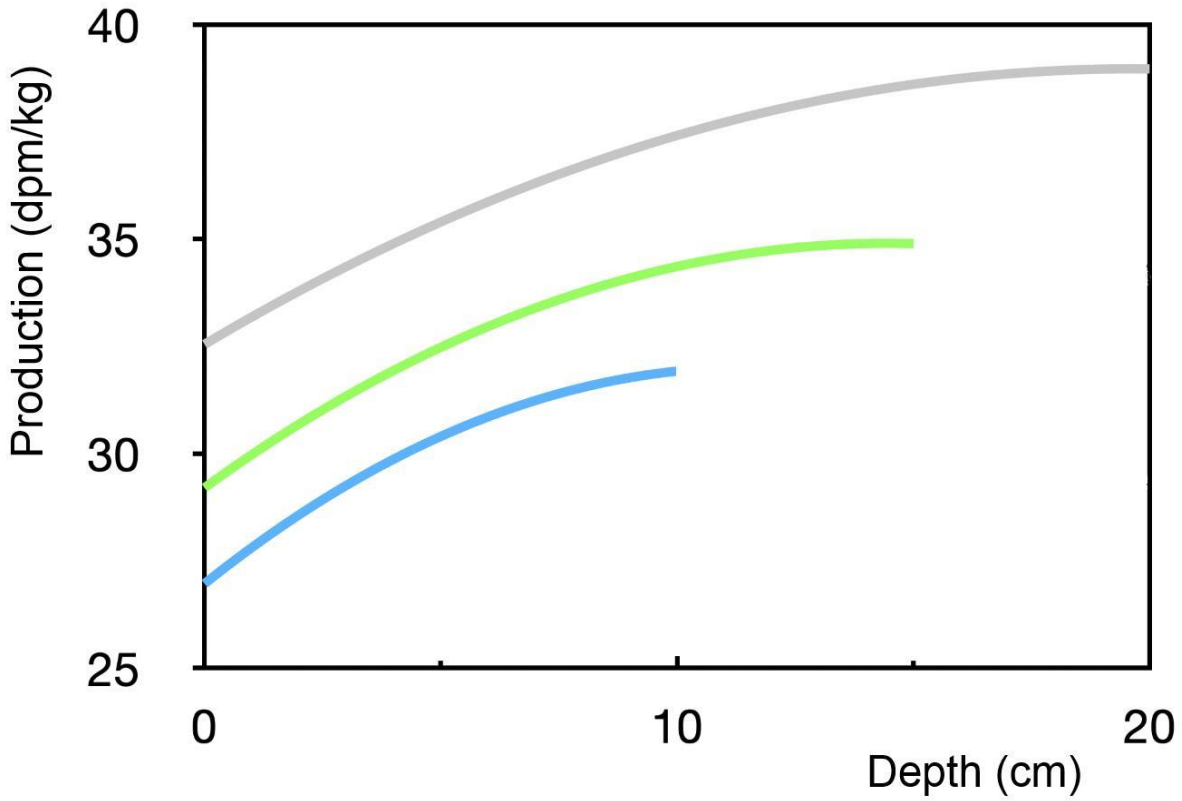

Figure S8. Saturated ^{26}Al production rates in the Winchcombe meteorite with radius of 10 and 20 cm, estimated from Monte Carlo simulations (adjusted for the meteorite chemical composition) (*55*).

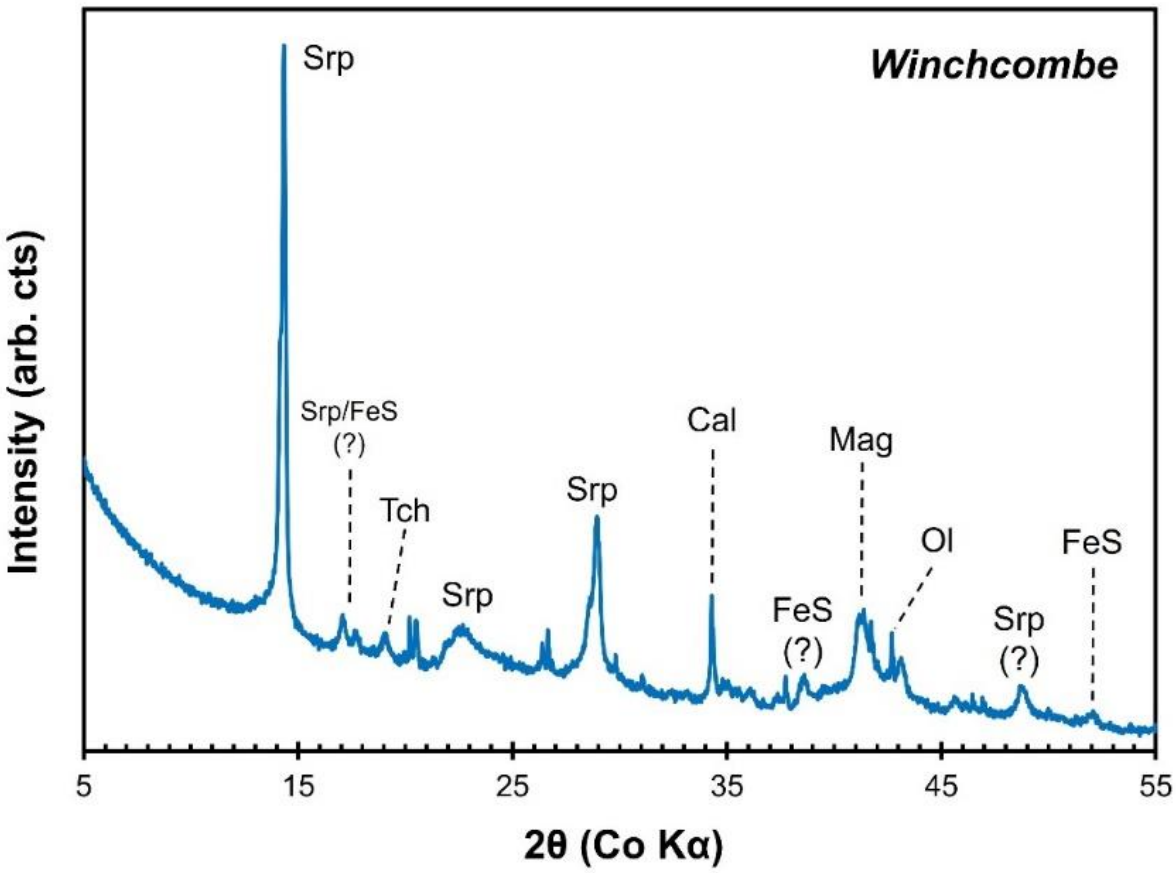

Figure S9. XRD pattern of Winchcombe meteorite sample BM.2022,M1-88 collected using a PANalytical X'Pert Pro scanning XRD. Minerals identified include phyllosilicates (serpentine (Srp)), tochilinite (Tch), calcite (Cal), Fe-sulfides (pyrrhotite (FeS), magnetite (Mag), and olivine (Ol).

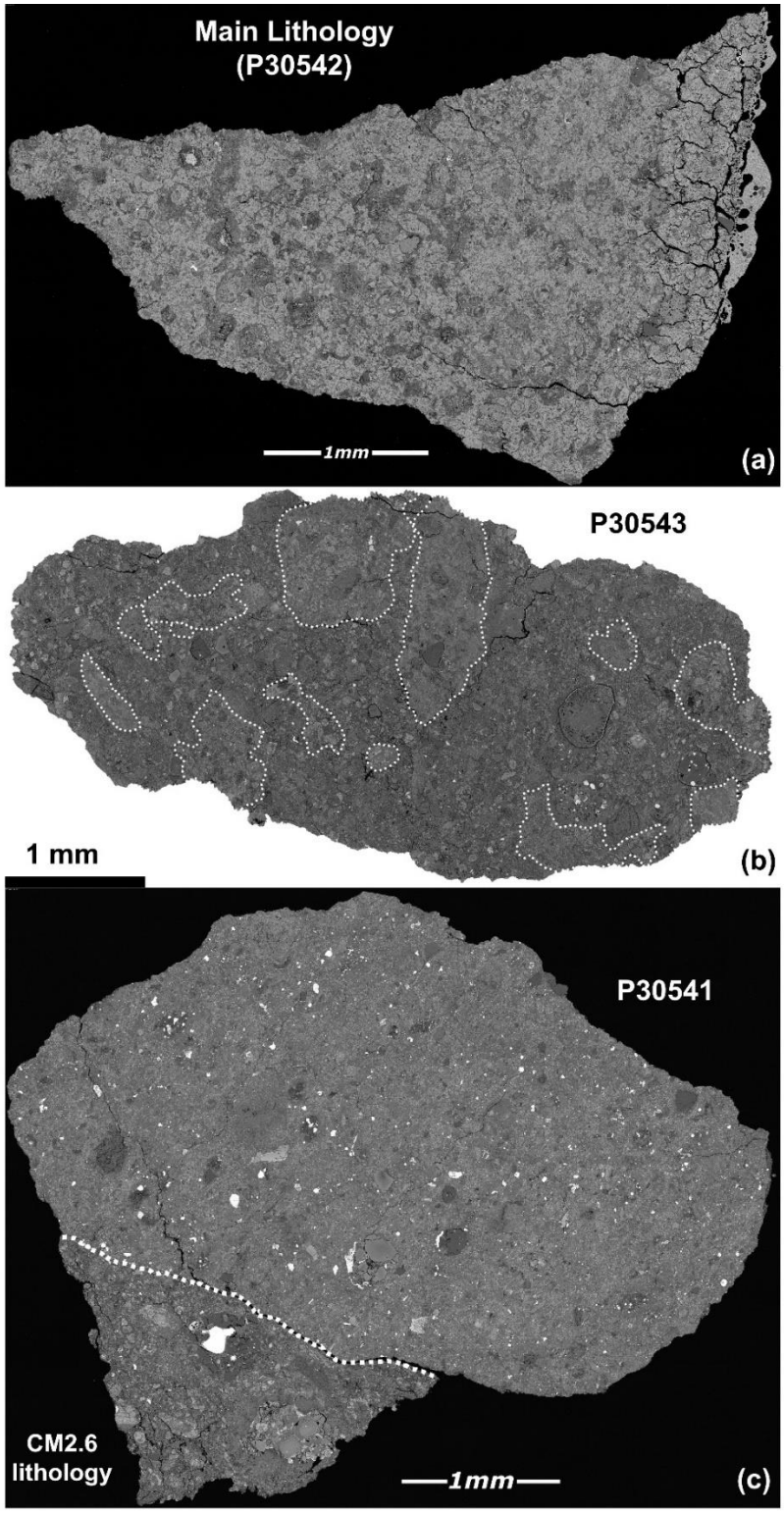

Figure S10. Example BSE overview images of Winchcombe meteorite samples. (a) P30542 only contains the main lithology identified in the Winchcombe meteorite, whereas (b) P30543 and (c) P30541 are comprised of multiple lithologies (highlighted by dashed white lines).

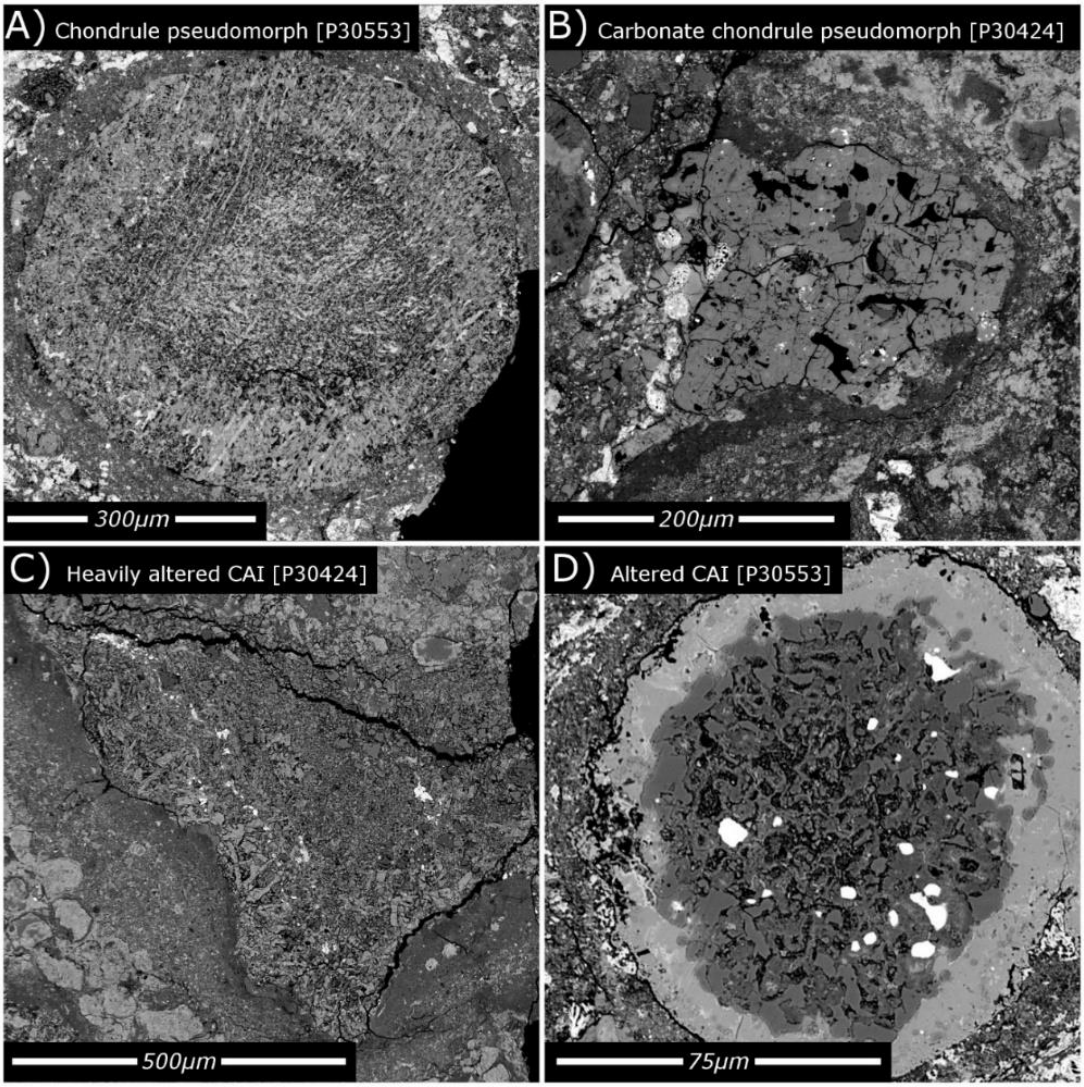

Figure S11. BSE images showing chondrule pseudomorphs with interiors replaced by (a) phyllosilicates and (b) carbonates, and examples of (c, d) altered CAIs in the main lithology of the Winchcombe meteorite.

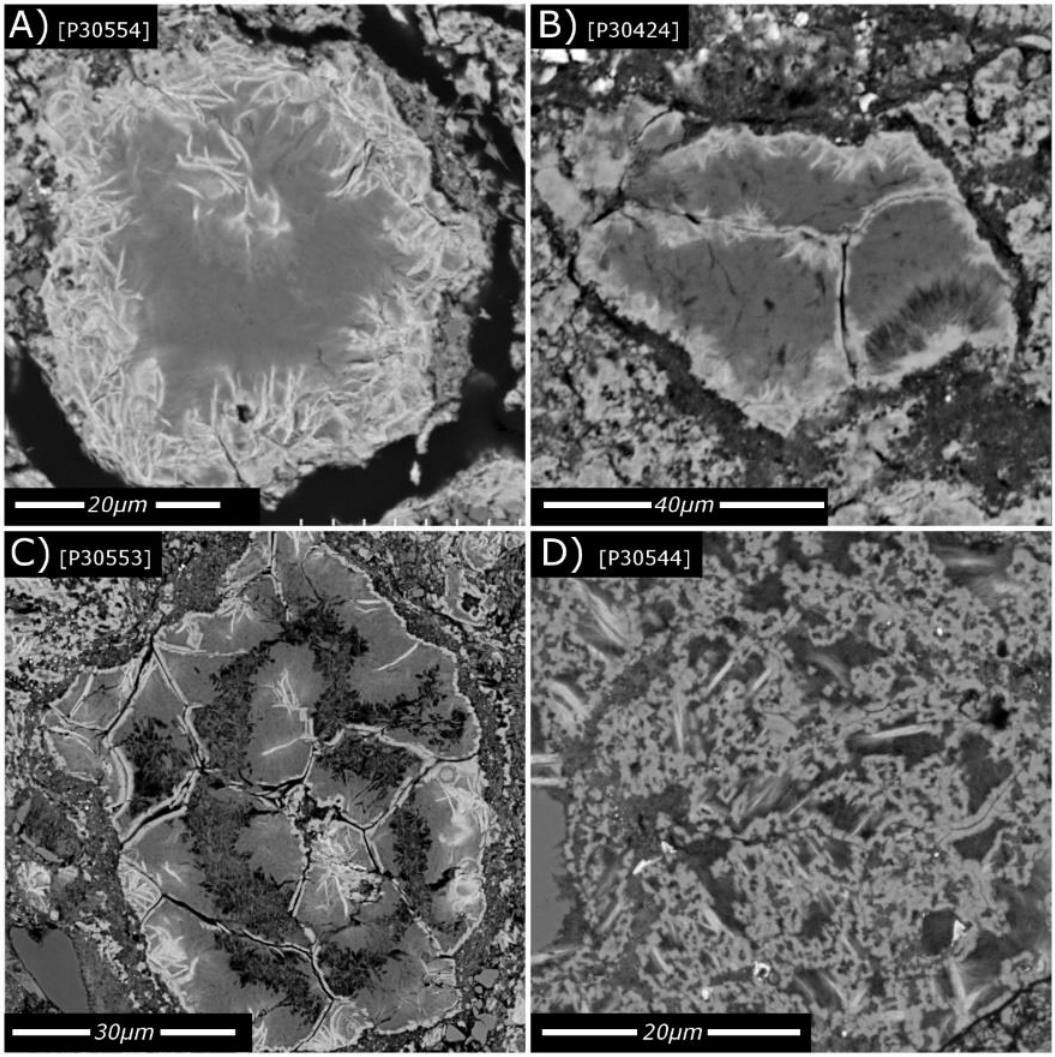

Figure S12. BSE images showing examples of coarse phyllosilicate clumps in the main lithology of the Winchcombe meteorite.

5

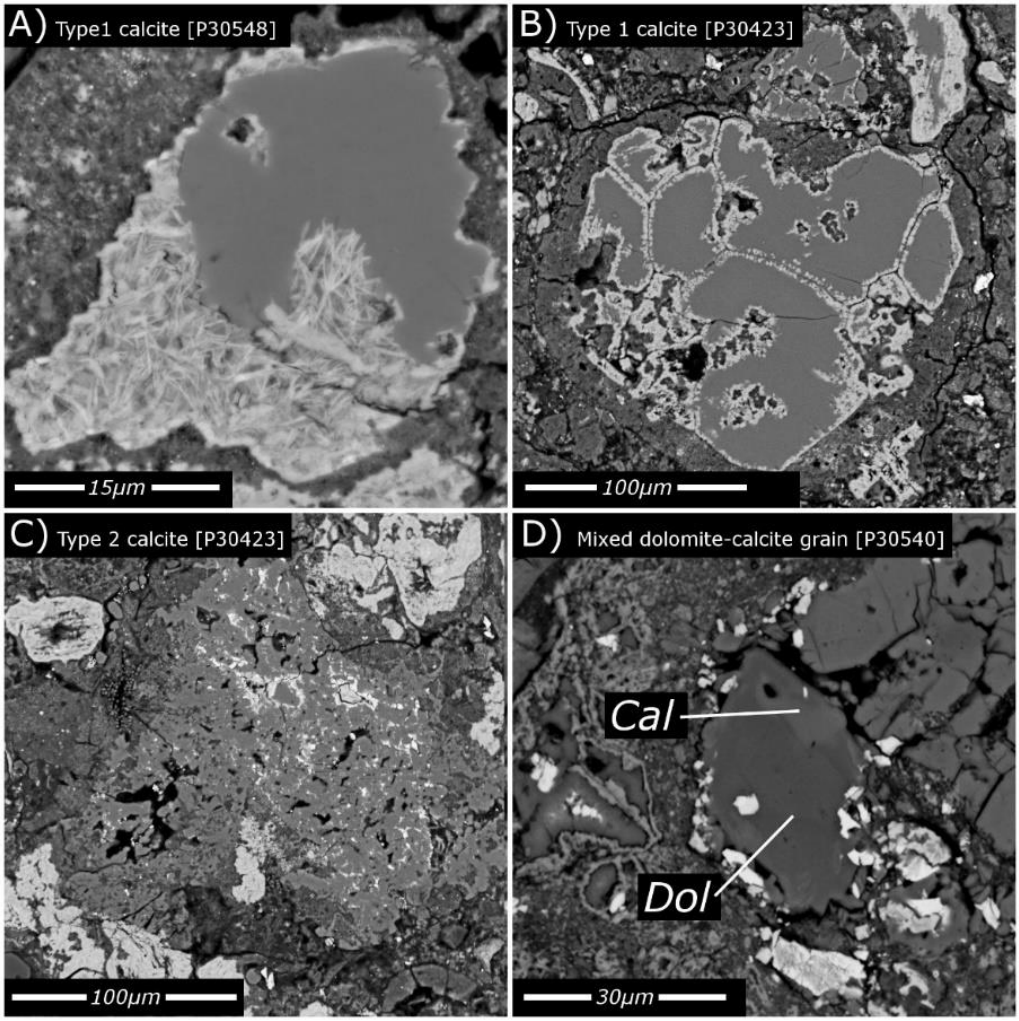

Figure S13. BSE images showing examples of (a, b) type 1 and (c) type 2 calcite, and (d) mixed calcite-dolomite in the minor lithologies of the Winchcombe meteorite.

5

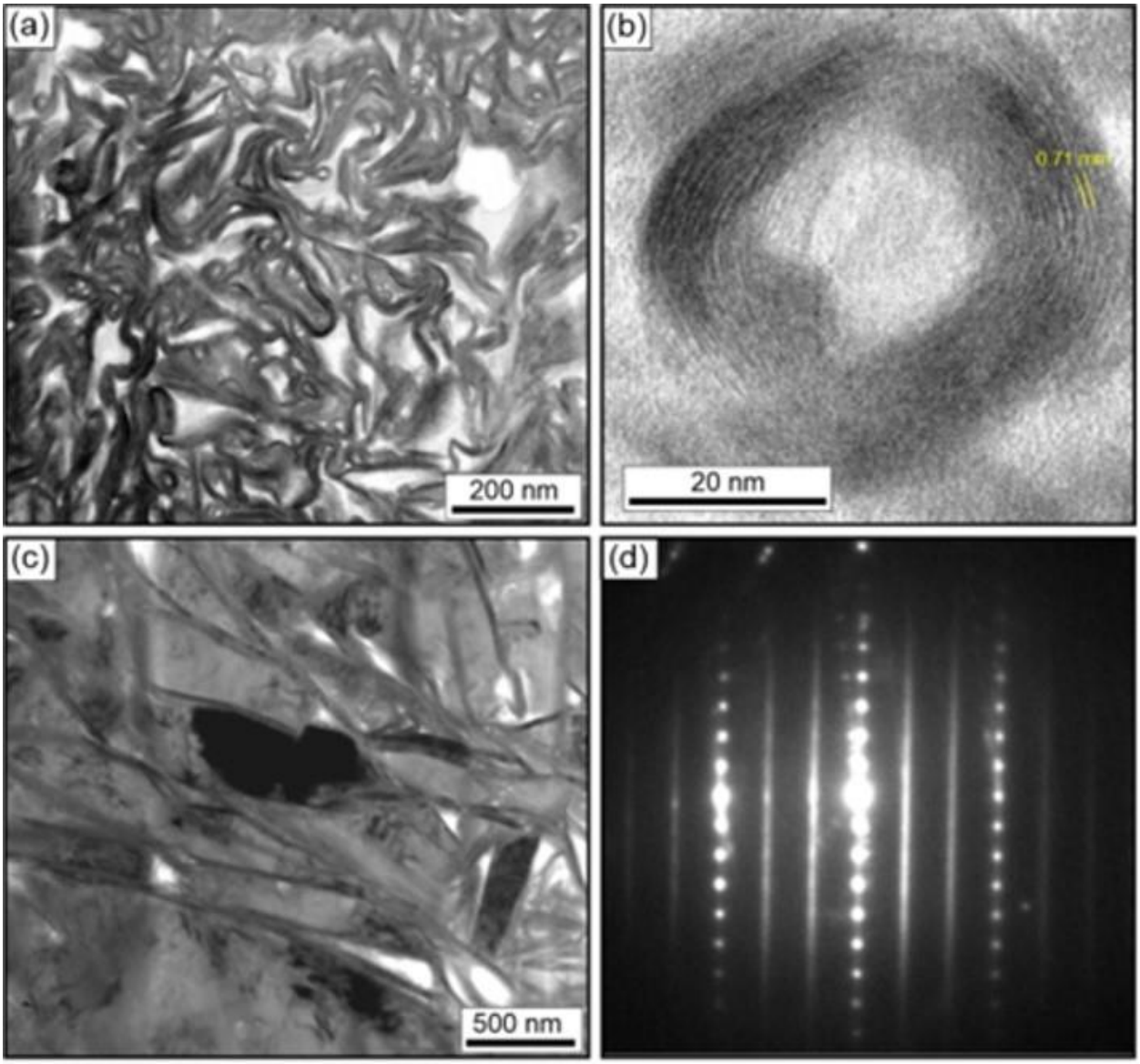

Figure S14. (a) Bright-field TEM image of an area of matrix that contains abundant curved and tubular chrysotile crystals. (b) High-resolution image of a chrysotile tube with a ~0.71 nm lattice spacing consistent with 1:1 layered T-O phyllosilicates such as serpentine and chrysotile. (c) Bright-field image of platy cronstedtite crystals. (d) SAED pattern of the crystal in the middle of (c). The spots have a d-spacing of 0.72 nm, and the streaking of the k≠3 rows is indicative of stacking disorder in the cronstedtite lattice.

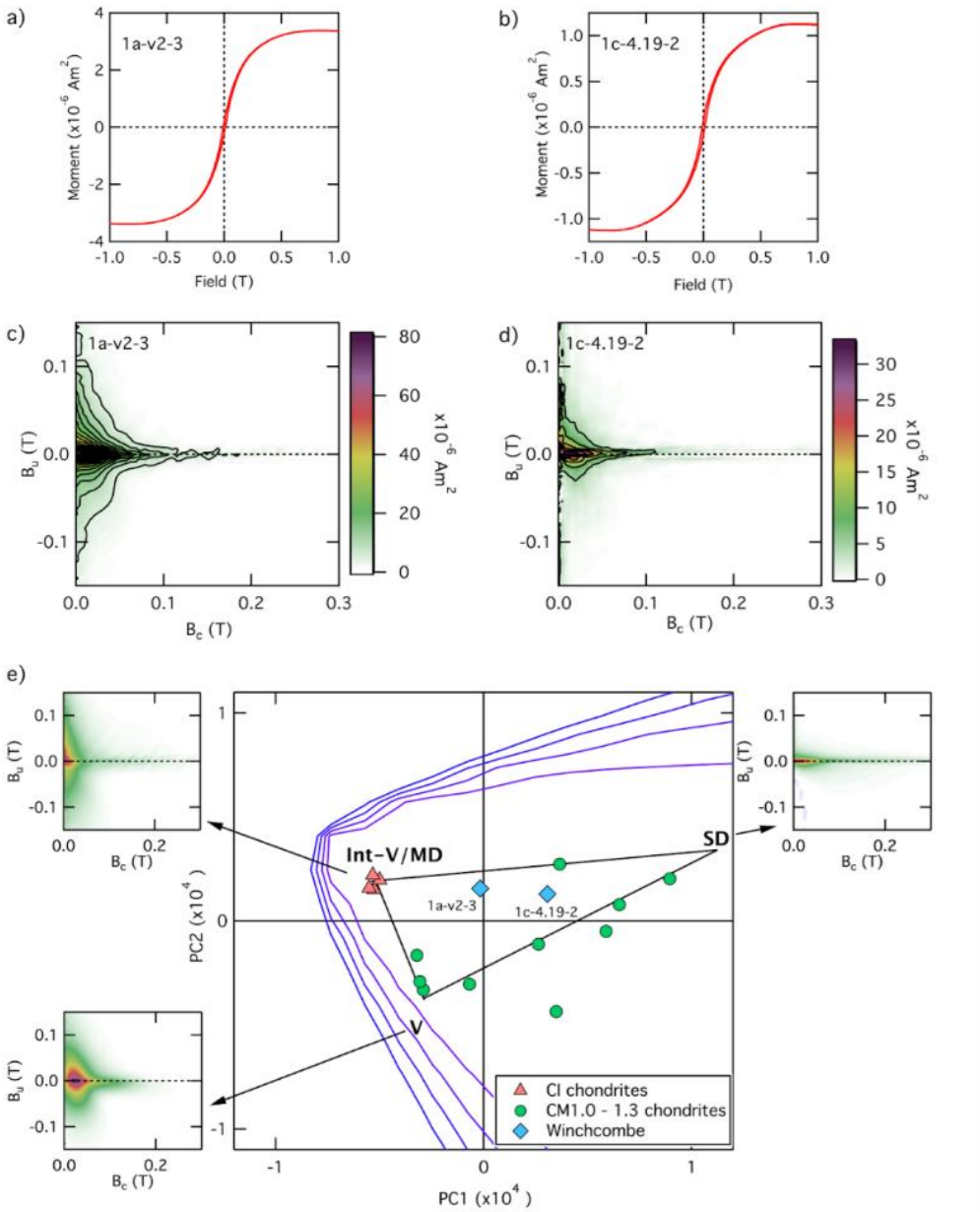

Figure S15. (a) Hysteresis loop of chip BM.2022,M1-95 (1a-v2-3 on figures); (b) Hysteresis loop of chip BM.2022,M3-32 (1c-4.19-2 on figures); (c) FORC diagram of chip BM.2022,M1-95; (d) FORC diagram of chip BM.2022,M3-32; and (e) Score plot displaying the proportions of PC1 and PC2 present in CI1.0 chondrites, CM1.0-1.3 chondrites, and Winchcombe meteorite chips BM.2022,M1-95 and BM.2022,M3-32. The Winchcombe meteorite data plot within the range of FORC diagrams defined by CI1.0 and CM1.0-1.3 chondrites, overlapping with the CM chondrites, but displaying a higher proportion of interacting vortex/multi-domain (Int-V/MD) particles. V = Vortex state, SD = Single Domain. Contours of feasibility metrics have been superimposed onto the score plot to help identify regions where physically realistic endmembers could be situated, with contours between 0.90 and 0.98 shown with intervals of 0.02. CI and CM chondrite data adapted from (*96*).

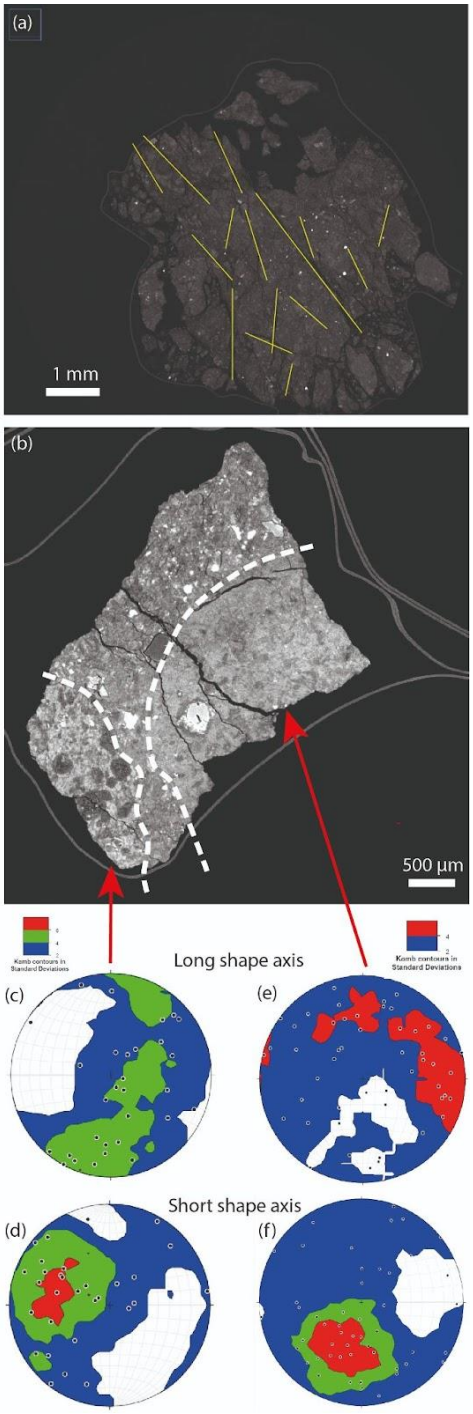

Figure S16. Example XCT data from Winchcombe meteorite samples BM.2022,M1-84 and BM.2022,M2-34. (a) and (b) – Example CT slice from two samples, with (a) showing aligned fractures and (b) showing three distinct lithologies distinguishable by their texture and contrast variations. (c) and (e) – lower hemisphere projection of the long shape axis of chondrules showing a weak-moderate girdle fabric. (d) and (f) – lower hemisphere projection of the short shape axis of chondrules showing a weak-moderate lineation fabric. There preferred alignments in the long and short shape axis of chondrules are consistent with a foliation fabric caused by compaction.

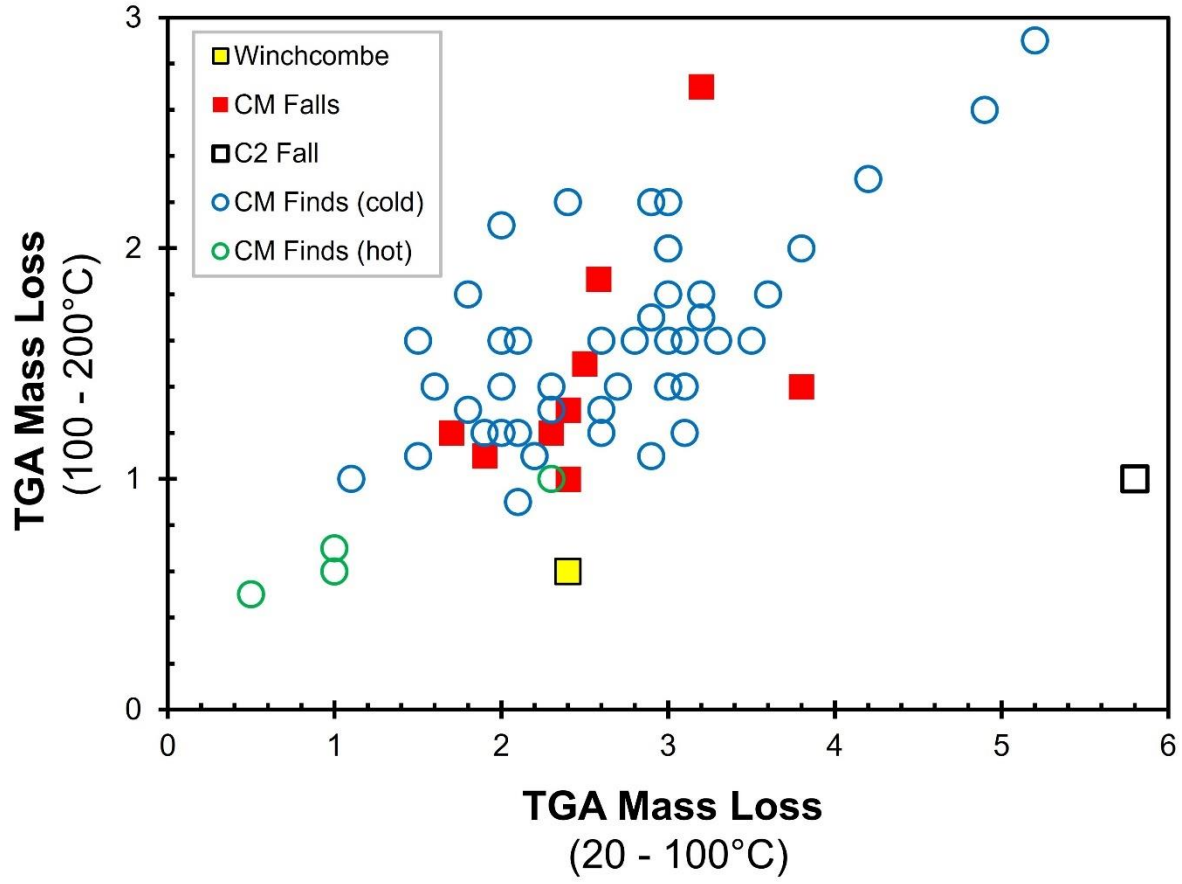

Figure S17. TGA mass loss between 20 – 100°C and 100 – 200°C for a sample of the Winchcombe meteorite analyzed on the 5th March 2021 compared to other CM/C2 chondrites measured in our laboratory. Data are from (*51*, *106*, *134*, *135*).

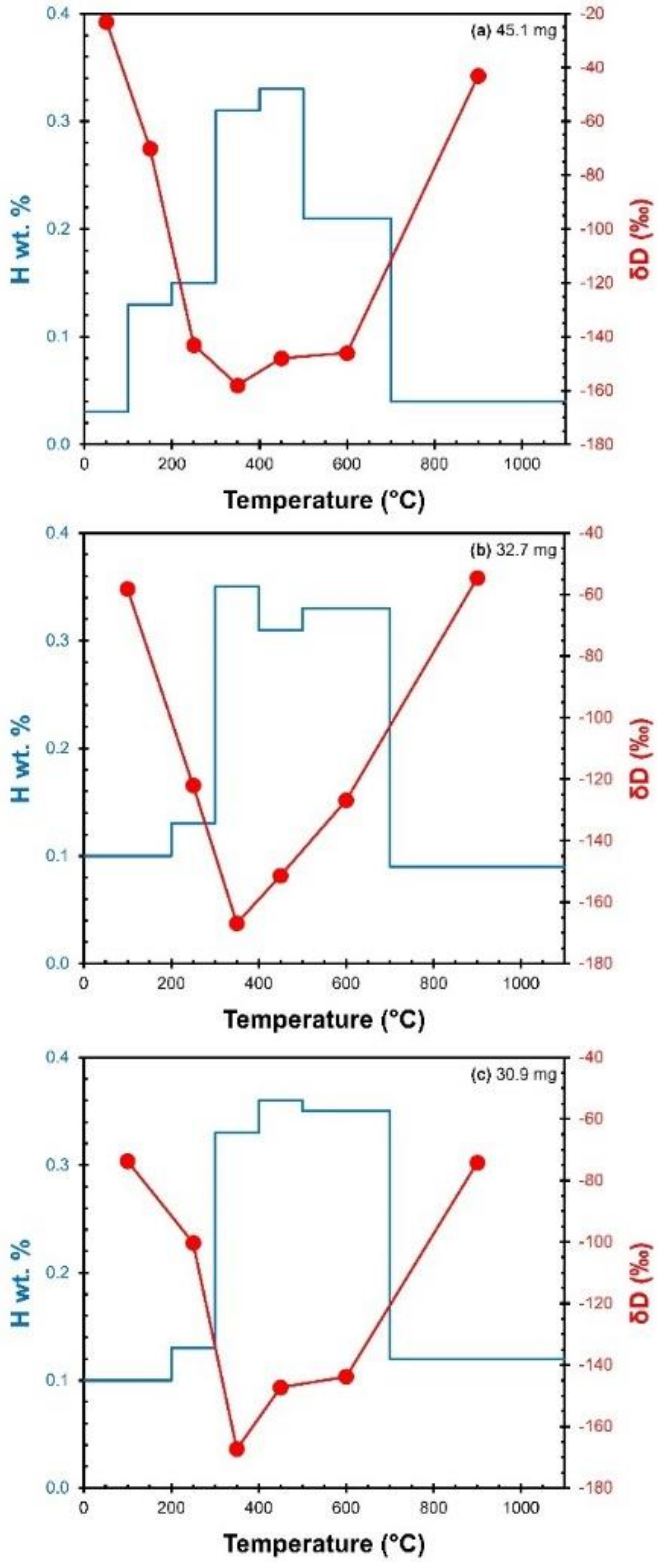

Figure S18. Abundance and isotopic composition of hydrogen released during stepped pyrolysis of the Winchcombe meteorite samples (a) BM.2022,M2-39-a, (b) BM.2022,M2-39-b, and (c) BM.2022,M2-39-c.

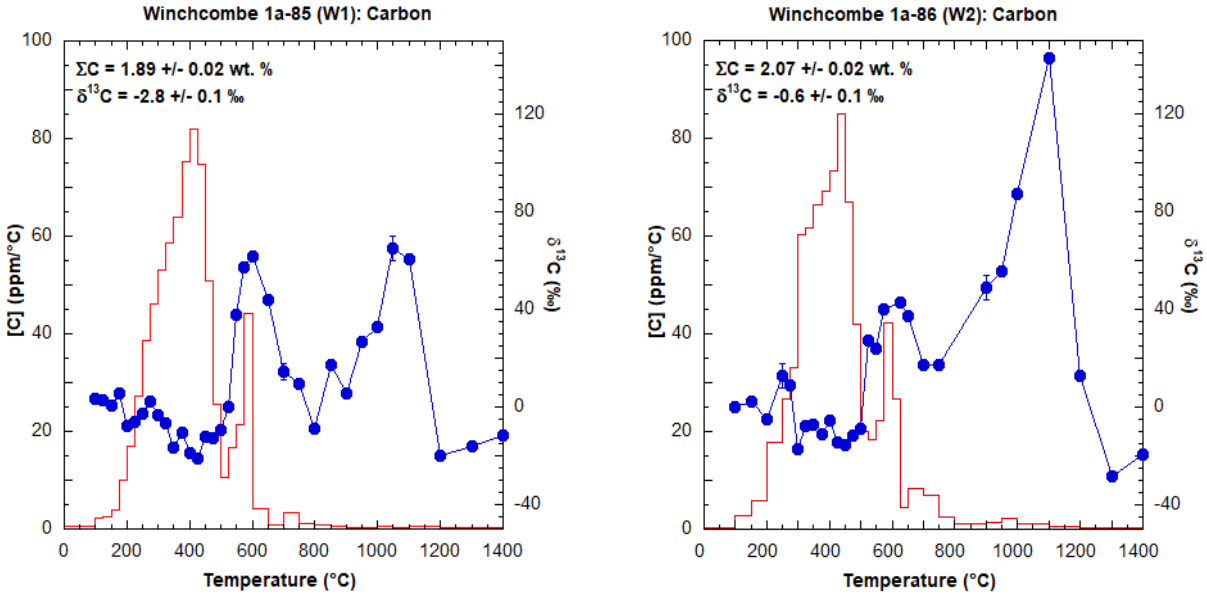

Figure S19. Carbon data from stepped combustion of Winchcombe chips BM.2022,M1-85 (5.0502 mg; 1a-85 (W1) on figure) and BM.2022,M1-86 (5.0981 mg; 1a-86 (W2) on figure). Abundance (in ppm °C^{-1}; scaled on the left axis) is the red histogram. Isotopic composition (in %; scaled on the right axis) is the blue line. Errors are less than the size of the symbol unless shown otherwise.

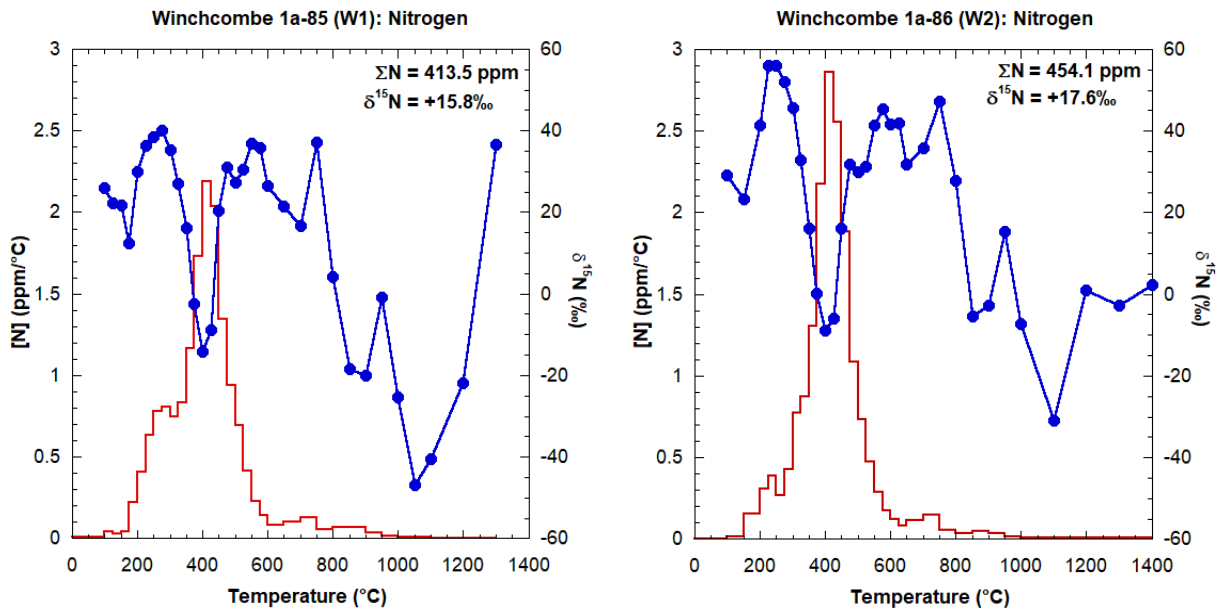

Figure 20. Nitrogen data from stepped combustion of Winchcombe chips BM.2022,M1-85 (5.0502 mg; 1a-85 (W1) on figure) and BM.2022,M1-86 (5.0981 mg; 1a-86 (W2) on figure). Abundance (in ppm $°C^{-1}$; scaled on the left axis) is the red histogram. Isotopic composition (in %; scaled on the right axis) is the blue line. Errors are less than the size of the symbol unless shown otherwise.

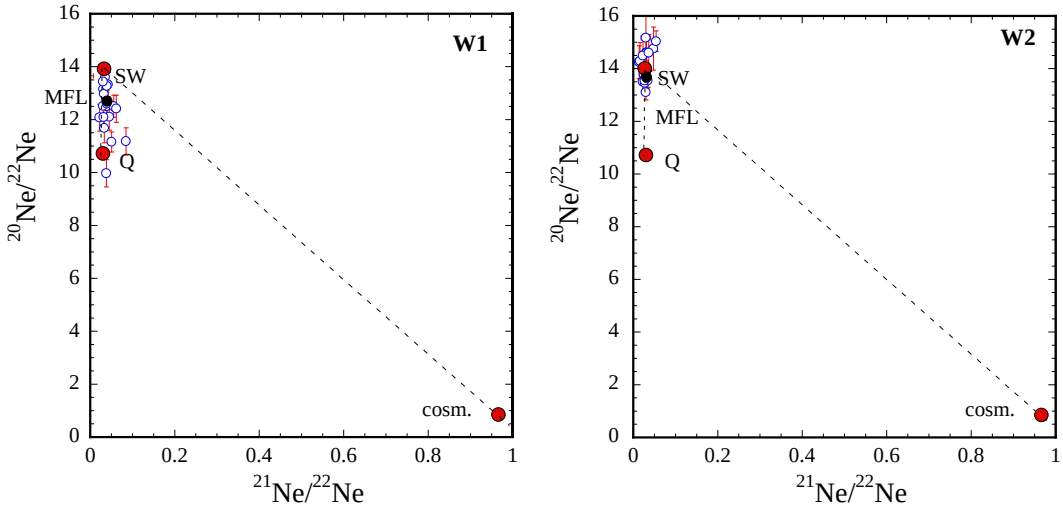

Figure S21. Isotopic composition of Ne in the temperature steps of Winchcombe meteorite samples BM.2022,M1-85 (W1) and BM.2022,M1-86 (W2). SW – solar wind composition (*136*); Q – planetary composition (*137*); MFL – mass fractionation line; cosm. – cosmogenic Ne. The total (summed) Ne isotopic composition is shown in black.

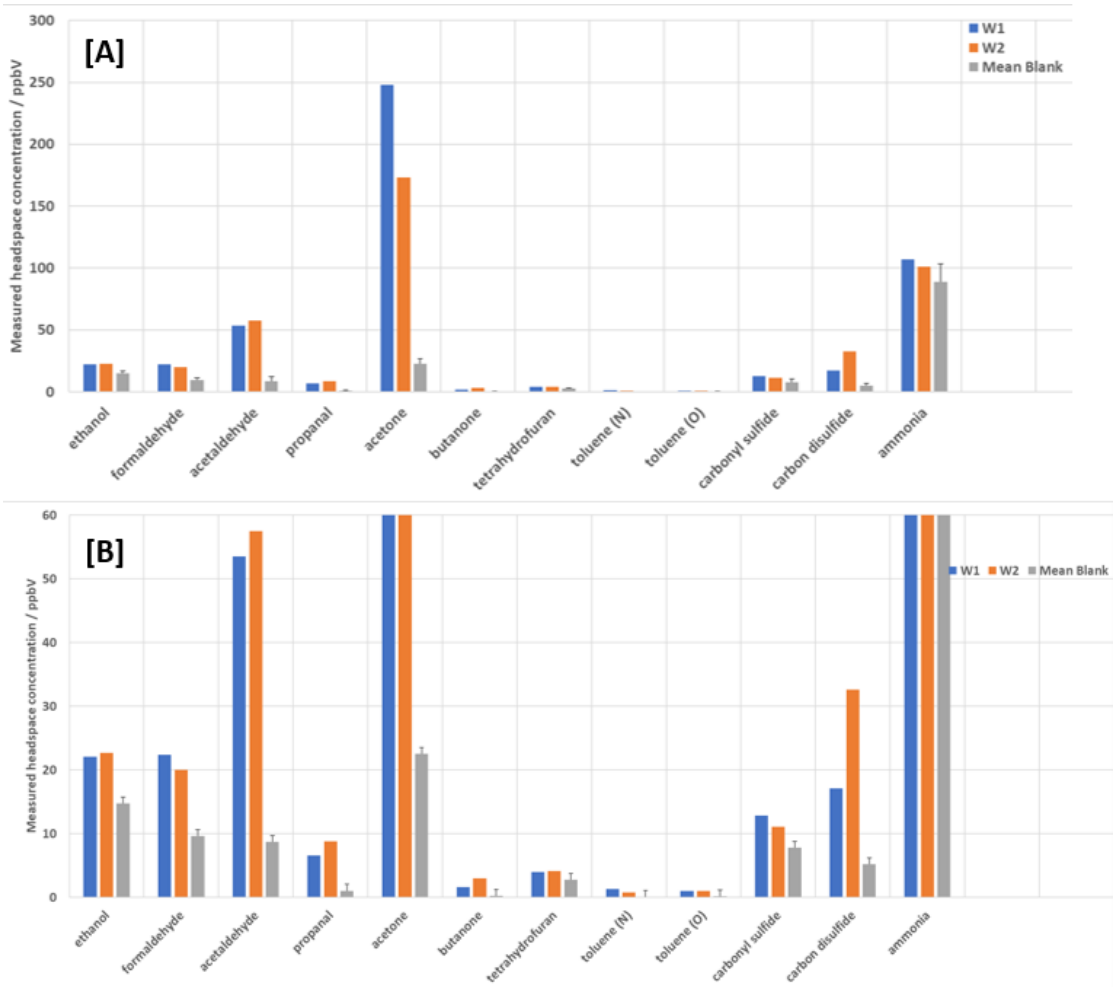

Figure S22. Species identified in a preliminary SIFT-MS analysis of headspace gases from Winchcombe meteorite samples BM.2022,M1-85 (W1, blue) and BM.2022,M1-86 (W2, orange). The blank from an empty vial is shown in grey. [A] Concentration in ppbV; [B] the same data at higher scale to show concentrations of minor species relative to the blank.

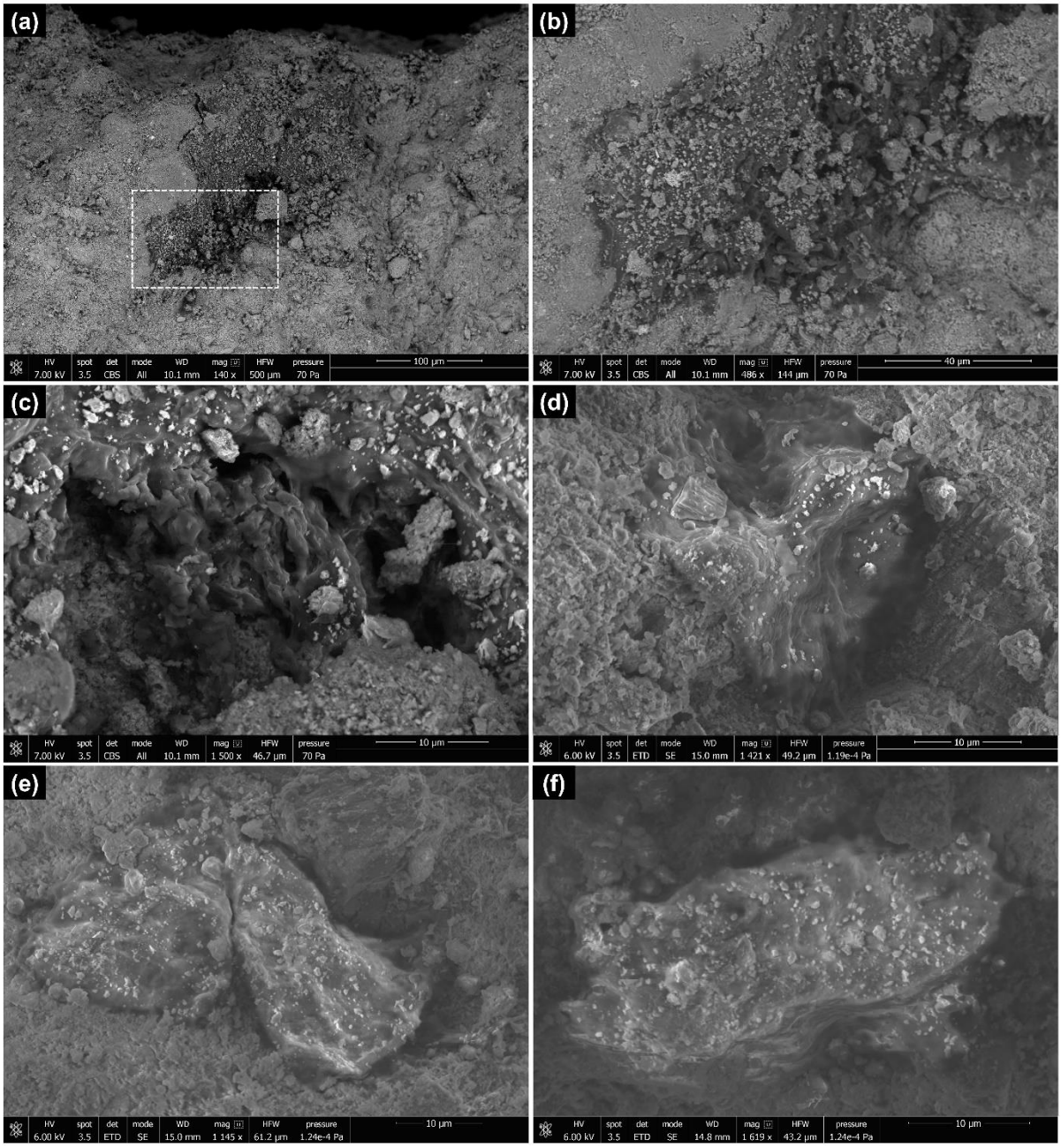

Figure S23. (a) BSE overview image of an ~100 × 300 µm carbon-rich area in a fragment of the Winchcombe meteorite. (b) BSE image of the area marked by a dashed white box in (a) showing that the carbon-rich area is intrinsic to the meteorite and not terrestrial contamination. (c) BSE image showing the texture of the carbon-rich material shown in (b). (d), (e), and (f) SE images of carbonaceous materials with "globule-like" morphologies found in uncoated and unprepared fragments of the Winchcombe meteorite.

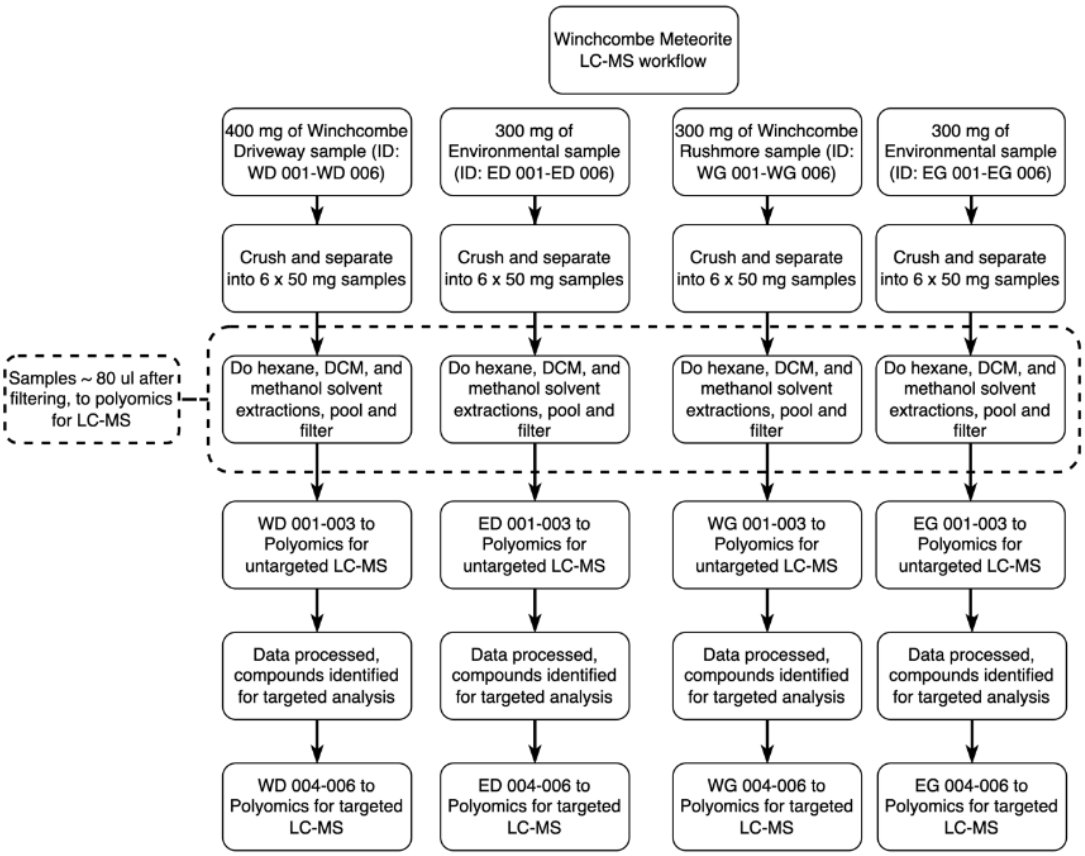

Figure S24. The analytical workflow for LC-MS characterization of the Winchcombe meteorite samples BM.2022,M2-23 and BM.2022,M9-4.

5

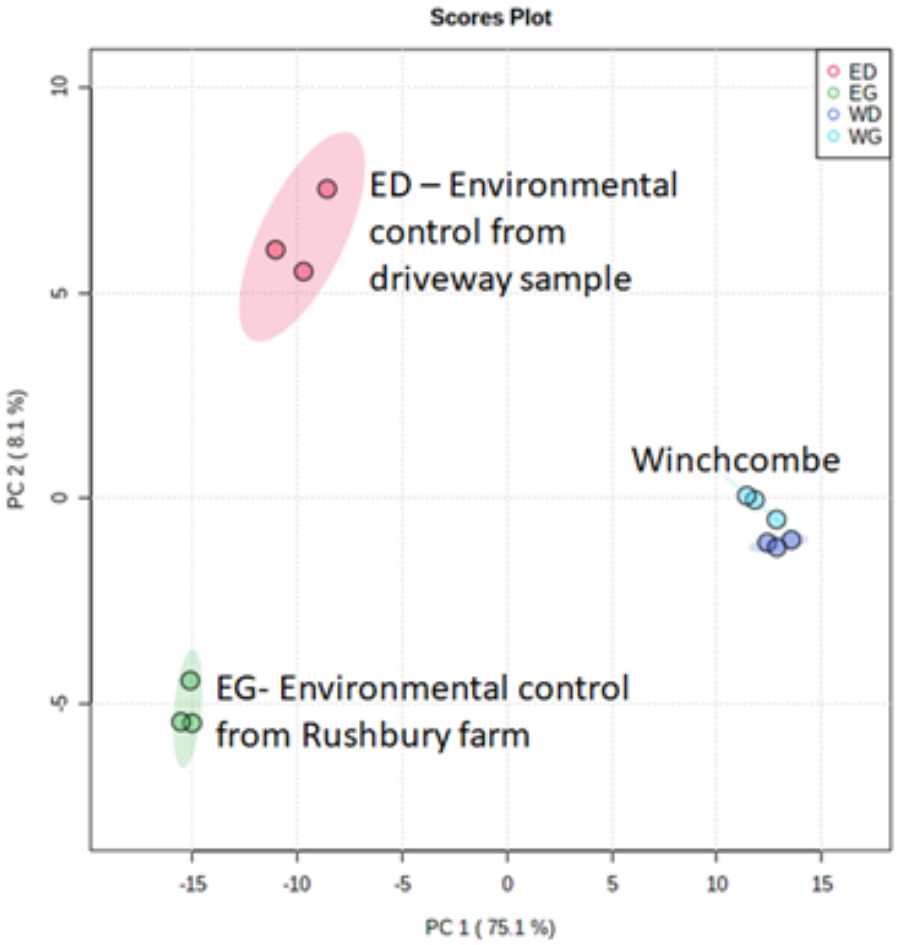

Figure S25. Two dimensional PCA of untargeted metabolomics data from the Winchcombe meteorite samples BM.2022,M2-23 and BM.2022,M9-4, and their corresponding environmental samples. The first principal component accounts for 75.1 % of the variance in the samples, indicating that the organic content in the solvent extracts of the Winchcombe meteorite was similar, but somewhat distinct from their environmental controls.

Table S1. Coordinates of UKFAll cameras that observed the Winchcombe fireball. Astrometry/Photometry indicates whether the data from the camera was used for astrometric picks (A) or for photometry (P).

Location	Network	Latitude (°)	Longitude (°)	Altitude (m, mean sea level)	Astrometry / Photometry
Cambridge	UKFN	52.164447	0.038883	8	-
Cardiff	SCAMP	51.486110	-3.177870	33	A + P
Chard	UKMON	50.877448	-2.949729	100	A
Chelmsford	NEMETODE	51.745000	0.493500	45	-
Clanfield	UKMON	50.938801	-1.019700	158	-
Honiton	SCAMP	50.801832	-3.184410	119	A + P
Hullavington	GMN	51.535053	-2.148658	103	A
Lincoln	UKFN	53.222048	-0.463622	16	A
Loughborough	NEMETODE	52.750500	-1.213000	73	-
Manchester	SCAMP	53.474365	-2.233606	69	P
Nuneaton	AllSky7	52.526389	-1.454722	80	-
Ringwood	GMN	50.857470	-1.778230	24	A
Tackley	GMN	51.883100	-1.306160	80	-
Welwyn	UKFN	51.268390	-0.394043	78	A
Wilcot	UKMON	51.351913	-1.801903	133	P
Antwerp (Bel)	AllSky7	51.213359	4.454574	16	-

Table S2. Radiant and pre-atmospheric orbit of the Winchcombe fireball.

Parameter		**Value**	1σ error	95% confidence interval	
Apparent radiant and entry velocity (relative to the ground)					
Azimuth (°)	A	263.342	± 0.046	263.235	263.399
Elevation (°)	a	41.919	± 0.029	41.852	41.961
Velocity (km/s)	v_0	13.547	± 0.008	13.531	13.560
Geocentric radiant (J2000.0) and velocity					
Right ascension (°)	α_G	56.638	± 0.017	56.604	56.671
Declination (°)	δ_G	+17.713	± 0.069	+17.555	+17.816
Velocity (km/s)	v_G	8.123	± 0.013	8.094	8.143
Heliocentric orbital elements (J2000.0)					
Semimajor axis (au)	a	2.5855	± 0.0077	2.5686	2.5980
Eccentricity	e	0.6183	± 0.0011	0.6158	0.6202
Perihelion distance (au)	q	0.986839	± 0.000012	0.986814	0.986861
Aphelion distance (au)	Q	4.184	± 0.015	4.150	4.209
Inclination (°)	i	0.460	± 0.014	0.440	0.491
Argument of perihelion (°)	ω	351.798	± 0.018	351.759	351.824
Ascending node (°)	Ω	160.1955	± 0.0014	160.1933	160.1985
Last perihelion		2021 Feb 22.446	± 0.015	2021 Feb 22.413	2021 Feb 22.469
Tisserand's parameter w.r.t. Jupiter	T_J	3.1207	± 0.0056	3.1117	3.1331

Table S3. Physical properties and atmospheric trajectory of the Winchcombe meteoroid.

	Initial	**Terminal**
Time (UTC)	21:54:15.88	21:54:24.12
Velocity (km/s)	13.54	~3
Latitude (°)	51.87106 ± 29 m	51.94011 ± 33 m
Longitude (°)	-3.10932 ± 17 m	-2.09634 ± 11 m
Height (km)	90.623 ± 38 m	27.554 ± 28 m
Mass (kg)	12.5 ± 3	~0.6
Observed length (km)	96.60	
Observed duration (s)	8.24	
Peak magnitude	-10.5^{M} at 53-55 km	
Peak dyn. pressure	0.6 MPa at 33.7 km	
Radiated energy	2.2×10^{7} J (0.005 T TNT)	

Table S4. Summary of recorded Winchcombe meteorite samples.

	Mass (g)	**Largest Fragment (g) / No. Fragments >1 g**	**Location**	**Finder**
Site 1: Winchcombe				
(M1) 01/03/21	206.5	8.8 / 44	Driveway / Lawn	Wilcock
(M2) 02/03/21	49.7	5.2 / 13	Driveway / Lawn	Wilcock
(M3) 04/03/21	39.5	7.3 / 1	Driveway / Lawn	Wilcock, King, Russell, Ensor
(M4) 05/03/21	23.0	6.2 / 2	Driveway / Lawn	Wilcock, Daly, Joy
(M5) 07/03/21	0.8	-	Driveway / Lawn	Wilcock, Suttle
Total Mass	*319.5*			
Site 2: Winchcombe				
(M6) 01/03/21	20.6	17.2 / 2	Driveway	Godfrey
Site 3: Woodmancote				
(M7) 02/03/21	11.2	11.2 / 1	Lawn	Carrick
Site 4: Woodmancote				
(M8) 05/03/21	20.1	13.7 / 2	Driveway	Mounsey
Site 5: Rushbury House				Ihasz, Daly, O'Brien, Hallis,
(M9) 06/03/21	160.1	152.0 / 1	Field	Bond
Site 6: Home Farm				Farrelly, Spencer, Naqvi,
(M10) 16/03/21	16.5	7.5 / 4	Field	Mayne, Skilton, Kirk
Total	**548.0**	152.0 / 70		

Table S5. Summary of fragments and powders of the Winchcombe meteorite analyzed in this study. Descriptions of the analytical techniques are given in the text.

Analysis	Sample ID	Parent Mass (g)	Institution
Fragments			
Major, minor & trace elements;	BM.2022,M1-91	0.3	NHM; Oxford
PSD-XRD; IR	BM.2022,M2-41	0.3	
Albedo	BM.2022,M1-22	2.0	Oxford
C, N & O isotopes	BM.2022,M1-85	8.8	OU
	BM.2022,M1-86	6.9	
Ti isotopes	BM.2022,M3-16	0.1	Bristol
Cr isotopes	BM.2022,M3-33	<0.1	St. Andrews
Ne isotopes; PSD-XRD	BM.2022,M2-36	0.3	SUERC; NHM
	BM.2022,M4-7	0.3	
Cosmogenic nuclides	BM.2022,M2-6	2.1	Gran Sasso
	OE-2021-23 (1)	3.2	Bratislava
	OE-2021-23 (7)	7.5	
	BM.2022,M2-40	0.1	Arizona
Magnetic properties	BM.2022,M1-95	0.1	Oxford/Cambridge
	BM.2022,M3-32		
H pyrolysis	BM.2022,M2-39	0.1	Glasgow/SUERC
GC-MS	BM.2022,M2-14	1.1	Imperial
LC-MS	BM.2022,M2-23	0.4	Glasgow
	BM.2022,M9-4	0.8	
Powders			
XRD; TGA	BM.2022,M1-88	0.2	NHM

5

Table S6. Neon isotope composition in Winchcombe meteorite samples BM.2022,M2-36 and BM.2022,M4-7.

Sample	**$^{21}Ne/^{22}Ne$**	**$^{20}Ne/^{22}Ne$**	**$^{21}Ne_{cos}$ (cc/g)**	**CRE age**	
1b-36				Ma	Ma
Step 1	0.0363 ± 0.0001	11.88 ± 0.02	1.76×10^{-10}		
			($\pm 2.22 \times 10^{-12}$)		
Step 2	0.0351 ± 0.0001	11.06 ± 0.02	6.17×10^{-11}		
			($\pm 1.17 \times 10^{-12}$)		
Step 3	0.0391 ± 0.0005	10.45 ± 0.02	1.95×10^{-11}		
			($\pm 1.04 \times 10^{-12}$)		
Step 4	0.0335 ± 0.0004	9.17 ± 0.01	5.90×10^{-12}		
			($\pm 9.04 \times 10^{-13}$)		
Total	0.0359 ± 0.0001	11.46 ± 0.02	2.63×10^{-10}	**0.212**	**0.085**
			($\pm 3.61 \times 10^{-12}$)	(± 0.0029)	(± 0.0012)
1d-8.2-6					
Step 1	0.1285 ± 0.0008	11.12 ± 0.02	1.60×10^{-10}		
			($\pm 1.19 \times 10^{-12}$)		
Step 2	0.0714 ± 0.0018	10.10 ± 0.04	4.04×10^{-11}		
			($\pm 1.77 \times 10^{-12}$)		
Step 3	0.0319 ± 0.0002	8.89 ± 0.01			
Step 4	0.0278 ± 0.0007	8.08 ± 0.02			
Total	0.0516 ± 0.0003	9.28 ± 0.01	1.89×10^{-10}	0.153	0.061
			($\pm 2.68 \times 10^{-12}$)	(± 0.0022)	(± 0.0009)

Table S7. Results of analysis of cosmogenic radionuclides in the Winchcombe meteorite.

Nuclide	Half-life	Activity (dpm kg^{-1})*			
		BM.2022,M2-6 INFN-LNGS Asergi	-23 (1) CU Bratislava	-23 (7) CU Bratislava	BM.2022,M2-40 AMS Tucson
^{7}Be	53.22 d	60 ± 20	< 190	110 ± 50	
^{58}Co	70.83 d	< 3	<14	< 6	
^{56}Co	77.236 d	5 ± 2	<9	8 ± 4	
^{46}Sc	83.788 d	8 ± 3	< 12	10 ± 5	
^{57}Co	271.8 d	< 11	<25	<17	
^{54}Mn	312.13 d	35 ± 4	39 ± 12	44 ± 6	
^{22}Na	2.6029 a	44 ± 5	36 ± 11	38 ± 7	
^{60}Co	5.2711 a	< 8	< 18	< 12	
^{44}Ti	60 y	< 13	<32	<19	
^{14}C	5730 a	-	-	-	13.3 ± 0.4
^{26}Al	7.17×10^{5} a	8 ± 2	14 ± 8	12 ± 5	

*) ^{14}C was analyzed by AMS, all other radionuclides by non-destructive gamma-ray spectrometry. Activities are corrected back to the date of the meteorite fall (28/2/2021). Uncertainties are given at 1σ. LNSG Asergi - Laboratori Nazionali del Gran Sasso; CU Bratislava - Department of Nuclear Physics and Biophysics of the Faculty of Mathematics, Physics and Informatics of the Comenius University; Tucson – National Science Foundation AMS Facility of the University of Arizona.

Table S8. Bulk major element composition (wt.%) of the Winchcombe meteorite measured by ICP-OES. Errors are the standard deviation of three replicate measurements.

	Winchcombe (BM.2022,M1-91)	**Winchcombe (BM.2022,M2-41)**
SiO_2	29.1 ± 0.4280	30.0 ± 0.1170
TiO_2	0.0972 ± 0.0004	0.0955 ± 0.0002
Al_2O_3	2.25 ± 0.0194	2.29 ± 0.0039
Fe_2O_3	31.7 ± 0.3700	32.1 ± 0.0529
MgO	18.1 ± 0.1470	17.8 ± 0.0372
CaO	1.79 ± 0.0067	1.57 ± 0.0072
Na_2O	0.565 ± 0.0035	0.616 ± 0.0015
P_2O_5	0.228 ± 0.0001	0.248 ± 0.0011
K_2O	0.0485 ± 0.0020	0.0604 ± 0.0004
MnO	0.21 ± 0.0009	0.207 ± 0.0005
NiO	1.55 ± 0.0085	1.56 ± 0.0036
Total	85.6	86.6

Table S9. Trace element abundances (ug g^{-1}) in the Winchcombe meteorite measured by ICP-MS. Errors are the standard deviation of three replicate measurements. < indicates that the abundance was below the limit of quantification.

	Winchcombe (BM.2022,M1-91)	**Winchcombe (BM.2022,M2-41)**
As	1.62 ± 0.0245	1.66 ± 0.0411
Ba	3.26 ± 0.0951	10.4 ± 0.2740
Be	<	<
Bi	<	<
Cd	0.396 ± 0.0078	0.39 ± 0.0089
Co	526 ± 4.28	521 ± 7.04
Cr	2572 ± 20.5	2561 ± 23.5
Cs	0.126 ± 0.0014	0.172 ± 0.0004
Cu	127 ± 0.5530	121 ± 1.6600
Ga	8.11 ± 0.0056	7.89 ± 0.0343
Ge	23.2 ± 0.0758	22.9 ± 0.2040
Hf	0.153 ± 0.0009	0.168 ± 0.0109
Li	1.39 ± 0.0200	1.65 ± 0.1080
Mo	1.16 ± 0.0048	1.04 ± 0.0061
Nb	0.345 ± 0.0005	0.343 ± 0.0038
Pb	1.46 ± 0.0215	1.44 ± 0.0346
Rb	1.68 ± 0.0469	2.0 ± 0.1020
Sb	0.106 ± 0.0009	0.106 ± 0.0030
Sc	7.65 ± 0.0271	9.7 ± 0.0377
Sn	<	<
Sr	10.2 ± 0.0543	9.97 ± 0.0320
Ta	<	<
Th	<	<
Tl	0.0883 ± 0.0025	0.0882 ± 0.0007
U	0.0108 ± 0.0002	0.0109 ± 0.0002
V	50.6 ± 1.2100	52.5 ± 0.4140
W	<	<
Y	1.85 ± 0.0081	2.05 ± 0.0111
Zn	168 ± 0.2410	173 ± 0.6480
Zr	4.7 ± 0.0328	5.27 ± 0.2680
La	0.398 ± 0.0326	0.37 ± 0.0076
Ce	0.996 ± 0.0175	1.51 ± 0.0106

Pr	0.13 ± 0.0008	0.132 ± 0.0015
Nd	0.66 ± 0.0038	0.662 ± 0.0141
Sm	0.209 ± 0.0082	0.201 ± 0.0071
Eu	0.0835 ± 0.0009	0.0821 ± 0.0008
Gd	0.276 ± 0.0015	0.283 ± 0.0040
Tb	0.0528 ± 0.0005	0.0577 ± 0.0004
Dy	0.358 ± 0.0058	0.419 ± 0.0133
Ho	0.078 ± 0.0008	0.0941 ± 0.0015
Er	0.235 ± 0.0064	0.258 ± 0.0008
Tm	0.0369 ± 0.0009	0.0364 ± 0.0011
Yb	0.237 ± 0.0028	0.23 ± 0.0037
Lu	0.00347 ± 0.0001	0.0354 ± 0.0002

Table S10. Oxygen isotopic composition of the Winchcombe meteorite samples BM.2022,M1-85 and BM.2022,M1-86.

	Weight (mg)	**$\delta^{17}O$(‰)**	1 σ	**$\delta^{18}O$ (‰)**	1 σ	**$\Delta^{17}O$ (‰)**	1 σ
M1-85-1	2.643	2.894	0.018	9.657	0.007	−2.128	0.020
M1-85-2	2.407	2.610	0.025	9.305	0.011	−2.229	0.027
average		*2.752*		*9.481*		*−2.178*	
M1-86-1	2.407	0.832	0.017	7.074	0.013	−2.846	0.020
M1-86-2	2.638	1.054	0.028	7.514	0.011	−2.853	0.034
average		*0.943*		*7.294*		*−2.850*	

Table S11. Titanium isotopic composition of the Winchcombe meteorite sample BM.2022,M3-16. Errors are 2σ.

Sample	n	$\Delta'^{46/47}Ti_{49/47}$ (ppm)	$\Delta'^{48/47}Ti_{49/47}$ (ppm)	$\Delta'^{50/47}Ti_{49/47}$ (ppm)
M3-16	10	46 ± 8	−4 ± 4	321 ± 9

Table S12. Chromium isotopic composition of the Winchcombe meteorite sample BM.2022,M3-33.

Sample	n	$\varepsilon^{53}Cr_{50/52}$	2se	$\varepsilon^{54}Cr_{50/52}$	2se
M3-33	4	0.319	0.029	0.775	0.067
DTS2	16	0.037	0.021	0.002	0.041

5

Table S13. Bulk modal mineralogy of the Winchcombe meteorite determined using PSD-XRD. PSF = total phyllosilicate abundance / [total anhydrous silicate + total phyllosilicate abundance].

	Winchcombe (M1-91)	**Winchcombe (M2-41)**	**Winchcombe (M2-36)**	**Average (1σ)**
Mg-serpentine	53.8	72.0	57.4	61.1 (9.6)
Fe-serpentine	33.7	21.1	30.0	28.3 (6.5)
Olivine	6.5	3.1	4.0	4.5 (1.8)
Pyroxene	1.6	-	2.6	2.1 (0.7)
Calcite	1.9	1.6	1.0	1.5 (0.5)
Magnetite	2.2	1.9	4.1	2.7 (1.2)
Sulphides	0.4	0.3	1.0	0.6 (0.4)
PSF	0.92	0.97	0.93	
Petrologic Type	1.2	1.1	1.2	

Table S14. Summary of polished sections of the Winchcombe meteorite characterized by SEM in this study. *Section P30554 mainly consisted of fusion crust.

Polished Section	Sample ID	Parent Mass (g)	Institution
P30423 (40.2 mm^2)	BM.2022,M1-87	0.3	
P30424 (7.5 mm^2)	BM.2022,M3-29	<0.1	
P30544 (2.5 mm^2)	BM.2022,M2-46	<0.1	NHM
P30548 (8.2 mm^2)	BM.2022,M1-105	<0.1	
P30553 (9.1 mm^2)	BM.2022,M9-15	<0.1	
P30540 (5.6 mm^2)	BM.2022,M2-42	<0.1	Glasgow
P30552 (9.8 mm^2)	BM.2022,M9-14	<0.1	
P30541 (12.2 mm^2)	BM.2022,M2-43	<0.1	Manchester
P30542 (7.8 mm^2)	BM.2022,M2-44	<0.1	Kent
P30543 (10.8 mm^2)	BM.2022,M2-45	<0.1	Leicester
P30545 (18.9 mm^2)	BM.2022,M2-47	<0.1	Plymouth
P30551 (7.4 mm^2)	BM.2022,M9-13	<0.1	Imperial
P30554 (5.1 mm^2)*	BM.2022,M9-16	<0.1	
P30555 (9.1 mm^2)	BM.2022,M9-17	<0.1	

Table S15. Representative composition (wt.%) of chondrule silicates, matrix and phyllosilicate clumps, pentlandite, tochilinite, and calcite measured by SEM-EDS in the main lithology of the Winchcombe meteorite. *n* is the number of analyses and values in parentheses are 1 standard deviation.

5

	Type I chondrule silicates	**Type II chondrule silicates**	**Matrix**	**Phyllosilicate clump (Fe-rich rim)**	**Phyllosilicate clump (Mg-rich core)**	**Pentlandite**	**Tochilinite**	**Calcite**
n	*42*	*8*	*61*	*106*	*78*	*46*	*3*	*49*
C								15.4 (3.1)
O	45.6 (1.7)	41.8 (1.8)	32.0 (2.2)	38.4 (4.4)	45.2 (7.0)	3.6 (3.4)	22.2 (0.7)	44.3 (2.5)
Na			0.8 (0.2)	0.5 (0.2)	0.5 (0.1)		0.1 (0.1)	
Mg	34.1 (1.8)	24.4 (3.7)	11.4 (1.8)	10.2 (1.5)	17.2 (0.7)	0.5 (1.0)	4.8 (2.6)	0.7 (0.9)
Al			0.9 (0.3)	1.3 (0.2)	1.0 (0.1)		0.4 (0.1)	0.1 (0.1)
Si	19.8 (0.8)	18.2 (0.8)	13.1 (1.4)	11.3 (1.1)	16.9 (0.8)	0.5 (0.9)	3.0 (3.4)	0.7 (0.9)
P			0.1 (0.1)				0.7 (0.6)	
S			2.6 (0.6)	5.3 (1.8)	1.5 (0.6)	30.7 (2.7)	19.1 (3.2)	0.2 (0.2)
Cl			0.2 (0.2)					
K							0.2 (0.1)	
Ca	0.3 (0.1)	0.1 (0.1)	0.2 (0.3)			0.1 (0.3)	0.1 (0.1)	37.6 (2.0)
Cr	0.3 (0.1)	0.3 (0.1)	0.3 (0.1)	0.2 (0.1)	0.1 (0.1)	0.3 (1.2)	0.9 (0.6)	
Mn	0.1 (0.1)	0.1 (0.1)	0.1 (0.1)	0.1 (0.1)	0.1 (0.1)		0.1 (0.1)	
Fe	1.4 (1.5)	16.5 (5.3)	13.5 (2.8)	26.0 (2.9)	10.9 (1.4)	32.8 (5.2)	35.7 (3.0)	1.0 (0.8)
Co						1.4 (1.0)	0.5 (0.3)	
Ni		0.1 (0.1)	1.6 (0.6)	0.9 (0.3)	0.5 (0.2)	29.0 (7.8)	9.1 (4.9)	
Total	101.5 (3.6)	101.6 (2.0)	76.7 (5.2)	94.3 (6.5)	94.0 (6.0)	99.1 (3.8)	96.7 (5.8)	100.0 (0.01)
Mg#	98.2 (2.0)	77.0 (8.1)	65.8 (7.3)	47.3 (6.0)	78.3 (2.5)		23.1 (10.5)	

Table S16. Summary of the bulk magnetic properties of the Winchcombe meteorite samples BM.2022,M1-95 and BM.2022,M3-32.

Sample	**M_S** ($Am^{-2}kg^{-1}$)	**M_{RS}** ($\times 10^{-3}$ $Am^{-2}kg^{-1}$)	**H_C** ($\times 10^{-3}$ T)	**H_{CR}** ($\times 10^{-3}$ T)	**log(χ)** ($\times 10^{-9}$ m^3 kg^{-1})	**S300 ratio**
M1-95	1.02	60.8	8.67	36.5	3.52	0.96
M3-32	0.10	6.98	9.74	38.3	3.03	0.95

Table S17. Mass loss (wt.%) as a function of temperature during TGA of the Winchcombe meteorite sample BM.2022,M1-88. The DTG curve is divided into temperature regions related to the dehydration of terrestrial adsorbed H_2O (15 - 200°C), the dehydration and dehydroxylation of Fe-(oxy)hydroxides (200 – 400°C) and phyllosilicates (400 – 770°C), and the breakdown of carbonates (770 – 900°C).

	15 - 200°C	**200 - 400°C**	**400 - 770°C**	**770 - 900°C**	**H_2O** (200 - 770°C)	**Fe-serpentine** (300 - 450°C)	**Mg-serpentine** (450 - 800°C)
Winchcombe (M1-88)	3.0	2.2	9.0	0.8	11.2	3.1	7.9

Table S18. Summary of the abundance and isotopic composition of hydrogen released during stepped pyrolysis of the Winchcombe meteorite samples BM.2022,M2-39-a, BM.2022,M2-39-b, and BM.2022,M2-39-c.

Winchcombe Sample No.	**Step (°C)**	**H_2O (wt. %)**	**Fraction Released**	**H (wt. %)**	**δD (‰ vSMOW)**
M2-39-a	100	0.29	0.03	0.03	−23
(45.1 mg)	200	1.20	0.11	0.13	−70
	300	1.32	0.12	0.15	−143
	400	2.79	0.26	0.31	−158
	500	2.91	0.27	0.33	−148
	700	1.91	0.18	0.21	−146
	1100	0.36	0.03	0.04	−43
	Total	**10.78**	**1.00**	**1.21**	
M2-39-b	100				
(32.7 mg)	200	0.92	0.08	0.10	−58
	300	1.17	0.10	0.13	−122
	400	3.11	0.27	0.35	−167
	500	2.74	0.23	0.31	−151
	700	2.95	0.25	0.33	−127
	1100	0.77	0.07	0.09	−55
	Total	**11.66**	**1.00**	**1.31**	
M2-39-c	100				
(30.9 mg)	200	0.86	0.07	0.10	−74
	300	1.13	0.09	0.13	−100
	400	2.97	0.24	0.33	−167
	500	3.17	0.26	0.36	−147
	700	3.14	0.26	0.35	−144
	1100	1.03	0.08	0.12	−74
	Total	**12.30**	**1.00**	**1.38**	

Table S19. Carbon data from stepped combustion of Winchcombe chips BM.2022,M1-85 and BM.2022,M1-86.

Temp (˚C)	[C] (ppm)	$\delta^{13}C$ (‰)	± σ (‰)	[C] (ppm)	$\delta^{13}C$ (‰)	±σ (‰)
	M1-85 (W1) 5.0502 mg			M1-86 (W2) 5.0981 mg		
100	56.6	3.1	0.2	19.7	-0.2	0.3
125	57.7	2.6	0.2			
150	60.8	0.5	0.1	135.1	2.0	0.2
175	100.2	5.6	0.4			
200	249.1	-8.0	0.3	288.1	-4.9	0.2
225	419.5	-6.0	0.7			
250	681.5	-2.7	0.1	891.8	13.1	5.0
275	963.0	2.4	0.7	670.4	8.7	0.9
300	1150.2	-3.6	0.3	825.0	-17.2	0.7
325	1324.3	-6.4	0.1	1505.8	-7.5	0.6
350	1456.4	-16.6	0.7	1543.2	-7.0	0.7
375	1593.3	-10.6	0.6	1658.1	-10.9	0.2
400	1874.9	-19.0	0.5	1728.8	-5.8	0.2
425	2043.1	-21.1	0.5	1836.1	-14.3	0.1
450	1862.3	-12.2	0.2	2123.1	-15.4	0.4
475	1268.3	-12.8	0.7	1670.8	-11.6	0.7
500	637.0	-9.6	0.7	1050.7	-9.0	0.3
525	260.6	-0.1	1.0	498.8	27.4	0.2
550	414.4	37.9	0.6	459.9	23.8	0.5
575	533.0	57.2	0.2	556.7	40.0	0.9
600	1099.4	61.5	0.2	1056.1	nm	
625				668.1	42.8	0.9
650	206.1	43.9	0.8	109.8	37.2	0.1
700	47.8	14.5	3.3	414.8	17.5	1.2
750	167.9	9.6	0.4	350.6	17.3	0.2
800	49.7	-8.9	1.1	122.7	nm	
850	42.3	17.4	0.1	60.8	nm	
900	21.5	5.7	1.8	54.7	48.9	5.0
950	19.0	26.5	1.5	64.2	55.8	0.9
1000	21.2	32.8	2.1	116.1	87.5	1.6
1050	31.4	65.0	2.5			
1100	18.7	60.4	0.4	98.6	142.5	1.2
1200	43.2	-19.9	0.1	54.2	12.6	0.2
1300	28.8	-16.3	0.2	34.7	-28.1	0.2
1400	20.4	-11.7	0.2	24.5	-19.3	0.2
Total:	18823.8	-2.8	0.1	20692.0	-0.6	0.1

Table S20. Nitrogen data from stepped combustion of Winchcombe chips BM.2022,M1-85 and BM.2022,M1-86.

Temp. (˚C)	[N] (ppm)	$\delta^{15}N$ (‰)	± σ (‰)	[N] (ppm)	$\delta^{15}N$ (‰)	± σ (‰)
	M1-85 (W1) 5.0502 mg			M1-86 (W2) 5.0981 mg		
100	0.9	25.9	0.2	0.5	29.3	0.4
125	1.0	22.3	0.2			
150	0.8	21.7	0.2	0.9	23.4	0.2
175	1.0	12.4	0.2			
200	5.5	30.1	0.2	7.8	41.4	0.2
225	10.2	36.3	0.2	7.7	56.0	0.2
250	15.8	38.4	0.2	9.7	56.1	0.2
275	19.4	40.1	0.2	6.7	51.9	0.2
300	20.1	35.3	0.2	10.6	45.5	0.2
325	18.6	27.1	0.2	19.3	32.9	0.2
350	20.7	16.2	0.2	21.8	16.2	0.2
375	29.0	-2.6	0.2	32.6	0.2	0.2
400	43.0	-14.1	0.2	54.4	-8.8	0.2
425	54.6	-8.8	0.2	71.5	-5.9	0.2
450	50.8	20.3	0.2	63.9	16.2	0.2
475	33.6	31.1	0.2	47.1	31.9	0.2
500	23.5	27.4	0.2	27.1	29.9	0.2
525	17.2	30.5	0.3	18.3	31.4	0.2
550	10.3	36.8	0.3	11.9	41.4	0.2
575	5.7	35.7	0.3	7.2	45.4	0.2
600	3.5	26.5	0.3	4.4	41.8	0.3
625				3.0	41.9	0.3
650	4.2	21.4	0.2	2.0	31.7	0.2
700	5.0	16.6	0.2	5.8	35.8	0.2
750	6.3	37.1	0.2	7.3	47.3	0.2
800	2.7	4.2	0.2	2.8	28.0	0.2
850	3.4	-18.4	0.2	1.9	-5.4	0.2
900	3.5	-19.9	0.2	2.3	-2.8	0.2
950	1.6	-1.0	0.2	1.7	15.4	0.3
1000	0.9	-25.3	0.2	0.9	-7.3	0.3
1050	0.5	-46.9	0.3			
1100	0.3	-40.4	0.3	0.9	-31.0	0.3
1200	0.2	-21.8	0.3	0.8	0.9	0.4
1300	0.0	36.7	0.4	0.7	-2.9	0.3
1400		nd		0.8	2.3	0.3
Total:	413.5	15.8	0.3	454.1	17.6	0.3

Table 21. He, Ne, Ar and Xe concentrations in the Winchcombe meteorite samples BM.2022,M1-85 and BM.2022,M1-86.. nd – not determined.

Sample	^{4}He	^{20}Ne	^{36}Ar	^{132}Xe
		$\times 10^{-6}$ cm^3 STP g^{-1}		
M1-85 (W1)	145	3	2.87	nd
M1-86 (W2)	790	15	1.96	0.672

Table S22. The percentage of ammonium carbonate (A) and acetonitrile (B) flowing through the LC-MS column over time.

Time (mins)	% A	% B
0	20	80
15	80	20
15	95	5
17	95	5
17	20	80
26	20	80

Table S23. Summary of the amino acid content of the Winchcombe meteorite sample BM.2022,M2-14 and a soil sample collected near the fall site. n. f. indicates that the compound was not found in the sample above the detection limits.

	Winchcombe		**Fall Site Soil**	
	Free	Total	Free	Total
Glycine	131.7 ± 17.8	163.0 ± 17.2	13875 ± 181	54677 ± 402
D-Alanine	47.2 ± 2.2	57.0 ± 6.9	1595 ± 37	4957 ± 31
L-Alanine	46.4 ± 2.2	50.2 ± 5.1	34906 ± 607	54872 ± 458
β-Alanine	n. f.	28.3 ± 3.4	1389 ± 12	2869 ± 12
D-Serine	n. f.	n. f.	1695 ± 67	20629 ± 655
L-Serine	n. f.	n. f.	19627 ± 1266	68247 ± 5404
D-α-aminobutyric acid (ABA)	11.6 ± 1.4	12.6 ± 1.8	n. f.	n. f.
L-α-ABA	14.3 ± 1.2	16.7 ± 2.5	n. f.	n. f.
D-β-ABA	5.3 ± 3.4	8.0 ± 2.2	n. f.	n. f.
L-β-ABA	6.8 ± 3.2	12.8 ± 1.4	n. f.	n. f.
γ-ABA	n. f.	14.0 ± 2.3	1603 ± 25	2139 ± 21
α-aminoisobutyric acid (AIB)	467.1 ± 16.7	331.1 ± 33.6	n. f.	n. f.
D-β-AIB	n. f.	n. f.	n. f.	n. f.
L-β-AIB	n. f.	n. f.	n. f.	n. f.
D-Aspartic acid	6.7 ± 1.7	6.8 ± 0.7	1252 ± 15	10238 ± 33
L-Aspartic acid	12.7 ± 4.2	13.2 ± 1.6	18742 ± 206	82678 ± 472
D-Threonine	n. f.	n. f.	n. f.	n. f.
L-Threonine	n. f.	n. f.	20293 ± 273	40837 ± 284
D-Glutamic acid	<18.5	17.8 ± 3.0	1121 ± 21	5731 ± 34
L-Glutamic acid	<42.4	38.9 ± 4.1	26336 ± 229	84812 ± 705
D-Norvaline (2-apa)	3.0 ± 0.3	3.4 ± 0.6	n. f.	n. f.
L-Norvaline (2-apa)	2.7 ± 0.2	3.8 ± 0.8	n. f.	n. f.
D-Isovaline	196.7 ± 8.6	138.3 ± 14.7	n. f.	n. f.
L-Isovaline	194.4 ± 8.5	130.7 ± 13.9	n. f.	n. f.
D-Valine (2-a-3-mba)	9.2 ± 1.5	11.1 ± 1.5	n. f.	370 ± 0.2
L-Valine (2-a-3-mba)	16.6 ± 2.6	14.9 ± 1.5	28575 ± 477	30955 ± 153
R-3-Aminopentanoic acid (3-apa)	n. f.	n. f.	n. f.	n. f.
S-3-Aminopentanoic acid (3-apa)	n. f.	n. f.	n. f.	n. f.
D-4-amino-pentanoic acid (4-apa)	n. f.	n. f.	n. f.	n. f.
L-4-amino-pentanoic acid (4-apa)	n. f.	n. f.	n. f.	n. f.
5-Aminopentanoic acid (5-apa)	n. f.	20.3 ± 1.7	413 ± 11	847 ± 15
3-Amino-3-methyl butanoic acid	n. f.	n. f.	n. f.	n. f.

(3-a-3-mba)				
3-Amino-2,2-dimethylpropanoic acid (3-a-2,2-dmpa)	n. f.	n. f.	n. f.	n. f.
6-Amino-Hexanoic acid (eaca)	n. f.	28.6 ± 6.6	n. f.	n. f.
D-Norleucine	n. f.	n. f.	n. f.	n. f.
L-Norleucine	n. f.	n. f.	n. f.	n. f.
D-isoleucine	n. f.	n. f.	n. f.	n. f.
L-isoleucine	n. f.	n. f.	16639 ± 256	15752 ± 43
D-Leucine	5.0 ± 0.8	4.1 ± 0.1	n. f.	n. f.
L-Leucine	9.7 ± 1.5	6.5 ± 1.0	38345 ± 537	26979 ± 71
L-Alloisoleucine	n. f.	n. f.	n. f.	n. f.
D-2-Methylleucine	n. f.	n. f.	n. f.	n. f.
D-2-Aminoheptanoic acid (2-aha)	n. f.	n. f.	n. f.	n. f.
L-2-Aminoheptanoic acid (2-aha)	n. f.	n. f.	n. f.	n. f.
Total	**1247.9 ± 30.9**	**1132.3 ± 49.3**	**226406 ± 1662**	**507587 ± 5553**